

MAGNETIC DOMAINS IN HEMATITE

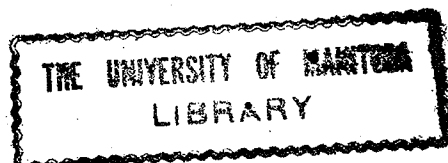
A thesis

Submitted to

The Faculty of Graduate Studies, University of
Manitoba, in partial fulfillment of the
requirements of the degree of Doctor of Philosophy.

By

John A. Eaton,
Winnipeg, Manitoba,
May, 1970.



Abstract

The aim of the research in this thesis was to determine by all means available the magnetic domain structure of synthetic single crystal hematite and any other related properties. The magnetic domain structure was determined by the magnetite colloid technique. Ideally, it was 180° slab-type structure with the walls parallel to the basal plane. Magnetoelastic interactions with strain causing crystal defects produced distortions from this in the bulk crystal structure to maze-like or cylindrical 180° domains with parallel axes in the basal plane which changed direction if magnetoelastic interactions demanded it. In thin sections, the magnetoelastic effect caused the appearance of a two phase domain structure of $2\phi < 180^\circ$ walls where ϕ varied. The plane of these walls was parallel to basal plane easy direction and at $\sim 26^\circ$ to the basal plane. A 180° structure could disappear abruptly or more generally by these 2ϕ walls. Magnetoelastic interactions with regular lattice distortions caused by the growth structure appeared to stabilize a narrow strip domain pattern of 2ϕ walls in bulk (110) surfaces.

The magnetic domain observations also allowed the

Morin transition process to be observed. A colloid wall formed at the boundary between the antiferromagnetic-weakly ferromagnetic phases. The transition always occurred by a process of adjacent (110) growth layers going through the transition in succession as temperature varied. The transition temperature range was consistent with bulk measurements and was found to be caused by a non-uniform doping which also followed the growth structure. The shift was also related to difference of dopant ionic size from the Fe ionic size. Domain behaviour in this process appeared to be nothing more than a response to a changing boundary of the ferromagnetic phase. The domain structure generally showed a little or no changes in the process.

Mössbauer, magnetometer and crystal physical property measurements gave further support to the models proposed for the domain and transition behaviour.

Wall models consistent with magnetoelastic anisotropy were developed which explained the domain walls. Domain wall energies were calculated to be $\sim 4-13 \times 10^{-2}$ ergs/cm² which agreed with domain observations.

Acknowledgements

The author wishes to thank Professor A. H. Morrish for his support and encouragement that made this research possible. Also, the invaluable discussions with Professor C. W. Searle and his advice are very much appreciated. He would also like to thank many of his fellow graduate students for their cooperation and help. Finally, he would like to thank his family especially his wife, Phyllis, without whom this thesis would not have been possible.

Table of Contents

Abstract	
Acknowledgements	
I. Introduction	1
II. Preliminary Considerations	3
A. The Magnetic Free Energy	3
B. Principles of Domain Formation	14
C. Principles of the Bitter Figure Technique	24
III. Experimental Technique	28
A. Crystals and Their Preparation	28
B. Preparation of the Magnetite Colloid	33
C. Magnetite Colloid Domain Observations	34
1. At Room Temperature	34
2. Between -40°C and 50°C	36
D. Crystal Physical Properties	39
1. X-ray Diffraction	39
2. X-ray Fluorescence	40
3. Electron Microprobe Analysis	40
4. X-ray Topographic and Optical Studies	41

E.	Bulk Magnetization Properties	44
1.	Magnetometer Measurements	44
2.	Mössbauer Spectrometer Measurements	46
IV.	Experimental Results	49
A.	Magnetite Colloid Domain Patterns	49
1.	At Room Temperature	49
a)	No Magnetic Field or Stress	49
b)	With Applied Magnetic Field	55
c)	With Applied Stress and Magnetic Fields	65
2.	Colloidal Structures at the Morin Transition	68
B.	Crystal Physical Properties	80
1.	X-ray Diffraction and X-ray Fluorescence	80
2.	Electron Microprobe Analysis	83
3.	X-ray Topographic and Optical Observations	88
C.	Bulk Magnetization Measurements	91
1.	Magnetometer Measurements	91
2.	Mössbauer Spectra Observations	96

V. Discussion of Results	103
A. The Domain Structure of Hematite	103
1. The Orientation of the Domains'	
Magnetizations	103
2. The Structure of the Domain Walls	112
a) The N-Domain Wall	112
b) The C- and CN-Domain Walls	117
B. The Morin Transition	120
C. Bulk Magnetization Measurements	124
1. Magnetometer Measurements	124
2. Mössbauer Measurements	126
D. Crystal Physical Characteristics	127
VI. Conclusions	129
A. The Domain Structure	129
B. The Morin Transition	129
C. The Physical Characteristics of	
Hematite Crystals	130
D. Suggestions for Further Experiments	130

References

Tables

I. Domain magnetostatic and wall energies	23
II. Mechanical polishing procedure	29
III. Width of domains	56
IV. Average Distortion of Hematite Lattice from $F_e K\alpha_1$ (232) and (318) Reflections	81
V. Mössbauer Spectra Parameters for (1 $\bar{1}$ 0) Thin Section	99

Figures

1. Rhombohedral unit cell of hematite and coordinate system to which spins are referred	5
2. Domain configurations for energy formula of Table I	22
3. Fringing field models for domain walls at crystal surface	26
4. Laue photographs of $(1\bar{1}0)$ and $(11\bar{2})$ planes	30
5. Geometry of $(1\bar{1}0)$ and $(11\bar{2})$ planes relative (110) planes	31
6. Stress apparatus	37
7. Temperature control apparatus	38
8. X-ray topography camera	42
9. Mössbauer experiment geometry for spin axis direction determination	47
10. N-domain patterns	50
11. C- and CN-domain patterns	52
12. Effect of magnetic field, in basal plane, parallel and perpendicular to a $(11\bar{2})$ thin section having N-domains	57
13. Effects of defect on magnetic field behaviour in a $(11\bar{2})$ thin section	59

14.	Magnetic field behaviour of CN-domains and unusual effects related to CN-domains	62
15.	Graph of magnetization versus field according to domain widths in $(1\bar{1}0)$ and $(11\bar{2})$ thin sections	64
16.	Graph of N-domain width for a $(1\bar{1}0)$ thin section versus applied stress	66
17.	The Morin transition for (110) surface of pure bulk crystal	69
18.	The Morin transition in pure 2 mole % Ga doped thin section	70
19.	The Morin transition in Ti doped bulk and thin section (110) surfaces	71
20.	The WF-AF phase boundaries as a function of temperature on 0.5 mole % Rh doped bulk crystal surface	75
21.	The WF-AF phase boundaries on a 1.0 mole % Rh doped crystal	76
22.	The WF-AF phase boundaries on a 0.1 mole % Ti doped crystal	77
23.	Photographs of crystal surfaces showing scan paths for electron microprobe analysis	82
24.	Graph of T_M versus doping for 0.5 mole % Rh doped surface	84

25.	Graph of T_M versus doping for 1.0 mole % Rh doped crystal	85
26.	Graph of T_M versus doping for 0.1 mole % Ti doped crystal	86
27.	Graph of doping along scan paths for 0.5 mole % Ga and 1.0 mole % Al doped crystals	87
28.	Photographs of crystals and crystal surfaces	89
29.	Hysteresis loops of a poor quality large bulk crystal before and after a 1200°C anneal	92
30.	Hysteresis loops of a good quality bulk crystal before and after 1200°C anneal	93
31.	Hysteresis loop of small bulk crystal	94
32.	Magnetization versus field up to saturation for small bulk crystal	95
33.	Magnetization as versus temperature at 100 Oe and 15 kOe for 0.5 mole % Rh doped crystal	97
34.	Magnetization versus temperature at 100 Oe for 1.0 mole % Rh doped crystal	98
35.	Mössbauer spectra for $\pm 15^\circ$ and 0° orientations of a $(1\bar{1}0)$ thin section	102
36.	Model for an AF-F domain wall parallel to the basal plane	113
37.	Model for a F wall parallel to the basal plane	114

I. Introduction

Hematite, or $\alpha\text{-Fe}_2\text{O}_3$, which is readily obtainable in large single crystals from nature, has a very weak magnetization at room temperature. Thus, in the past considerable research, has been devoted to the magnetic properties of hematite. This was, no doubt, stimulated by the research of Morin¹ and of Shull et al². In 1950, Morin observed that hematite underwent a transition, now called the Morin transition, where the susceptibility rapidly increased with temperature. The Morin transition temperature T_M has now been measured to be $T_M \sim -10$ C for very pure synthetic single crystal hematite. Then in 1951, Shull et al determined that hematite existed in what appeared to be two different antiferromagnetic states above and below the transition. In the next few years various researchers attempted to explain the weak moment in terms of crystal defects, impurities and even a net moment generated in antiferromagnetic domain walls. Finally, Dzialoshinskii³ produced the now accepted thermodynamic argument which showed that in the one antiferromagnetic state it was possible for the sublattice spins to be slightly canted towards each other without lowering the magnetic symmetry. The quantum mechanical basis of this canting was subsequently given by Moriya⁴ as a spin-orbit effect in the super-exchange interaction. Continued interest in hematite up to the present time has mainly been concerned

with measurement and explanation of effects related to magnetocrystalline anisotropy and magnetostriction.

Since hematite has an ordered ferromagnetic component, although very weak, a domain structure could be expected to exist. This was indeed shown to be the case by Blackman et al⁵ and William et al⁶ and has now been well established by the continued work by various researchers⁷⁻¹¹ under M. Blackman. Also, it has been established that the domain structure disappears in a characteristic fashion at the Morin transition.

Since we have a supply of, and could grow, large highly perfect,¹² pure and doped, crystals of hematite by a method established by P.J. Besser¹³ it was felt that we might be able to contribute towards further explanation of the domain structure of hematite. Therefore, it is the purpose of this thesis, to put forward all the results of a research program into the domain structure in hematite.

II. Preliminary Considerations

A. The Magnetic Free Energy

Domain structures in ferromagnetic materials are a mechanism by which the magnetic free energy can be minimized. Therefore, to explain domain structures a knowledge of the mechanisms that can contribute to the magnetic free energy is necessary. The magnetic free energy can be expressed¹⁴

$$F_T = F_H + F_D + F_e + F_K + F_\sigma + F_o \quad (1)$$

where F_H is the free energy due to an applied magnetic field, F_D the self energy due to uncompensated poles, F_K the magnetocrystalline anisotropy energy, F_σ the magnetostrictive energy, F_e the exchange energy and F_o the energy due to any other magnetic interactions relevant to the material such as crystalline imperfections. Thus, this expression is completely general and can be applied to any magnetically ordered material if the form of all the magnetic interactions is known.

The energy due to an applied field \underline{H} is

$$F_H = - \int \underline{m} \cdot \underline{H} dv \quad (2)$$

and the self magnetostatic energy is

$$F_D = -\frac{1}{2} \int \underline{m} \cdot \underline{H}_D dv \quad (3)$$

where \underline{m} is the magnetization and \underline{H}_D is the self field due to uncompensated poles. For a uniformly magnetized ellipsoid

$$F_D = \frac{1}{2} D m^2 \quad (4)$$

where D is a geometrical factor depending on the shape of the ellipsoid relative to the direction of magnetization

and is relatively easy to calculate.¹⁴ However, calculation of demagnetization energies for other than ellipsoid shaped specimens becomes very complicated and laborious and usually involves approximations.

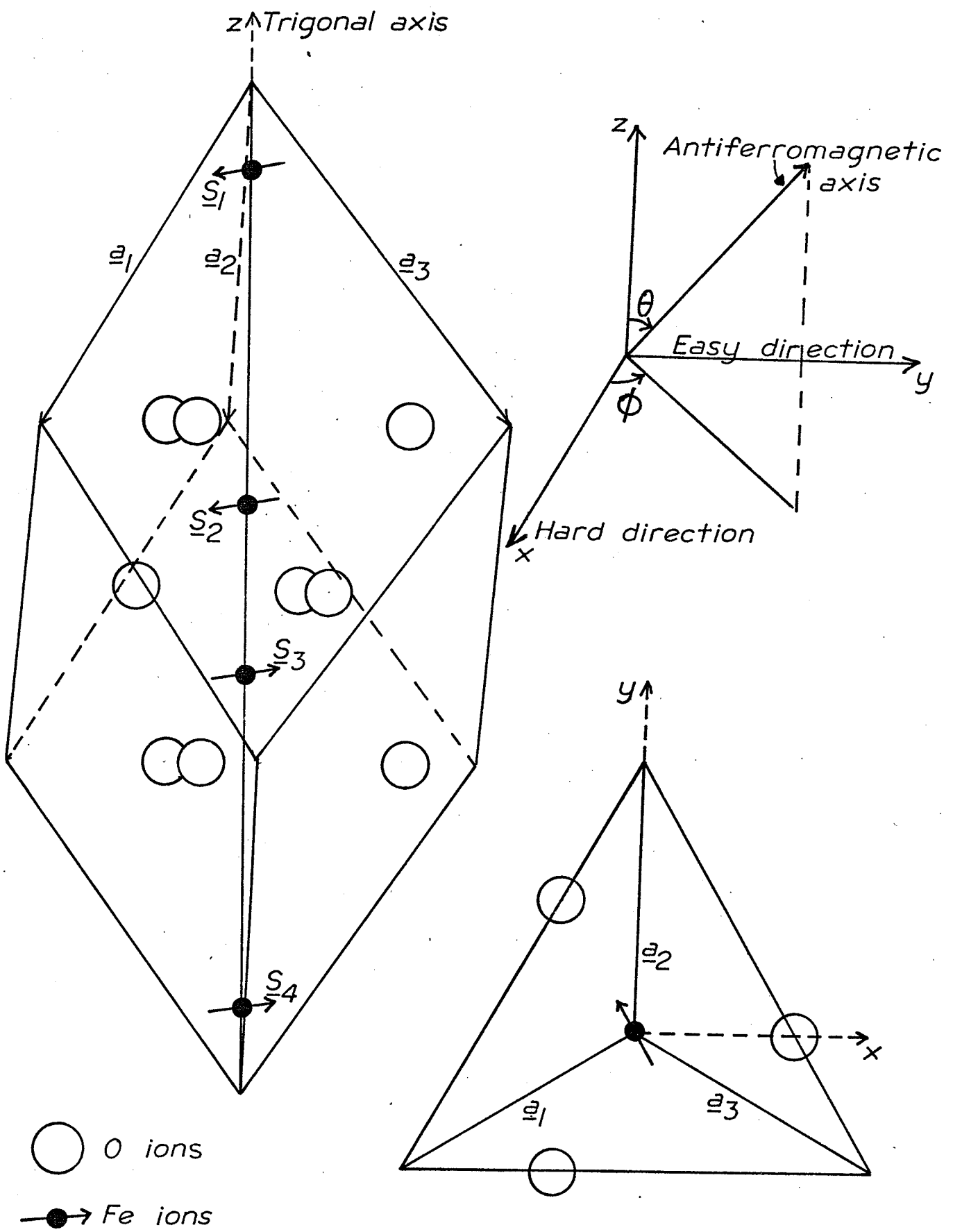
The remainder of the terms in equation (1), ignoring F_0 , generally depend on crystal and magnetic symmetry. Therefore, a discussion of the crystal structure of hematite is appropriate at this point.

Hematite has a trigonal structure with space group $R\bar{3}c$ as determined by Pauling et al.¹⁵ and later refined by Blake et al.¹⁶ The structure can be represented either by a rhombohedral or a hexagonal lattice. The rhombohedral cell is illustrated in Fig. 1. The structure may be described as a slightly distorted hexagonal close packed structure of oxygen atoms with $2/3$ of the octahedral interstices containing iron atoms. The iron atoms are so arranged such that, along any hexagonal axis, every third interstice is empty. Therefore, the lattice repeats itself after every six layers of oxygen atoms.

The microscopic origin of ordering in magnetic systems is the exchange interaction.¹⁷ This interaction arises between neighbouring magnetic ions because of the effect of the Pauli Exclusion Principle and the indistinguishability of electrons when the outermost electron orbitals of the two ions overlap. This generally results in the ions having

Figure 1.

Rhombohedral unit cell of hematite. The relative direction of the spins and the coordinate system to which they will always be referred are indicated on the unit cell.



parallel spin configurations as the lowest energy state. This interaction energy between the spins of the ions summed over the whole crystal can be represented, assuming only nearest neighbour interactions and isotropy of the exchange interaction as

$$F_e = -2J_e \sum \underline{S}_i \cdot \underline{S}_j \quad (5)$$

$J_e > 0$ is the exchange integral and \underline{S}_i the sum of the unpaired spins on the ion.

The exchange interaction may also occur via an intermediate non-magnetic ion such as oxygen as in the case of hematite. This interaction is now called superexchange and the quantum mechanical formalism has been developed by Anderson¹⁷. For cases where superexchange is appreciable the direct exchange is negligible since the magnetic ions are too widely separated. Therefore, in hematite, appreciable overlap occurs between the p electron states of the O^{2-} ion and the outer d electron states of the Fe^{+++} ion. In the O^{2-} ground state the two p electrons are antiparallel. Therefore, if the d electron states on two magnetic ions have appreciable overlap with the same O^{2-} ion, the spins have an antiparallel configuration as the lowest energy state. Since the p state is dumbbell shaped this interaction is appreciable only if the Fe-O-Fe bond are appreciably different from 90° . According to Gilleo¹⁸, for each Fe ion, there are nine appreciable interactions in hematite. Thus, the magnetic moments of the iron ions are orientated

in two antiparallel sublattices formed by alternate layers of ions parallel to the basal plane ((111) plane in rhombohedral representation).

Phenomenologically this interaction may be represented in the molecular field approximation¹⁴ by

$$\lambda \underline{M}_1 \cdot \underline{M}_2 \quad (6)$$

where \underline{M}_1 and \underline{M}_2 are the sublattice magnetizations and λ is the exchange constant. Then $\lambda \underline{M}_1$ represents the molecular field of one sublattice acting on the other. There is no evidence to suggest that there is anything but a negligible exchange interaction between spins of the same sublattice.

In some basically antiferromagnetic materials with sufficiently low symmetry, such as hematite, Dzialoshinskii showed by a thermodynamic argument that it was possible for the sublattices to cant towards each other without lowering the symmetry of the magnetic state. If the thermodynamic potential of a magnetic state is expanded in terms of spin variables, then under the magnetic symmetry group for the antiferromagnetic axis in the basal plane, terms of the form

$$l_x m_y - l_y m_x \quad (7)$$

are allowed. The vector $\underline{l} = (l_x, l_y, l_z) = \underline{S}_1 + \underline{S}_2 - \underline{S}_3 - \underline{S}_4$ defines the antiferromagnetic spin axis and the vector $\underline{m} = (m_x, m_y, m_z) = \underline{S}_1 + \underline{S}_2 + \underline{S}_3 + \underline{S}_4$ is the net magnetic moment. The spin vectors \underline{S}_i and the cartesian coordinate system to which all calculations will be referred are illustrated

on the rhombohedral unit cell in Fig. 1. The interaction can be expressed in the molecular field approximation by

$$\underline{D} \cdot (\underline{M}_1 \times \underline{M}_2) \quad (8)$$

where \underline{D} is the Dzialoshinskii canting vector parallel to the $[111]$ axis.

The microscopic origin of this interaction was formulated by Moriya⁴ who extended the formalism of Anderson¹⁷ to include spin-orbit effects in the superexchange interaction. This leads to an anisotropic term whose form is exactly similar to that of the molecular field approximation. Thus, the total exchange energy in hematite can be expressed, for the antiferromagnetic axis in the basal plane, as

$$F_e = \lambda \underline{M}_1 \cdot \underline{M}_2 + \underline{D} \cdot (\underline{M}_1 \times \underline{M}_2) = \lambda M^2 \cos 2\theta + \mathcal{D} M^2 \sin 2\theta \quad (9)$$

where θ is the canting angle and $|\underline{M}_1| = |\underline{M}_2| = M$ is the sublattice magnetization. Minimizing F_e with respect to θ gives the canting angle as

$$\theta_D = \frac{\mathcal{D} M}{2 \lambda M} = \frac{H_D}{2H_e} \quad (10)$$

where H_e is the exchange field and H_D is the canting field.

For pure hematite, resonance experiments^{19,20} give values of $\mathcal{D} M \sim 2.2 \times 10^4$ Oe and from susceptibility measurements^{21,22}

$\lambda M \sim 10^7$ Oe. Thus, the canting angle is $\theta_D \sim 1.1 \times 10^{-3}$

radians. The spontaneous moment $m = 2M \theta_D$, from static measurements^{23,24} has values ~ 2.0 emu/cc. A value of $M = 880$ emu/cc obtained by Mössbauer technique,²⁴ gives a value of m

~ 2.1 emu/cc which agrees with the static measurements.

Phenomenologically, the magnetocrystalline anisotropy energy F_K can be expressed²⁰ as

$$F_K = K_1 \sin^2 \theta + K_2 \sin^4 \theta + K_3' \sin^6 \theta + K_3 \sin^6 \theta \cos 6\phi \quad (11)$$

where θ is the angle the antiferromagnetic axis makes with the z axis and ϕ is the angle the projection of the antiferromagnetic axis in the x-y plane makes with the x axis. The first three terms are the uniaxial components and the last term is the three fold basal plane anisotropy. Microscopic origins for these anisotropies come from two main sources^{25,26}; the magnetic dipolar anisotropy and the single ion anisotropy due to spin-orbit effects. Neglecting the contributions to the 3 fold basal plane anisotropy the contribution of the magnetic dipolar anisotropy was calculated to have an effective field value $H_{MD} \sim -10^4$ oe at absolute zero which favours the antiferromagnetic axis parallel to the trigonal axis. However, the uniaxial contribution from the single ion anisotropy favours the basal plane orientation of the antiferromagnetic axis. It is the competition between these two anisotropies which produce the Morin transition. Thus, at the Morin transition the effective field value of the uniaxial part of the single ion anisotropy $H_{SI} = -H_{MD}$ and therefore, in the neighbourhood of the transition $H_{SI} \sim |H_{MD}|$. The effective uniaxial anisotropy field above is

then $H_{SI} - |H_{MD}|$. From spin flop data²⁰ $H_{K_1} = H_{SI} - |H_{MD}| = 217$ Oe at 0°K. Therefore, in the temperature range of interest between the Morin transition and room temperature, $0 < H_{K_1} < \sim 1000$ Oe gives a value for $K_1 = MH_{K_1}$ in the range 0 to 10^6 ergs/cm³.

The basal plane anisotropy field has been measured by microwave resonance^{20,27} to have an effective field value ~ 1.1 to 1.8×10^{-2} Oe. Therefore, the value of $K_3 = \frac{MH_{K_3}}{18}$ is ~ 0.5 to 1.0 ergs/cm³.

In general every magnetic state induced or spontaneous is accompanied by an anisotropic deformation of the crystal called magnetostriction. This deformation will exhibit the same symmetry as the crystal space group. Linear magnetostriction is the deformation induced by an applied magnetic field. In hematite, it was observed and measured by Anderson et al²⁸ for the purely antiferromagnetic state in hematite. Piezomagnetism, the inverse of linear magnetostriction has been discussed and also observed by various researchers.²⁹ However, the effect that is important to the domain properties is the spontaneous magnetostriction associated with the direction of the antiferromagnetic axis. The spontaneous magnetostriction can be found by minimizing the sum of the elastic energy and the magnetoelastic energy. The resulting equilibrium strain deformation is the spontaneous magneto-

striction. The elastic and magnetoelastic coupling coefficients are fourth order polar tensors and the energies associated with them are^{27,30} respectively

$$\begin{aligned}
 E_e = & \frac{1}{2}C_{11}e_{xx}^2 + C_{12}e_{xx}e_{yy} + C_{13}e_{xx}e_{zz} + 2C_{14}e_{xx}e_{yz} & (12) \\
 & + \frac{1}{2}C_{11}e_{yy}^2 + C_{13}e_{yy}e_{zz} - 2C_{14}e_{yy}e_{yz} \\
 & + \frac{1}{2}C_{zz}e_{zz}^2 \\
 & + 2C_{44}e_{yz}^2 \\
 & + 2C_{44}e_{xz}^2 + 2C_{14}e_{xz}e_{yz} \\
 & + (C_{11} - C_{12})e_{xy}^2
 \end{aligned}$$

and

$$\begin{aligned}
 E_{me} = & B_{11}\gamma_x^2e_{xx} + B_{12}\gamma_x^2e_{yy} & + B_{14}\gamma_x^2e_{yz} & (13) \\
 & B_{12}\gamma_y^2e_{xx} + B_{11}\gamma_y^2e_{yy} & - B_{14}\gamma_y^2e_{yz} \\
 & + B_{zz}\gamma_z^2e_{zz} \\
 & B_{41}\gamma_y\gamma_z e_{xx} - B_{41}\gamma_y\gamma_z e_{yy} & + B_{44}\gamma_y\gamma_z e_{yz} \\
 & + B_{44}\gamma_x\gamma_z e_{xz} + 2B_{41}\gamma_x\gamma_z e_{xy} \\
 & + 2B_{14}\gamma_x\gamma_y e_{xz} + 2(B_{11} - B_{12})\gamma_x\gamma_y e_{xy}
 \end{aligned}$$

where C_{ij} , B_{ij} , e_{ij} and γ_i are the elastic constants, the magnetoelastic coupling constants, the strains and the direction cosines of the antiferromagnetic axis respectively.

Then by forming $\frac{\partial}{\partial e_{ij}} (E_e + E_{me}) = 0$, a set of equations is

obtained from which the equilibrium strains can be found.

Assuming the spin axis is constrained to the basal plane

then the solutions to the equilibrium strains²⁷, after

correcting them³⁰ to give the exact solution, are:

$$e_{xx} = \frac{C_{33}(B_{11} + B_{12}) + 2C_{13}B_{33}}{2 [C_{33}(C_{11} + C_{12}) - 2C_{13}^2]} + \frac{[C_{14}B_{14} - C_{44}(B_{11} - B_{12})]}{2 [C_{44}(C_{11} - C_{12}) - 2C_{14}^2]} \cos 2\phi$$

$$= M + N \cos 2\phi$$

$$e_{yy} = M - N \cos 2\phi \quad (14)$$

$$e_{zz} = \frac{C_{13}(B_{11} + B_{12}) + (C_{11} + C_{12})B_{33}}{C_{33}(C_{11} + C_{12}) - 2C_{13}^2} = K$$

$$e_{xy} = N \sin 2\phi$$

$$e_{xz} = \frac{[2C_{14}(B_{11} - B_{12}) - (C_{11} - C_{12})B_{14}]}{4 [C_{44}(C_{11} - C_{12}) - 2C_{14}^2]} \sin 2\phi = L \sin 2\phi$$

$$e_{yz} = L \cos 2\phi$$

Physically this deformation can be interpreted²⁷ as consisting of three parts: firstly, a uniform deformation independent of the antiferromagnetic axis direction, secondly, a

contraction along the antiferromagnetic axis and an equal elongation in the basal plane perpendicular to it, and thirdly, a tilt of the trigonal axis towards the basal plane. The tilt arises from the e_{yz} and e_{xz} strains and since $e_{xz}^2 + e_{yz}^2 = \text{constant}$ the tilt will be constant.

However, the tilt will rotate through twice the angle in the opposite direction to a antiferromagnetic axis rotation and for the antiferromagnetic axis along the x axis the tilt will be in the y-z plane.

A more general form for the spontaneous magnetostriction³⁰ along an arbitrary direction, given by the direction cosines

$\alpha_x, \alpha_y, \alpha_z$, is

$$\begin{aligned} \lambda_\sigma = & (\alpha_x^2 + \alpha_y^2)M(1 - \gamma_z^2) + (\alpha_x^2 - \alpha_y^2) \left[N(\gamma_x^2 - \gamma_y^2) + 2U\gamma_y\gamma_z \right] \\ & + \alpha_z^2K(1 - \gamma_z^2) + 4\alpha_x\alpha_y(N\gamma_x\gamma_y + U\gamma_x\gamma_z) \\ & + 4\alpha_x\alpha_y(L\gamma_x\gamma_y + V\gamma_x\gamma_z) \\ & + 2\alpha_y\alpha_z \left[L(\gamma_x^2 - \gamma_y^2) + 2V\gamma_y\gamma_z \right] \end{aligned} \quad (15)$$

Using the elastic constants measured by Voigt³¹ the values of K, L, M, N, U and V were measured to be $2.5 \pm 10\%$, $-8.5 \pm 12\%$, $5.6 \pm 10\%$, $-3.4 \pm 10\%$, $14 \pm 20\%$ and $\pm 10 \pm 40\% \times 10^{-6}$ respectively. The values estimated by Tasaki et al³⁰ from

the measurements of Urquhart et al³² are in reasonable agreement with these values.

The contribution to the free energy from magnetoelastic coupling is

$$F_{\sigma} = E_e + E_{me} \quad (16)$$

The validity of this equation in the form derived is open to question³³ especially if applied to the case of non-uniform strains in magnetic materials.

Any other contributions to the magnetic free energy such as defects may be included in F_0 . However, contributions from defects generally cannot be expressed analytically and hence can only be dealt with qualitatively.

B. Principles of Domain Formation.

Suppose that the applied field is zero and that contributions to F_0 can be ignored for a single crystal then the free energy of the crystal can be expressed as

$$F_T = F_D + F_e + F_{\sigma} + F_K \quad (17)$$

where the analytic forms for each term are as previously discussed. Clearly the terms F_e , F_{σ} and F_K are a minimum for a uniform magnetization. The only term that benefits from a non-uniform magnetization is the magnetostatic self energy due to uncompensated poles. Thus, any non-uniformity in the magnetization, in order to reduce free pole energy, necessarily increases F_e , F_{σ} and F_K . Therefore, non-uniform

distributions of \underline{m} are solutions for the minimization of F_T . The equation for the free energy can be converted into a differential equation satisfying certain boundary conditions. Continuous solutions for $\underline{m} = \underline{m}(\underline{r})$ can then be obtained exactly from these differential equations for very special cases of geometry only and no magnetoelastic and magneto-crystalline anisotropies. In general however, solutions will only be obtained by resorting to approximate methods. These forms of solutions are the field of micromagnetics³³.

However, a special approximation, which has wide validity experimentally, is the domain-wall approximation. A domain wall is a narrow transition layer between two regions each with uniform magnetization but in different directions. Micromagnetics indicate that there exist an infinite set of solutions for zero energy domain wall configurations. Thus, criteria for the applicability of the domain wall approximation is a domain wall of low energy compared to magnetostatic energy and small width compared to domains or regions of uniform \underline{m} . The domain regions in turn must be small compared to dimensions of crystal.

The domain wall approximation has now effectively reduced the problem to the solution of two one dimensional problems. Firstly, the problem is the minimization of the free energy of a domain wall under a physically intuitive

model and secondly a minimization of the sum of the magnetostatic energy and total domain wall energy again under some physically intuitive model of domain wall distribution.

The first experimental evidence for domain walls was given by Bitter³⁴. A successful model for these walls was first put forward by Bloch³⁵. In this model, the ferromagnetic moment \underline{m} slowly rotates across the wall under the condition that $\text{div } \underline{m} = 0$. This implies that the component of \underline{m} perpendicular to the wall remain constant. A second model was predicted by Néel³⁶ for thin films. In sufficiently thin films the free pole energy of the domain wall at the crystal surface is no longer negligible and it is more favourable for $\text{div } \underline{m}$ to be a maximum, thus, eliminating the uncompensated poles from the surface of the thin film. In bulk crystals the Bloch model is generally the more applicable, however, the condition $\text{div } \underline{m} = 0$ may have to be relaxed in some cases because of special crystal anisotropies or imperfections. But for bulk crystals the tendency will be for $\text{div } \underline{m}$ to be a minimum since the wall thickness will in general be much smaller than either of its other two dimensions.

It has been found using these wall models and rather simple models of domain structure (for example: the stripe and checkerboard models of Kittel³⁷ and the honeycomb model of Kaczer et al³⁸) that reasonable agreement can be obtained

with the actual domain structure observations.

There are two main techniques of calculating the energy of a plane domain wall depending on the rigour desired. The first simpler but less rigorous technique is to assume a domain wall of width δ and to assume the rate of change of direction of the magnetization across the wall is constant. Under this approximation each term in the free energy can then be dealt with separately and each will result in some function of δ . The domain wall energy can then be minimized with respect to δ .

The contribution of the exchange energy can be dealt with either from a microscopic approach or molecular field approximation approach. Since the terms in the exchange are usually measured in terms of the molecular field approximation then it will be convenient to perform the calculation this way. The exchange is given by equation (9) which is more complicated than the normal exchange in ferromagnets. However, the canting interaction will produce no free energy contribution due to the wall and hence the domain wall free energy is¹⁴

$$f_e = A \int [(\nabla\alpha_1)^2 + (\nabla\alpha_2)^2 + (\nabla\alpha_3)^2] dv \quad (18)$$

where $A = \frac{1}{2}\lambda M^2 a^2$ and α_i are the direction cosines of the magnetization relative to an appropriately chosen coordinate system. The constant a is the distance between successive

layers of magnetic atoms. The neglect of the canting interaction can be verified by the following simple argument. Suppose the two sublattice moments are rotated towards each other a small angle $\pm\theta$ in the basal plane from their equilibrium configuration, then the increase in free energy is

$$\lambda M^2 \cos(2\theta_0 \pm \theta) + 2M^2 \sin(2\theta_0 \pm \theta) - \lambda M^2 \cos 2\theta_0 - M^2 \sin 2\theta_0 \quad (19)$$

This reduces simply to $-\frac{1}{2}M^2\theta^2$ on replacing $2M^2$ by $2\lambda M^2\theta_0$ according to equation (10). This argument could be generalized to include an arbitrary rotation of the sublattice moments. Consequently the canting term can be ignored and the domain wall free energy can be calculated assuming a perfectly anti-ferromagnetic arrangement with molecular field approximation free energy of $\lambda \underline{M}_1 \cdot \underline{M}_2$.

The contribution to the wall energy of the magneto-crystalline anisotropy $F_K = F_K(\theta, \phi)$ is given by

$$f_K = \int [F_K(\theta, \phi) - F_K(\text{domain})] dv \quad (20)$$

In general, the domains will have magnetization directions giving $F_K(\text{domain}) = 0$. This expression assumes that adjacent domains have the same magnetocrystalline free energy.

The expression for the magnetoelastic free energy of the domain wall is exactly analogous to equation (20). The

usual assumption in calculating the magnetostrictive free energy is that there is no change in the state of strain across the domain wall. Thus, the expression for the magnetostrictive free energy becomes

$$f_{\sigma} = \int [E_{me}(\gamma_x, \gamma_y, \gamma_z) - E_{me}(\text{domain})] dv \quad (21)$$

The remaining term contributing to the free energy is the magnetostatic self energy. If the wall satisfies $\nabla \cdot \underline{m} = 0$ then this term is negligible in bulk crystals since uncompensated poles produced by the wall will occur only at the intersection of the domain wall with the boundary of the crystal. If however $\nabla \cdot \underline{m} \neq 0$ then there will be uncompensated poles throughout the wall. In this case it is necessary then to calculate this contribution which is given by equation (3) and where \underline{H} is obtained from

$$\text{div } \underline{H} = -4\pi \text{div } \underline{m} \quad (22)$$

for an infinite plane wall.

The second method of finding the domain wall energy is essentially a refinement of the first method. Instead of assuming boundary conditions for the wall, the free energy of the wall is minimized by making the integrand of the expression for the domain wall free energy, $f_w = f_e + f_K + f_{\sigma} + f_D$, satisfy Euler's equations. For the most general wall model the magnetization \underline{m} will depend on the polar coordinates θ, ϕ relative to a z axis perpendicular

to the domain wall. The solution to Euler's equations then gives the functional form for θ and ϕ which can be substituted back into the integrands and the integrals evaluated. The solution to this problem results in a region of infinite width over which the direction of magnetization changes, but the effective width of the wall will still be small. Consequently, there is a certain arbitrariness in assigning the wall width.

Wall models, such as Bloch and Néel walls, require only one of the variables θ , ϕ to specify the change in direction of the magnetization. In fact, the author is not aware of any derivations other than those where only one variable is required. Probably such a derivation would be quite difficult to solve because of coupled Euler equations.

For the Bloch wall where θ is constant the problem is relatively simple if the magnetostriction can be neglected or reduced to the same form as the magnetocrystalline anisotropy. Then the energy of the wall is given by^{14,42}

$$f_w = \int_{-\infty}^{\infty} \left[A \sin^2 \theta \left[\frac{d\phi}{dz} \right]^2 + F_K(\phi) \right] dz \quad (23)$$

which gives Euler's equation as

$$\frac{dF_K(\phi)}{d\phi} - 2A \sin^2 \theta \frac{d^2 \phi}{dz^2} = 0$$

From the boundary conditions $\phi = \pm \frac{1}{2}\pi$ at $z = \pm\infty$ the solution to Euler's equation is

$$A \sin^2 \theta \left[\frac{d\phi}{dz} \right]^2 = F_K(\phi) \quad (25)$$

Substitution into equation (23) gives

$$f_w = \int_{-\phi}^{\phi} 2\sqrt{A} \sin \theta [F_K(\phi)]^{\frac{1}{2}} d\phi \quad (26)$$

For the 180° Bloch wall in a uniaxial ferromagnet the wall energy is

$$f_w = 4\sqrt{AK} \quad (27)$$

Solving equation (24) gives

$$z = \sqrt{\frac{A}{K}} \log \tan \phi \quad (28)$$

Therefore, the wall width is chosen to be

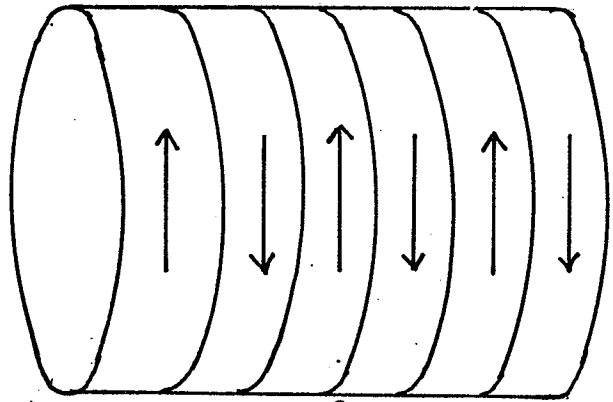
$$\delta = \pi \sqrt{\frac{A}{K}} \quad (29)$$

since approximately 75% of the change in ϕ takes place in this width.

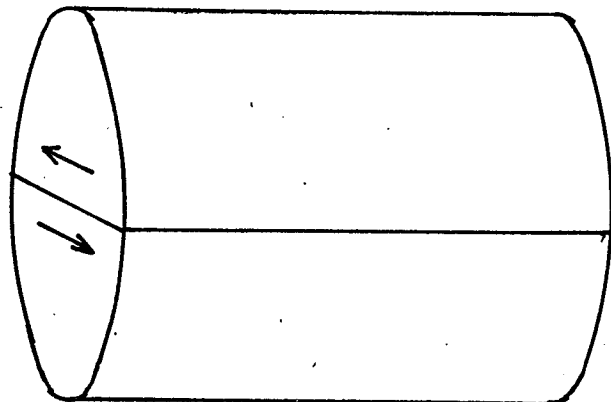
Kaczer⁴³ and Farztdinov⁴⁴ both give general treatments of domain walls in hematite under the assumption that magnetostriction can be ignored and that the moment is constrained to the basal plane. The wall models considered are illustrated in Fig. 2. Walls parallel to the basal plane can be treated very easily by the method given by equations (23) to (26). The walls perpendicular to the basal

Figure 2.

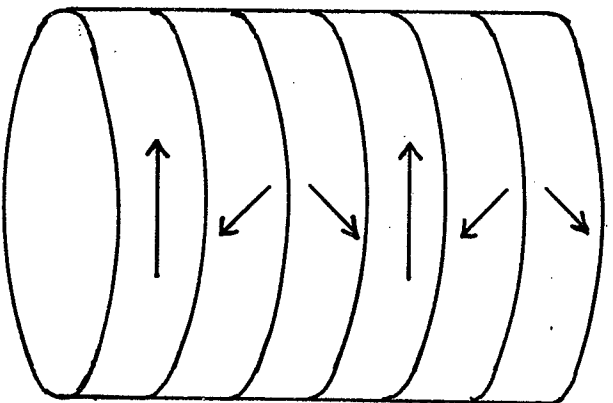
Domain and domain wall models according to Kaczer and Farztdinov. For a cylindrical specimen, with axis perpendicular to the basal plane, the following domain wall configurations are illustrated: (a), (b) and (c) show 60° , 120° and 180° walls parallel to (111) plane respectively and (d), (e) and (f) show 60° , 120° and 180° walls perpendicular to (111) plane respectively. The magnetocrystalline anisotropy is assumed to be non-negligible in the basal plane and effectively infinite out of the basal plane.



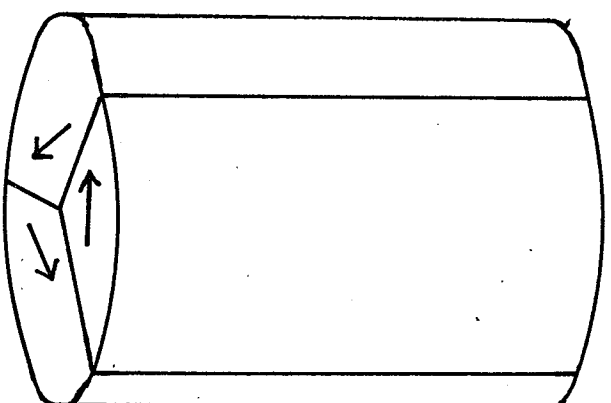
(c) 180°



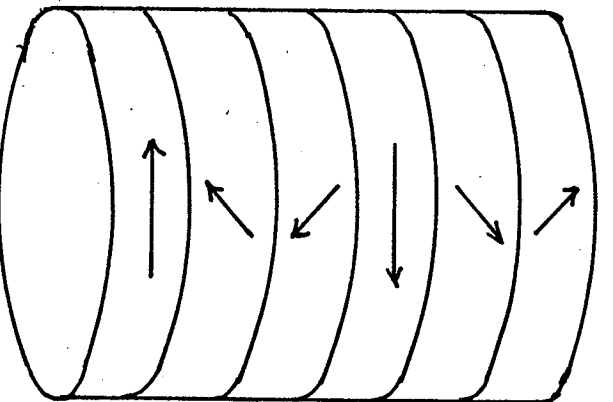
(f) 180°



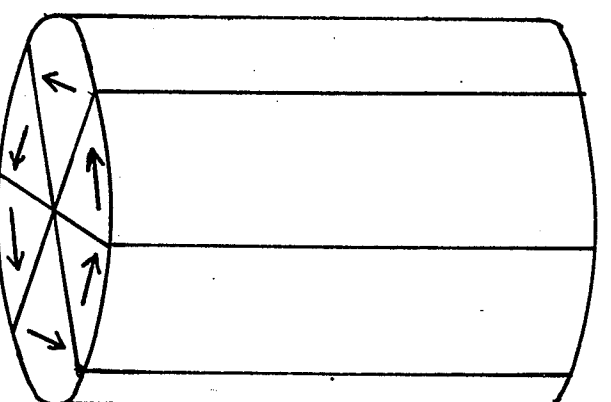
(b) 120°



(e) 120°



(a) 60°



(d) 60°

plane lead to walls with $\text{div } \underline{m} \neq 0$. The domain width of such wall is easy to calculate following the methods of Kaczer⁴⁵. However, the wall energy diverges now because of the magnetostatic energy for an infinite plane wall.

Physically this would not occur since the walls are of finite size. However, using a technique developed earlier⁴⁶ Kaczer obtains wall energies given in Table I. Also, given in Table I are the domain wall energies and magnetostatic energies for all the configurations illustrated in Fig. 2. The wall energies are in agreement with those cases Farztdinov calculated. To calculate the magnetostatic energies of domain structures Kaczer uses the standard technique of solving Laplace's equations for the boundary conditions given by the resulting distribution of free poles.

Table I. Domain Magnetostatic and Wall Energies.

Type of Wall	Wall energy		Magnetostatic energy	
	Wall \perp to basal plane	Wall \parallel to basal plane	\perp case	\parallel case*
180°	$4\sqrt{AK_3} \sqrt{\frac{2\pi m^2}{K_3}}$	$4\sqrt{AK_3}$	$4r^2 m^2$	$1.34rdm^2$
120°	$1.37\sqrt{AK_3} \sqrt{\frac{2\pi m^2}{K_3}}$	$\frac{8}{3}\sqrt{AK_3}$	$1.48r^2 m^2$	$1.24rdm^2$
60°	$0.18\sqrt{AK_3} \sqrt{\frac{2\pi m^2}{K_3}}$	$\frac{4}{3}\sqrt{AK_3}$	$0.21r^2 m^2$	$1.45rdm^2$

(* r = radius of cylinder, d = domain width)

Farztdinov only considers the magnetostatic energy of 180° walls in a rectangular block both parallel to the basal plane giving a stripe domain configuration. The magnetostatic energy for such a configuration is³⁷

$$F_D = 1.7m^2d \quad (30)$$

where d is the width of the domains. The domain wall energy per unit volume for such a configuration is

$$F_w = f_w \frac{L}{d} = 4\sqrt{AK} \frac{L}{d} \quad (31)$$

where L is the length of the domain along the magnetization direction. Minimizing the sum of equations (30) and (31) with respect to d gives

$$d = \left[\frac{4\sqrt{AK}L}{1.7m^2} \right]^{\frac{1}{2}} \quad (32)$$

By using a value of $K = K_3 = 3 \text{ ergs/cm}^3$,

Farztdinov gives the values for the domain parameters of such a configuration as $f_w = 2 \times 10^{-2} \text{ ergs/cm}^2$, $d = 1 \text{ mm}$ and $\delta = 10^{-2} \text{ mm}$, which he concludes are in agreement with the current observations.⁵⁻⁷ A value of $2.3 \times 10^{-8} \text{ cms}$ for the distance between layers of iron atoms parallel to the basal plane and the values given previously for λ_M , M , m and K_3 give values of $f_w \sim 10^{-2} \text{ ergs/cm}^2$, $\delta \sim 5 \times 10^{-2} \text{ mm}$ and $d \sim 0.4 \text{ mm}$, which are in reasonable agreement with Farztdinov.

C. Principles of Bitter Figure Technique.

The original technique for observing magnetic domain

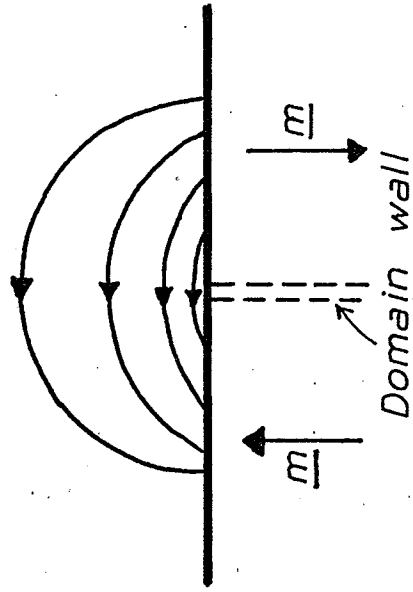
structures is the Bitter³⁴ pattern technique. This technique is still the most widely applicable and simplest technique compared to the more recently developed Faraday and Kerr optical, electron microscope and the various other techniques. A comparison and discussion of the various techniques is given by J.F. Dillon Jr.⁴⁷.

The principle behind the colloid technique is the preferential migration of magnetic particles toward regions of highest flux density, when they are suspended colloiddally. For multi-domain particles the force experienced by the particles is equal to $\frac{1}{2}v\chi\nabla H^2$ where χ is the susceptibility of the particles, H the stray magnetic field, and v is the volume of the particle⁴². Therefore, the force acting on the particle is towards regions of highest field and is a maximum for maximum field gradient. The particles are therefore trapped in regions of maximum field. The consequences⁴⁸ of this for domain studies are illustrated in Fig. 3. The field above the surface of a magnetic crystal will trap particles near the crystal surface at the domain boundary whether the field is created by flux leakage at the domain wall or by flux linkage between adjacent domains.

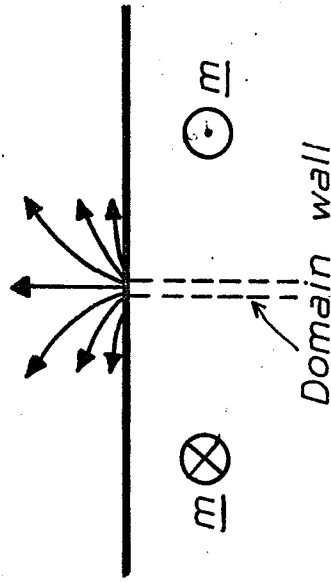
If a small uniform field is applied to the crystal in such a way that it is antiparallel to the field due to the domain boundary, then at a sufficiently large value the

Figure 3.

Fringing fields about domain walls at crystal surface.
Flux leakage and flux linkage are illustrated in (a)
and (b) respectively.



Flux linkage



Flux leakage

region near the wall is no longer a region of higher field. Therefore, there will be no preferential deposit of colloid at the domain wall. This allows the mechanism which is producing the Bitter patterns to be determined and also gives some idea of the intensity of the magnetic field at the wall.

III. Experimental Technique

A. Crystals and Their Preparation.

Synthetic single crystals of hematite, grown by the flux technique^{12,13}, were used for all experiments. Some pure and the Ga, Al and Ti doped crystals had been grown previously at the University of Minnesota¹³. However, the Rh doped and the majority of the pure specimens were grown here. The amount of dopant present in the crystals ranged up to 2.5 mole % depending on the type of dopant.

On removal of the hematite crystals from the flux, they varied in size from a few millimetres to 2-3 cm and had up to 5 smooth plane surfaces which were lightly mottled by flux etching. These faces were always (110) faces. The other areas of crystal surface were irregular and appeared to be formed by the termination of growth of successive (110) plates which formed the smooth (110) surfaces. The angle between different (110) faces was $\sim 86^\circ$ so that apart from the irregular faces the crystals would appear like a slightly distorted rectangular box.

Surfaces of crystal with a chosen orientation could be obtained by cutting the crystals with a Micro-Matic Precision Wafering Machine³⁹ after crystal orientation on a goniometer¹³. The crystal orientation on the goniometer could be performed by the standard Laue x-ray technique^{13,40}. Sample Laue photographs of $(1\bar{1}0)$ and $(11\bar{2})$ surfaces are illustrated in

Fig. 4, and photographs of (100), (110) and (111) faces are given elsewhere¹³. The $(\bar{1}\bar{1}0)$ and $(1\bar{1}\bar{2})$ planes were of particular importance since they are perpendicular to the basal plane and contain the easy and hard directions respectively of the weak ferromagnetic moment.

The crystal orientation could be done, in general, just as accurately and far more expediently by using a protractor and orienting the well formed (110) face of the crystal to specific angles on the goniometer. The geometry of this technique is illustrated in Fig. 5.

Before colloidal domain observation, crystal surfaces required mechanical polishing. This was accomplished on an AB Low speed polisher⁴¹ using the procedure⁴⁹ given in Table II.

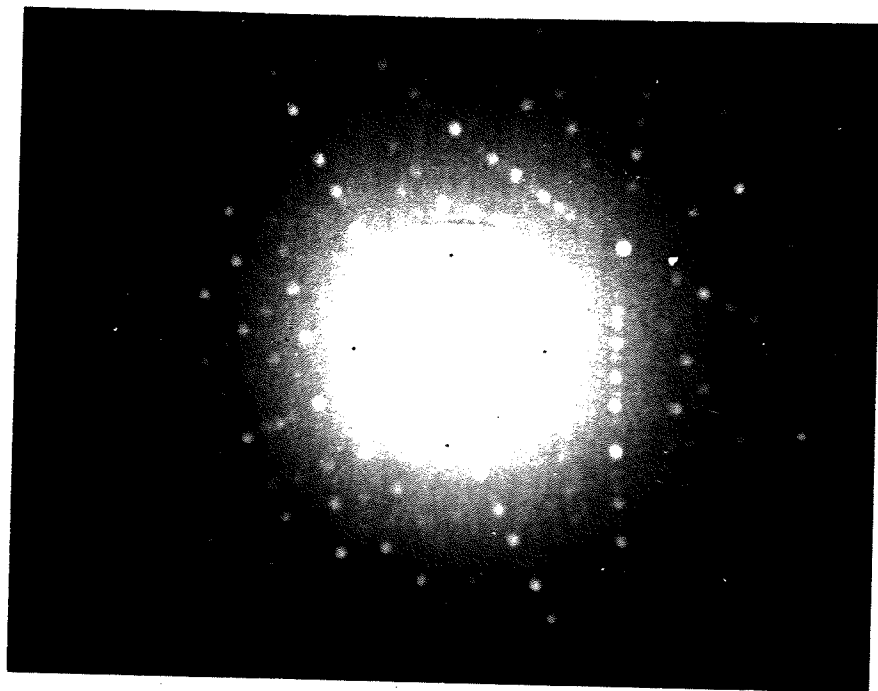
Table II: Mechanical Polishing Procedure

Polishing Step	Polishing wheel and surface	Lubricant	Polishing Agent
Fine grinding	Concentrically grooved copper	AB polishing oil	5 Al ₂ O ₃
Rough polishing	Bronze with AB Texmet		9 Diamond
Fine polishing			1 Diamond
Buffing	Bronze with AB Microcloth	Water	0.05 Gamma Alumina

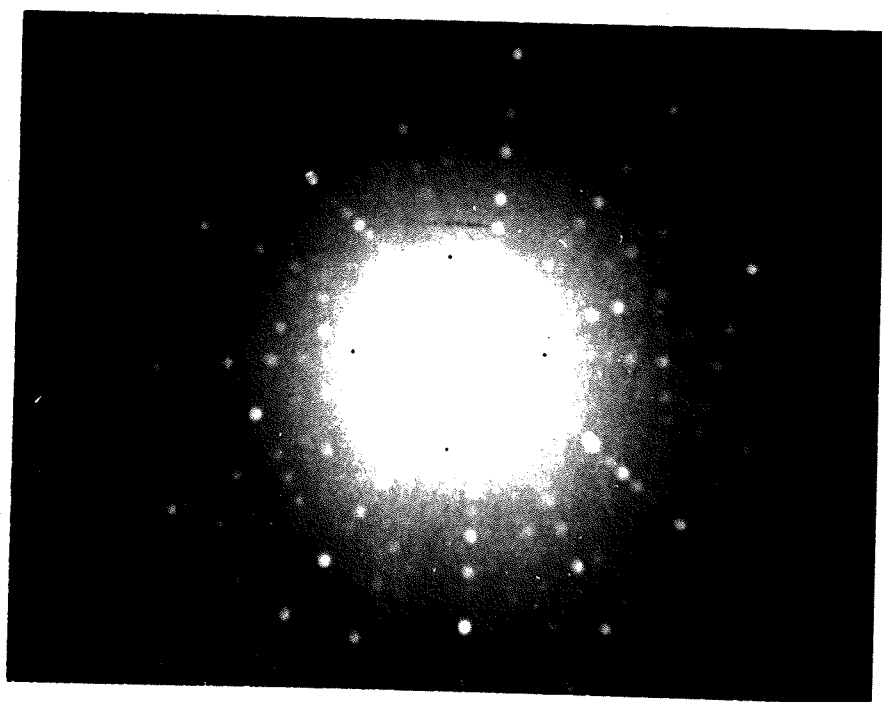
Each step required about 5-15 minutes until traces of previous step were removed.

Figure 4.

X-ray Laue photographs showing planes perpendicular to the (111) plane. The hard or $(11\bar{2})$ and easy or $(1\bar{1}0)$ planes for the magnetization are illustrated in (a) and (b) respectively.



(a) $(11\bar{2})$ plane



(b) $(1\bar{1}0)$ plane

Figure 5.

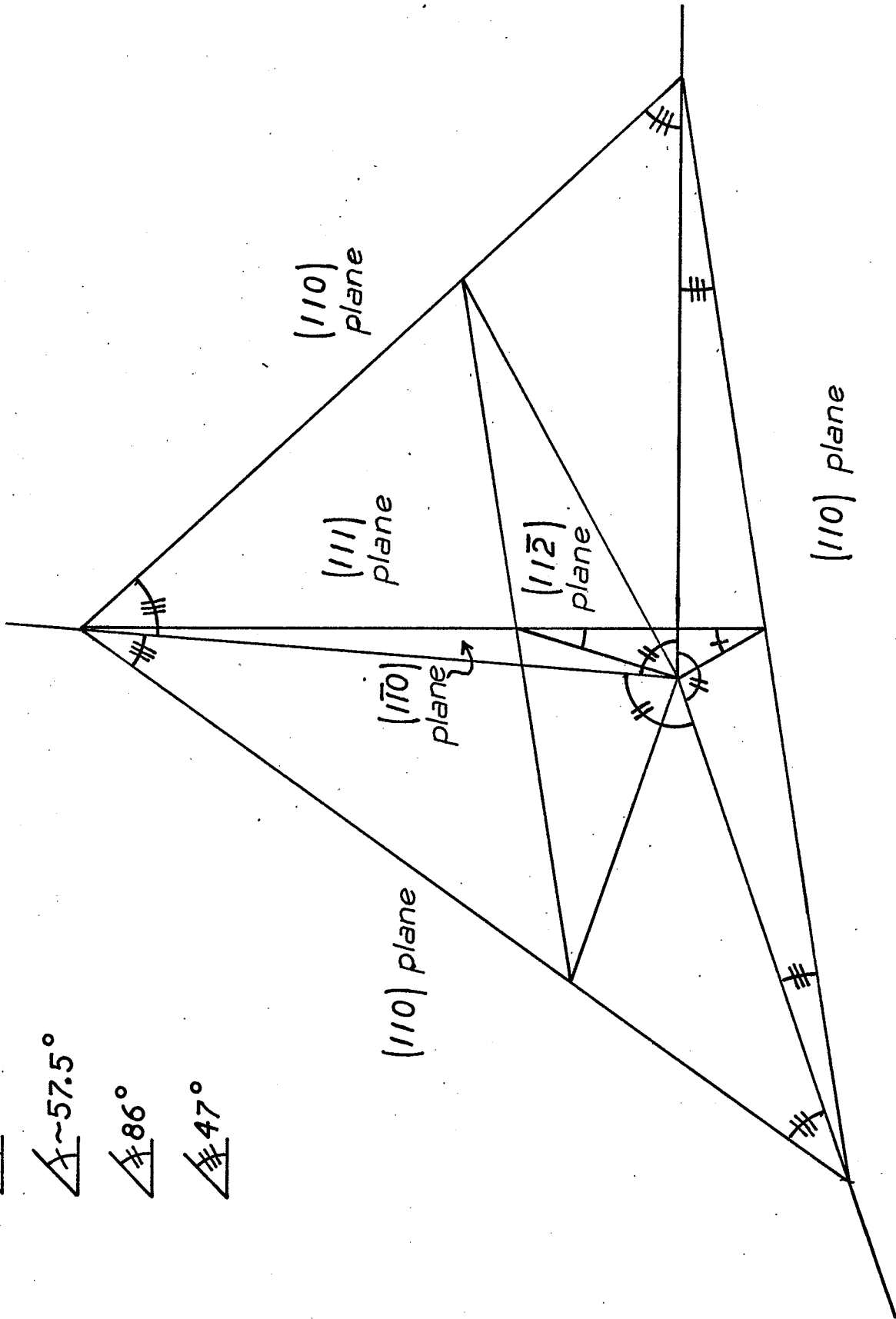
The geometry of $(1\bar{1}0)$ and $(11\bar{2})$ planes relative to the (110) planes.

$\triangle 90^\circ$

$\triangle \sim 57.5^\circ$

$\triangle 86^\circ$

$\triangle 47^\circ$



Thin sections of a polished surface from 50μ - 500μ thick could be obtained with the wafering machine by glueing the crystal surface with quartz cement to a 2" x $2\frac{1}{2}$ " glass slide, which could be readily mounted in the wafering machine's vertical holder and a thin section then cut off. One difficulty encountered in this procedure was ensuring a thin section of uniform thickness. This appeared to be just a matter of technique.

In general, before domain observation, the crystals were carefully annealed in air in a box-type furnace at temperatures from 1000° C to 1200° C. A 1000° C anneal for 24 hours followed by furnace cooling was sufficient to produce regular domain structures. However, longer and higher temperature anneals did appear to result in further small improvements or changes in the domain structure. They also had the advantage that the 1μ diamond paste polishing scratches were removed and therefore, the buffing step in polishing could be dispensed with. From all microscopic investigations and measurements of the properties of hematite, there was never any evidence to suggest a change of hematite to another iron oxide form. However, flux inclusions occasionally caused etching problems on the polished surfaces.

The rate of cooling the crystal from the anneal temperature did not appear too critical and furnace cooling in the box-type furnace appeared sufficient. However, in the 2" tube furnace, since the furnace has a much lower

thermal capacity the rate of cooling had to be controlled in order to reduce it sufficiently.

B. Preparation of the Magnetite Colloid.

In order to observe the domains on the surface of the crystal from room temperature down to -40°C a magnetite colloid in acetone was used. The recipe was obtained in a private communication with M. Blackman, to whom the author would like to express his appreciation. Fine magnetic particles are produced by precipitation from a boiling solution of 5.00 gm NaOH in ~ 450 cc H_2O with a mixture of 5.40 gm $\text{FeCl}_3 \cdot 6\text{H}_2\text{O}$ in 50 cc H_2O and 2.78 gm $\text{FeSO}_4 \cdot 7\text{H}_2\text{O}$ in 50 cc H_2O . The colloid is boiled for $\sim \frac{1}{2}$ hour and then filtered off on cooling. It is thoroughly washed with water and then ethyl alcohol. The precipitate is now boiled in ethyl alcohol and after filtering off is thoroughly washed with acetone. The precipitate is finally suspended in a solution of equal amounts of acetone and acetone saturated with ethyl cellulose by an ultrasonic cleaner. This gives a stock colloidal solution which can be diluted with acetone to the desired particle density for domain observations. Typically, the dilution is between 20 to 5 parts acetone to one part stock solution. After dilution, the colloid allows domain observation down to -30° to -40°C

depending on the amount of dilution.

This colloid appeared to deteriorate with age and after 4 to 6 months was no longer any use even if stored in a dry atmosphere. This problem was eliminated, giving a colloid that has not deteriorated at all, by a change in the precipitation technique to that outlined by Chikazumi⁵⁰. The 2.78 gm $\text{FeSO}_4 \cdot 7\text{H}_2\text{O}$ is replaced by 2.00 gm $\text{FeCl}_2 \cdot 4\text{H}_2\text{O}$ and instead of bringing the solutions to boiling, the NaOH solution is added to the rapidly stirred mixture of the salt solutions which has been carefully heated to 40°C . This technique also ensures the finest magnetite particle size.

C. Magnetite Colloid Domain Observations.

1. At Room Temperature.

The domain patterns at crystal surfaces are observed by immersing the surface in colloid and observing the distributions of the colloidal particles which aggregate on the surface. Since the particles take from $\frac{1}{4}$ to several hours to reach equilibrium in depositing at the domain boundaries the colloid must be prevented from evaporating. The immersion, therefore, was done by suitably mounting the crystal in an aluminum vessel with a machined lip. The vessel was filled with colloid to overflowing and quickly covered with a glass slide. After a small acetone evaporation

the ethyl cellulose sealed the slide to the vessel preventing further evaporation.

The domain patterns could now be observed at room temperature with and without an applied field. The field was supplied by 15 cm diameter Helmholtz coils which gave a maximum field of 100 oe at 10 amp. The coils could be mounted on the microscope stage with their axis parallel or perpendicular to the crystal surface.

The domain patterns are observed and photographed with a Leitz Ortholux Research Microscope⁵¹. The optical system most suitable was either the 3.5x or the 11x Ultropak incident light objectives with 8x eyepieces. These objectives allowed the large working distances ~5 mm which were necessary. The 11x objective was the most widely used since the 3.5x objective had too low a resolution to show any domain pattern except extremely dense colloidal distributions. This difficulty could be partially overcome by slightly tilting the crystal surface until the contrast became inverted.

Higher magnification objectives were not suitable partly because of working distances but mainly because they had too limited a field of view. The photographs were obtained from a Polaroid 2 3/4" x 3 1/4" Pack Back fitted to the microscope and taking Polaroid film type 107.

Domain pattern observations were made while shear and

compressive stresses were applied to either bulk or thin section crystals. Forces from zero up to 50 kgm and from zero up to 2 kgm were applied to bulk and thin section crystals respectively, while they were immersed in colloid in the manner illustrated in Fig. 6. The effect of stress on domain behaviour in magnetic fields was also observed.

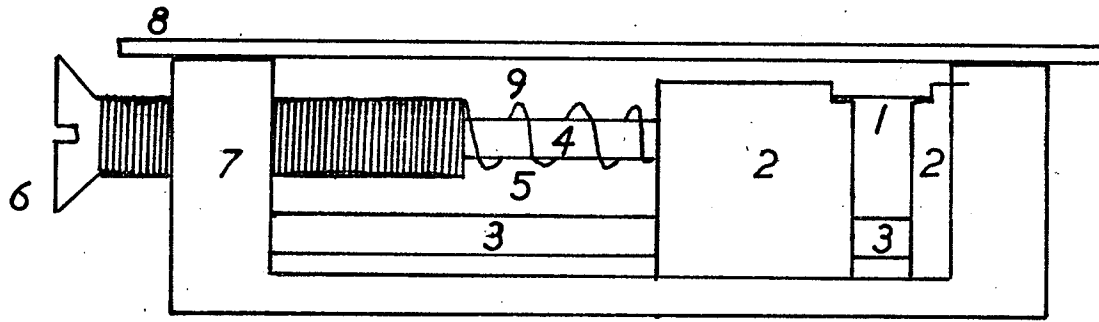
2. Between -40°C and 50°C .

To observe the domains at the temperatures when crystals underwent the Morin transition required construction of the apparatus illustrated in Fig. 7. The sample chamber is cooled or warmed by thermoelectric modules⁵². In order to avoid head leaks to the sample chamber, it was supported entirely on the thermoelectric modules and enclosed in a vacuum chamber which in turn was designed to provide the support for the other sides of the thermoelectric modules. The temperature of the vacuum chamber and of the one side of the modules was kept constant by tap water cooling. This was quite adequate since the apparatus was not meant to hold the temperature constant over long periods. Therefore, although the cooling water might have a daily variation in temperature of 1° - 2°C , the short term fluctuations were unobservable. The sample and vacuum chamber windows were glued in with epoxy and designed to be self sealing under

Figure 6.

Schematic illustrating technique of applying stresses to crystals while immersed in colloid.

1. Rectangular crystal thin section, 2. Nylon crystal supports, 3. Nylon support guide pins, 4. Spring guide pin, 5. Spring, 6. Spring tension adjustment screw, 7. Stress apparatus wall, 8. Cover glass, 9. Colloid.



Stress apparatus cross-section

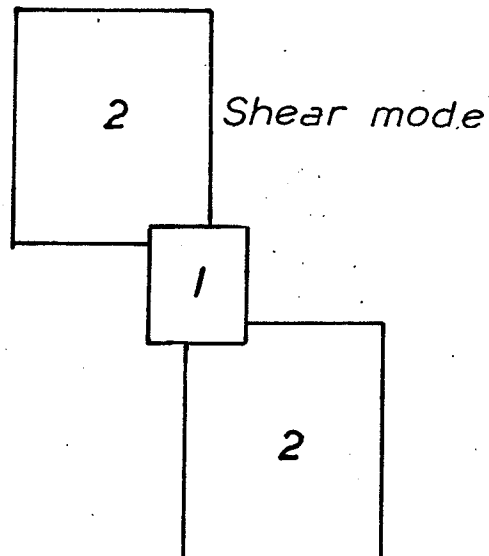
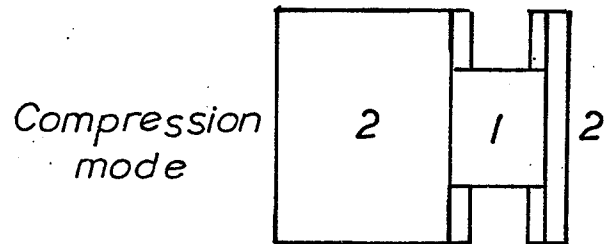
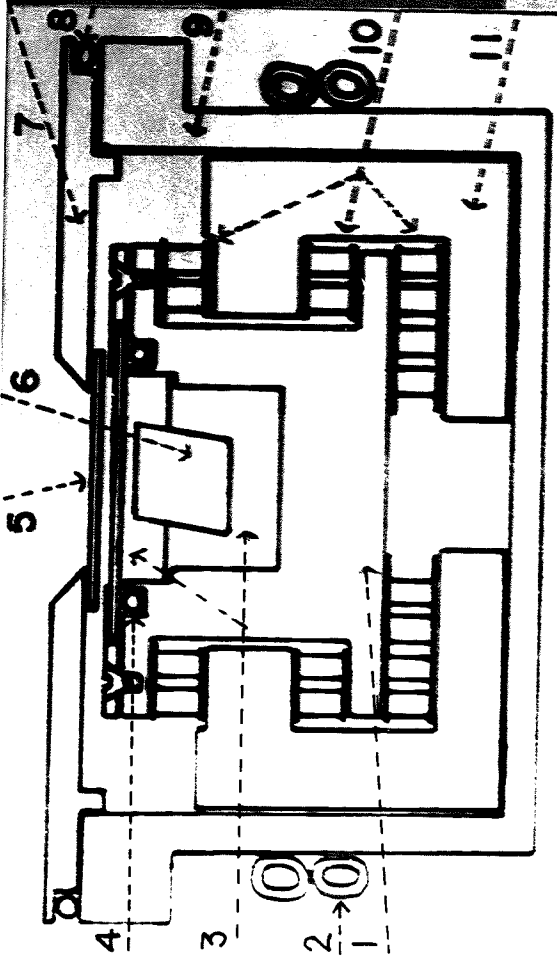


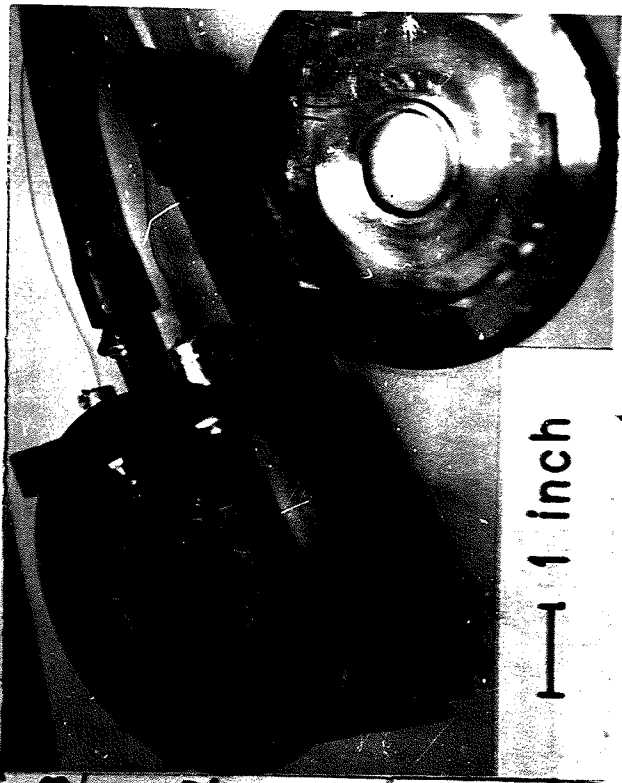
Figure 7.

Apparatus for controlling the temperature of crystals while immersed in colloid.

1. Cooling chamber walls.
2. Tap water cooling pipes.
3. Magnetite Colloid.
4. Teflon o-ring.
5. Glass windows.
6. Hematite crystal.
7. Vacuum chamber lid.
8. Viton o-ring.
9. Vacuum chamber walls.
10. Thermoelectric cooling modules.
11. Support blocks for modules.



Cross-section
a



1 inch
b

vacuum.

The power for the modules was supplied by a 6v, 15 amp stabilized current supply which was motorized to give a constant or a slowly increasing or decreasing current. Slowly changing the current causes the equilibrium temperature of the sample chamber to slowly drift at temperature rates of 1 - 5°C/hr. The domain patterns were observed as the crystals passed through their Morin transition temperatures if they lay in the range -30° to 50°C. The temperatures, monitored by a copper-constantan thermocouple, showed that the short term fluctuations in temperature were less than 1/50°C.

D. Crystal Physical Properties.

1. X-ray Diffraction.

Carefully chosen pieces of crystal of various dopings were ground up as finely as possible in an agate mortar and pestle. X-ray powder diffraction pictures were obtained using a 57 mm Debye-Scherrer Camera⁴⁰. Radiation from an Fe tube required a six hour exposure for powder pictures obtained with Kodak Medical X-ray Film.

The relative difference of the lattice parameters of differently doped crystals, compared to the lattice parameters of pure hematite, were measured from the powder pictures.

2. X-ray Fluorescence.

Using the x-ray fluorescence attachment to the Philips X-ray Generator the amount of Rh doping in the hematite single crystals was determined by the comparison with standards technique⁵⁶. The amount of Ga, Al and Ti dopings had been determined previously elsewhere²⁰. The standards for comparison were made by grinding up given amounts of $\alpha\text{-Fe}_2\text{O}_3$ and Rh_2O_3 reagent grade powders in suitable ratios to produce homogenous mixtures. These powders were formed into thin $1\frac{1}{4}$ " discs by an AB Specimen Mount Press⁵¹ using 1 gm of AB Transoptic Powder as a binder. Similarly carefully chosen amounts of Rh doped single crystal were made into discs after the single crystal had been ground up to give a brownish-purple powder. The K_α and L_α fluorescent radiation of the Fe and Rh respectively from the samples and standards was analysed by obtaining diffractometer traces. From these the peak height or intensity can be measured to give the relative amount of Fe to Rh in the specimens. Thus, if the Fe intensities are all normalized to one, assuming only small Rh dopings, the amount of Rh doping in the crystals compared to the standards is determined.

3. Electron Microprobe Analysis.

A crystal of each doping was cut to give a surface which

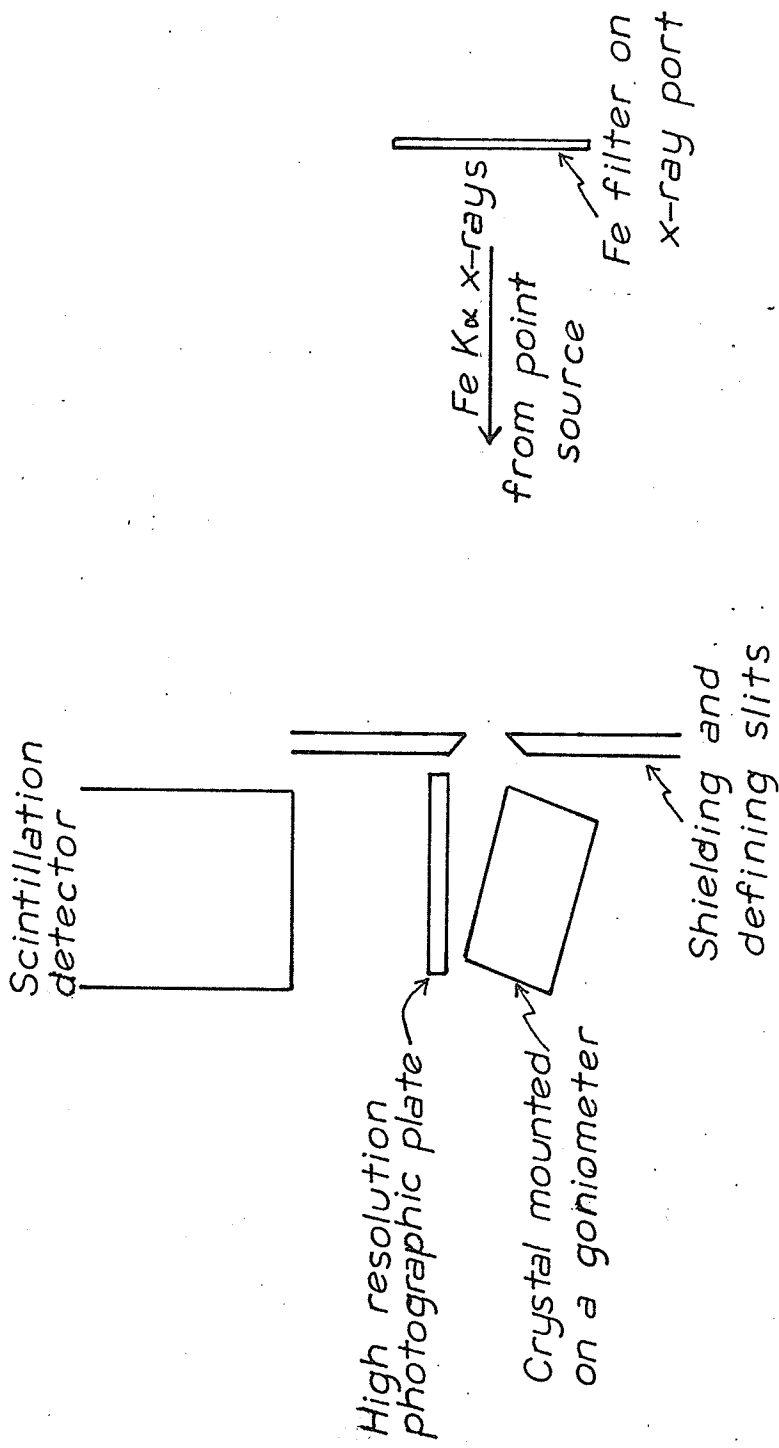
contained as many growth layers as possible and also the possible site of nucleation of the crystal. These surfaces were prepared and analysed for dopant density on the Philips Electron Microprobe Analyser at the AECL Research Station, Pinawa, Manitoba through the cooperation of Dr. A. Sawatzky. The density of the dopant at points on two mutually perpendicular scan paths was determined by measuring the intensity of the fluorescing characteristic radiation of the dopant. A given characteristic wave length for the dopant was found by first looking at a sample consisting of pure dopant material which also served as a standard. The dopant density was measured in steps of 20 to 40 μ along the scan paths. These paths could be identified optically on removal of the sample from the electron microprobe analyser.

4. X-ray Topographic and Optical Studies.

To ascertain if there were any dislocations or twins, an x-ray topography camera^{53,54} illustrated in Fig. 8 was constructed. A crystal surface was appropriately oriented in the camera so that maximum intensity of x-rays were incident on the surface when the camera was placed on an x-ray port of the Philips X-Ray Generator.⁵⁵ An Fe x-ray tube was used because of fluorescence problems with hematite.

Figure 8.

X-ray topography camera schematic.



The incident beam was also passed through an Fe filter to reduce as much fluorescence causing radiation as possible. By carefully adjusting the orientation of the crystal surface a suitable Bragg reflection was found with the scintillation detector and analyser attachment to the x-ray generator. The best Bragg reflection is that which balances intensity against smallest angle of incidence to, and closest to vertical reflection from, the crystal surface.

Once this has been achieved a preliminary topograph is taken with Kodak medical x-ray film which requires ~ 1 min exposure. If the topograph shows a good shadow of the crystal surface with no interfering Bragg reflections, an x-ray topograph is taken using Kodak High Resolution Plates. The plate is wrapped in aluminum foil to shield it from the light and placed as close as possible to crystal surface without interfering with the incident beam of x-rays. An exposure of 1 to 2 days is required and the plate is then developed in Kodak HRP developer and fixed. The plate can now be examined under the microscope to determine any variations in intensity which are produced by dislocations and crystal defects. The theoretical resolution of the camera is $\sim 5 \mu$ for a film to crystal surface distance of 2mm.

Virgin and annealed polished surfaces were examined

under the microscope for defects and characteristic properties of the physical appearance of the crystals.

E. Bulk Magnetization Properties.

1. Magnetometer Measurements.

Magnetic hysteresis loops for various unannealed and annealed bulk samples were measured using a P.A.R. Vibrating Sample Magnetometer⁵⁸. The magnetic field was provided by a Magnion 12" Electromagnet⁵⁹ with field dial which provided fields from 0 to 18 kOe. Unfortunately, this field could not be reversed uniformly through zero field. Therefore, in order to effectively reverse the field the crystal was rotated 180° in the magnetometer at zero field instead. In order to accommodate large bulk crystals an open ended sample tube was used. The signal measured by the magnetometer was only roughly adjusted to the saddle point since it was desired only to measure the moment relative to the saturation moment, and since the samples were large and irregular. For fields between zero Oe and the coercive field, after sample rotation, the magnetometer registered a negative reading. Unfortunately, the magnetometer had small electronic offsets which were different for different polarity. Therefore, instead of changing the polarity, the few measurements near zero negative field were taken

from the magnetometer null meter.

Anisotropy effects were measured by looking at the magnetization as a function of orientation in the basal plane and also by taking hysteresis loops at different crystal orientations in the basal plane.

The magnetization as a function of temperature for the Rh doped samples was measured. Cylindrical samples $1/8'' \times 1/8''$ were cut and mounted in the magnetometer and enclosed with the room temperature sample tube. A container small enough to go between the magnetometer pick-up coils was used to immerse the lower portion of the sample tube around the sample in acetone. The acetone was cooled to -40°C and allowed to drift back to room temperature. To obtain temperature between 10°C and 40°C the acetone was heated with a heat gun to give a slowly increasing temperature. Since the temperature drifts were ~ 0.2 to $1^{\circ}\text{C}/\text{min}$, the magnetization measurements could be taken versus sample temperature. The temperature was obtained from a copper-constantan thermocouple on the sample rod placed as close as possible to the sample. The magnetization as a function of temperature was measured at applied fields of 100 Oe and 15 kOe for the different dopings of Rh.

2. Mössbauer Spectrometer Measurements.

In order to determine the average magnetization direction in $\sim 125 \mu$ thick thin sections of crystal, the Mössbauer effect was used. An Elron Mössbauer Spectrometer⁶⁰ used in the parabolic mode in conjunction with a Nuclear Data 512 Channel Analyser⁶¹ was used to collect the Mössbauer spectra.

The domains were observed on a $(1\bar{1}0)$ thin section. It was then placed ~ 4 cm from the gamma ray source between the source and the proportional counter of the spectrometer so that the gamma rays were perpendicular to its surface. Mössbauer spectra for the whole slice and for three $\sim 1 \text{ mm}^2$ regions of the slice were taken and analysed by a computer program⁶² for six Lorentzian peaks on a parabolic background.

In order to determine if the antiferromagnetic axis was slightly inclined to the basal plane Mössbauer spectra for another $(1\bar{1}0)$ thin section were taken with the thin section in a 4 kOe magnetic field. The 4 kOe was to saturate the weak moment. The geometry of this experiment is illustrated in Fig. 9. A collimator was used to insure that the x-rays were perpendicular to the z axis. The magnetic field was along the y axis and the gamma ray

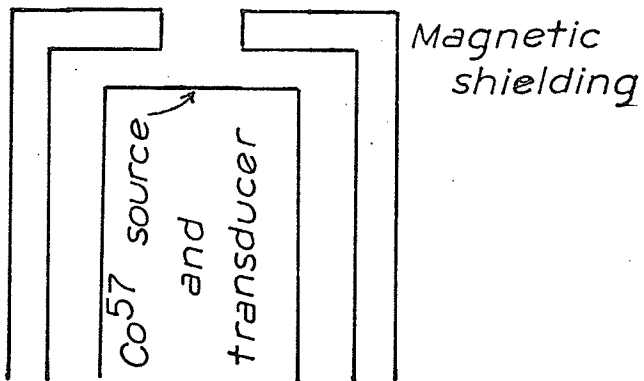
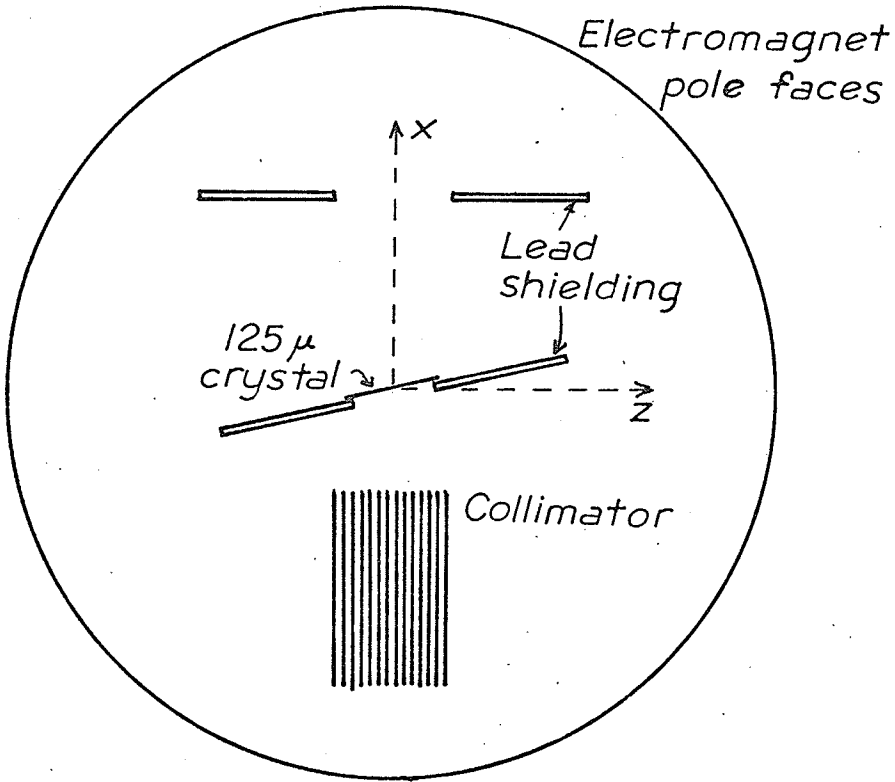
Figure 9.

Schematic showing geometry of Mössbauer experiment to determine direction of spin axis relative to (111) plane.

Proportional counter

50 cm

20 cm



source was placed to make the gamma rays as parallel to the x axis as possible. Spectra were taken and analysed for the slice parallel to the y axis and making angles 0° and $\pm 15^\circ$ with the z axis.

IV. Experimental Results.

A. Magnetite Colloid Domain Patterns.

1. At Room Temperature.

a) No Magnetic Field or Stress.

The form of the basic patterns observed for bulk and thin section, pure and doped crystals are illustrated in Figs. 10 and 11. With the exception of the example of Fig. 10(a), all patterns will be those observed after careful annealing. Fig. 10(a) and (b) illustrate domains before and after annealing on a mechanically polished (100) face. In this case the two photographs show essentially similar domain patterns. In the case of no annealing, the mechanical polishing has just made the pattern blotchy and disjointed. This, however, was not generally the case. For most crystals, the domain structure before annealing bore no resemblance to the final domain structure. In many instances, without annealing the crystal surface had none or only isolated patches of irregular domain patterns. It was only after annealing, and sometimes more than one annealing, that domain patterns similar to those of Fig. 10(b) would appear.

For pure crystals, most of them showed a domain pattern essentially similar to that of Fig. 10(b). The

Figure 10.

Domain patterns for various crystal surfaces illustrating essentially normal (N) domains only.

- (a) (100) unannealed surface of bulk crystal.
- (b) Same (100) surface as (a) but after 1000°C annealing.
- (c) $(11\bar{2})$ bulk crystal surface.
- (d) (110) bulk crystal surface.
- (e) $(11\bar{2})$ thin section surface.
- (f) (110) surface of 0.05 mole % Ti doped bulk crystal.

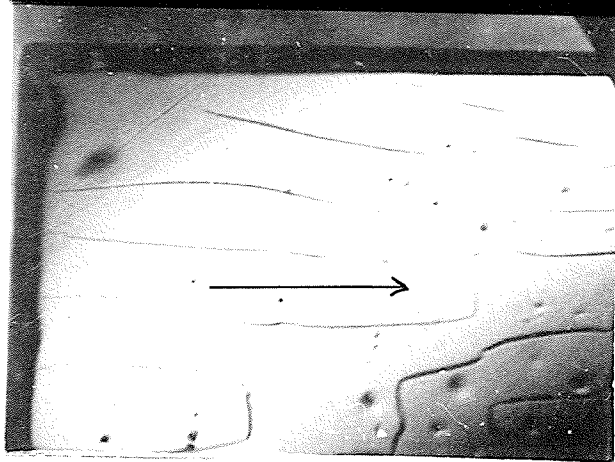


a)

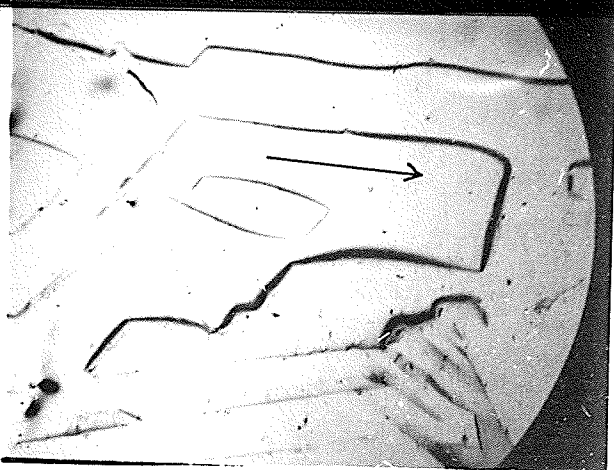
a

b

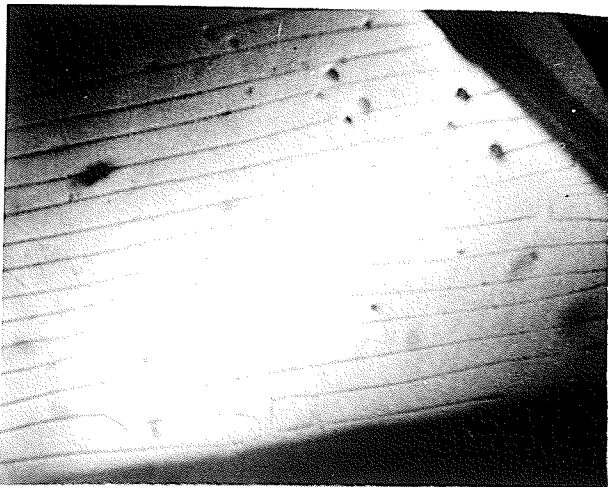
(b)



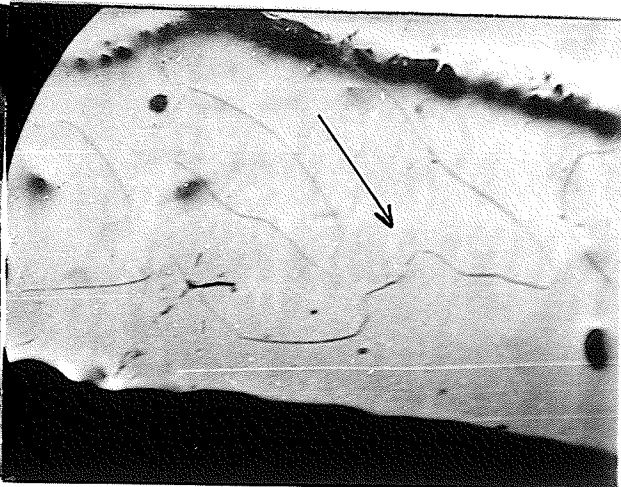
c)



(d)



e)



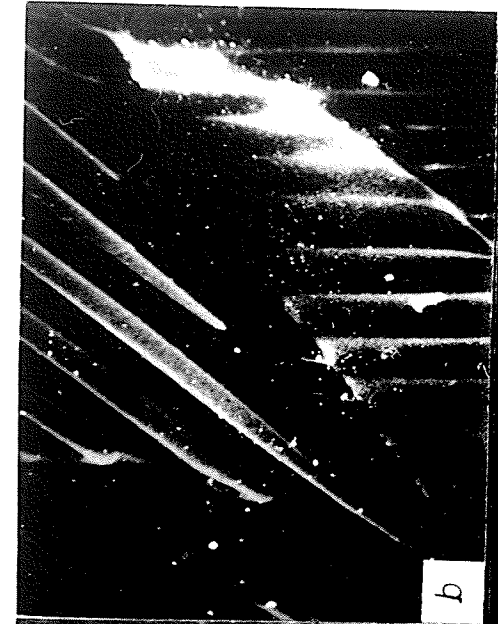
(f)

important feature to this domain structure is the majority of the domain walls, ignoring slight curvatures and small kinks, being parallel to the intersection of the (111) plane with the crystal surface. Any arrows on or adjacent to the photographs will indicate this direction. These walls are sometimes joined by shorter highly curved or roughly perpendicular walls resulting in nearly rectangular or maze like domain patterns. This type of structure which from now on will be called normal or N-walls is illustrated for different crystal surfaces in Fig. 10(c) and (d) and was observed on all bulk surfaces except for a few special cases and very poor quality, generally doped, crystals. No domain patterns are ever observed on (111) planes.

The special cases observed on three surfaces, are those illustrated in Fig. 11(a) and (b). In these cases a sub-structure domain pattern appears to be superimposed on the normal domain pattern over nearly all the crystal surface. This sub-structure consists of very straight parallel walls in two directions and with $\sim 50\mu$ separation. The colloid tends to be more lightly and diffusely deposited at these walls. The two directions of these walls are symmetric with the intersection of the (111) plane with the surface. They have only been observed

Figure 11.

Characteristic (C) and characteristic -normal (CN) domain structures. The C-domain structures for pure and 0.5 mole % Ti doped hematite on bulk (110) surface are illustrated in (a) and (b) respectively. In (c) a thin section covered almost entirely with CN-domains but having a very wide N-domain pattern superimposed, is shown. The change of N-domains to CN-domains is shown in (d). In both (c) and (d) the N-domain walls are horizontal.



b



a



(d)



(c)

normally on virgin (110) surfaces. The angle between the two sets of walls is $\sim 47^\circ$ in the case of pure crystals and $\sim 39^\circ$ in the case of the one 0.05 mole % Ti doped crystal. This type of domain structure will be called characteristic or C-walls.

Occasionally on (110) surfaces, which basically had a normal structure, traces or suggestions of C-walls appeared in small regions of the surface. This is the case in Fig. 10(d) in the bottom portion of the photograph.

In many of the doped crystals, especially those of high doping, and occasionally a pure crystal, regular domain structures did not appear after several anneals. In fact, sometimes most of the surface would be devoid of domain patterns and in the regions with domains the patterns would be faint and irregular or very curvy. However, whenever domains appeared they always indicated a parallelism to the intersection of the surface and the (111) plane. An example of very curvy domain patterns is given in Fig. 10(f). The parallelism is still apparent.

Thin sections of crystal resulted in extremely regular domain patterns being observed. The $(11\bar{2})$ section, illustrated in Fig. 10(e), shows a very good approximation to a stripe domain structure. The domains on both sides of this $(11\bar{2})$ thin section were observed.

They both had essentially the same domain structure and showed deviations from the stripe domain structure in the same places. Other $(11\bar{2})$ sections showed similar structure but generally also showed small regions with less regularly spaced domains.

For $(1\bar{1}0)$ thin sections the domain structures were a little more complex. No specimen was found with a perfect stripe domain pattern. Generally, large portions 25% to 50%, of the surface would consist of a normal stripe pattern. This stripe pattern's walls would suddenly change direction, now making an angle of $26^\circ \pm 2^\circ$ to the intersection of the (111) and $(1\bar{1}0)$ planes. These walls which will be called characteristic-normal or CN-walls, would then gradually disappear resulting in regions of no domains. An example of a transition between these two types of stripe domains is illustrated in Fig. 11(c). The normal walls occasionally disappeared without characteristic normal walls.

One $(1\bar{1}0)$ slice, except for $\sim 5\%$ of surface with normal walls, was covered entirely with CN-walls with very widely spaced and faint N-wall pattern superimposed. This is illustrated in Fig. 11(d). The N-walls are parallel to long edges of photographs. The different widths of each type of domain structures are listed in

Table III.

b) With Applied Magnetic Field.

Under the application of a field, as long as there was a component in the (111) plane, N-domains in bulk specimens would coalesce by adjacent domains growing larger and smaller respectively until they generally disappeared between 25 to 50 Oe. For good N-domain structures the shrinking domains would either gradually decrease in size until they coalesced or disperse just before they reached the point of coalescing. No adjacent domains would both increase or both decrease in size. In poorer normal domain structures, which were more irregular or curvy, some portions of domain walls would move very little or not at all and the others after moving to decrease or increase a domain size would stop after some field between 0 and 50 Oe is reached. These walls would generally eventually be removed by suddenly dispersing in fields between 25 and 100 Oe. The typical magnetic field behaviour of N-domains is best illustrated in Fig. 12 by $(11\bar{2})$ thin section. For the field perpendicular to the crystal surface the domains all disappear in a perfectly uniform manner as indicated by Fig. 12(a) and (b). They were removed at 20 Oe and reappeared at 7 Oe.

Table III. Width of Domains.

Specimen Type	Dimensions mm	Wall Type	Domain Width Variation μ	Average Width μ
Bulk (100)	15x15x6	N	200 - 500	380
Bulk (11 $\bar{2}$)	5x4x3	N	250 - 600	360
Bulk (110)	5x5x5	N	250 - 600	370
Bulk (110)	5x5x5	C	40 - 80	50
(11 $\bar{2}$) section	0.200	N	50 - 200	138 $\pm 10\%$
(1 $\bar{1}$ 0) section	0.200	N	50 - 200	110 $\pm 10\%$
(1 $\bar{1}$ 0) section	0.210	N	50 - 200	117 $\pm 10\%$
(1 $\bar{1}$ 0) section	0.225	N	50 - 200	137 $\pm 10\%$
(1 $\bar{1}$ 0) section	0.075	N	50 - 200	142 $\pm 10\%$
(1 $\bar{1}$ 0) section	0.050	N	50 - 200	123 $\pm 10\%$
(1 $\bar{1}$ 0) section	0.062	N	50 - 200	123 $\pm 10\%$
(1 $\bar{1}$ 0) section	0.087	N	50 - 200	90 $\pm 10\%$
(1 $\bar{1}$ 0) section	0.087	N	50 - 200	100 $\pm 10\%$
(1 $\bar{1}$ 0) section	0.300	CN	100 - 300	240 $\pm 10\%$

Figure 12.

Effect of fields in the (111) plane on N-domains on (11 $\bar{2}$) thin section. The field is perpendicular to crystal surface in (a) and (b). A field parallel to surface and along domain walls is applied in other photographs. The magnitude of the field is (a) 7 Oe, (b) 15 Oe, (c) 0 Oe, (d) 7 Oe, (e) 15 Oe and (f) 20 Oe.



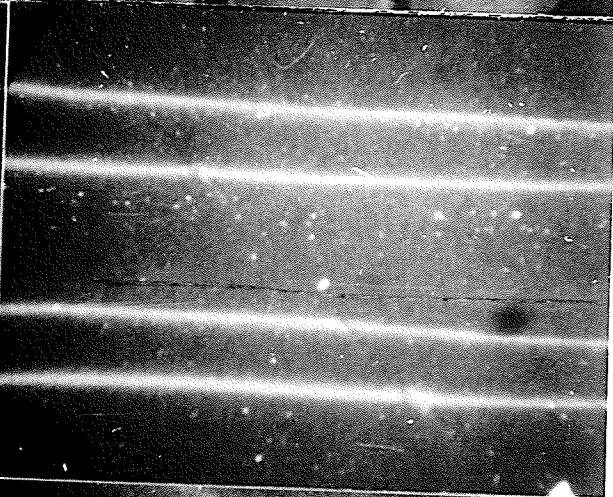
(a)

(b)

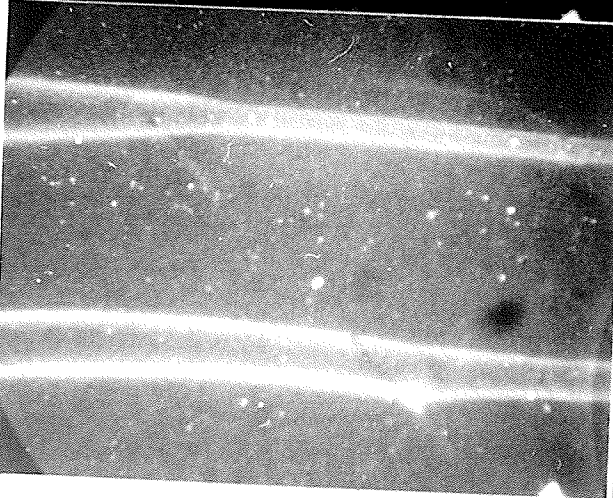
(b)



(c)



(d)



(e)

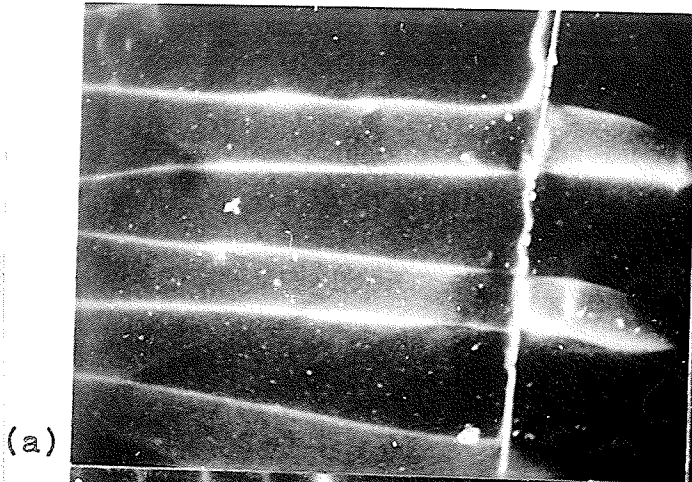


(f)

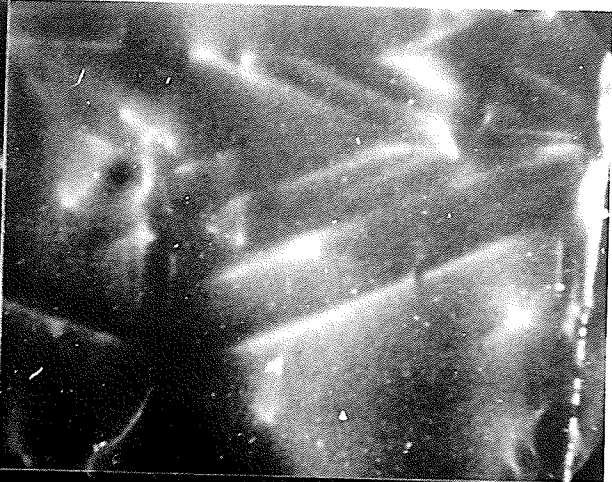
In the case of the field parallel to the crystal surface the behaviour was similar except for some rather interesting and anomolous behaviour in one small region. A first indication of this is the not complete disappearance of the domains in Fig. 12(f) at the one edge of the photograph. In the region just adjacent, the domain structure is illustrated in Fig. 13(a). In this region there appears to be some defect as indicated by a bright vertical dashed line. There was a domain wall along this defect so that the domains directly opposite each other across the defect increased and decreased in size respectively. The domains eventually coalesced into the defect at ~ 40 Oe. After removal of the normal domains, colloid distributions as illustrated in Fig. 13(b) appeared. These distributions took the form of diffuse lines parallel to two directions symmetric with the (111) plane. These diffuse lines disappeared at 100 Oe but reappeared on reducing the field. There also appeared now, however, diffuse lines perpendicular to the (111) plane. At 17 Oe the normal domains reappeared but not around the defect region where irregularly spaced walls vertical to the (111) plane appeared. These walls were evenly spaced at 10 Oe and were about twice the width of normal domains. On removal of all fields new vertical walls appeared in between

Figure 13.

Unusual effects of defect on behaviour of domains in magnetic fields for same sample as Fig. 12. Domains around defect (bright vertical line) with field of 20 Oe parallel to surface and domains are shown in (a). In (b) the same region as (a) is shown after increasing field to 50 Oe. Vertical domains appear after removal of field about defect region which disappear further away from defect as shown in (c) and (d). In (e) domains with no field, after vertical domains have been essentially removed by a reverse field of 50 Oe, are shown. The behaviour of vertical domains in field of 7 Oe parallel to (110) plane and surface is illustrated in (f).



(a)



(b)



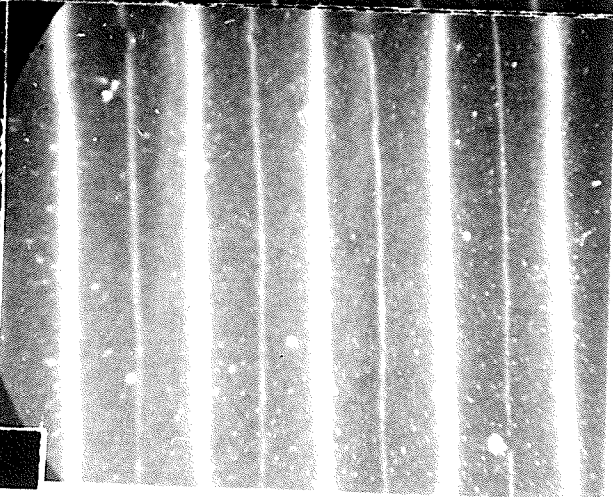
(c)



(d)



(e)



(f)

every old vertical wall. This pattern is now illustrated in Fig. 13(c). The vertical domains are slightly narrower than normal domains. These vertical domains disappeared slowly as they got further up from the defect region as shown in Fig. 13(d). On application of a field, again parallel to crystal surface, everything behaved normally except the vertical walls. They did not move. Instead one set of alternate walls slowly disappeared depending on field direction as illustrated in Fig. 13(f), and were gone at about 25 Oe. The remaining vertical walls showed sideway movements with increasing field and all of them had dispersed by 100 Oe.

These vertical walls could be completely removed by applying a field perpendicular to the crystal surface which removed all the domains. The vertical walls then did not reappear on removal of the field. They could also essentially be removed, as indicated in Fig. 13(e), by applying a field of 50 Oe parallel to the surface in the reverse direction and removing it. If this value is exceeded the vertical walls return, and if a lower field is used a lesser amount of the vertical walls are removed.

A distinctive behaviour of the colloidal walls in magnetic fields is the gradual disappearance of every second wall with increasing field if there is a component of field perpendicular to the wall and parallel to the crystal surface. The remaining walls become heavier.

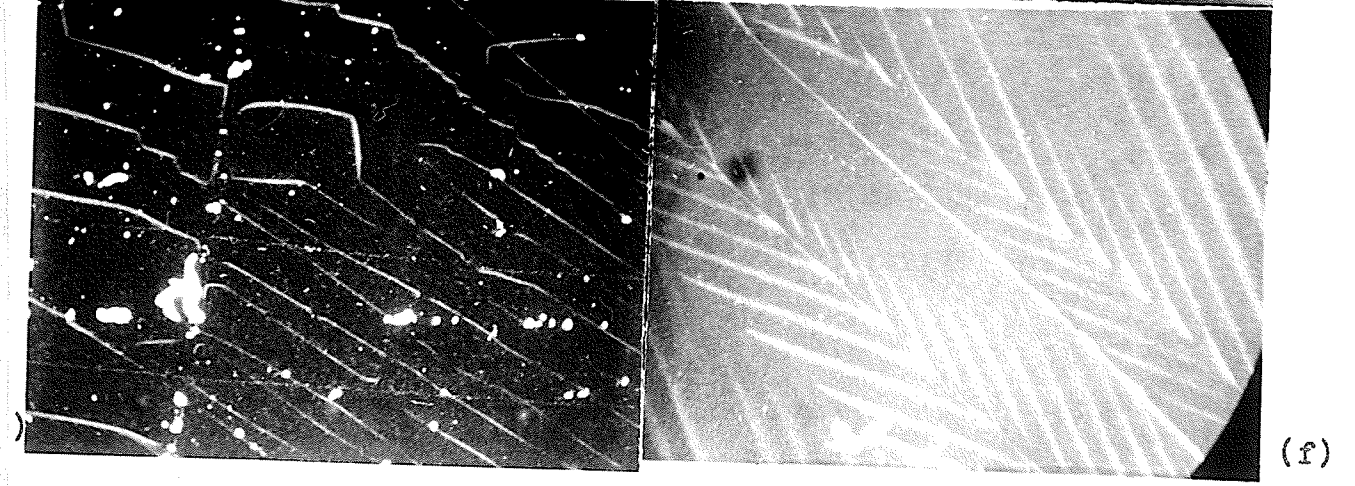
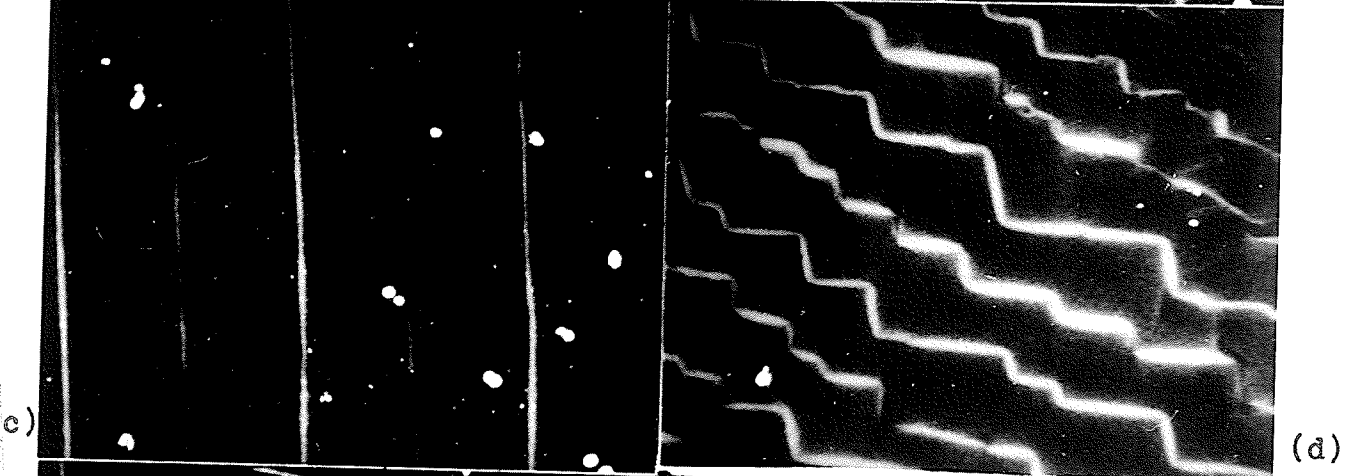
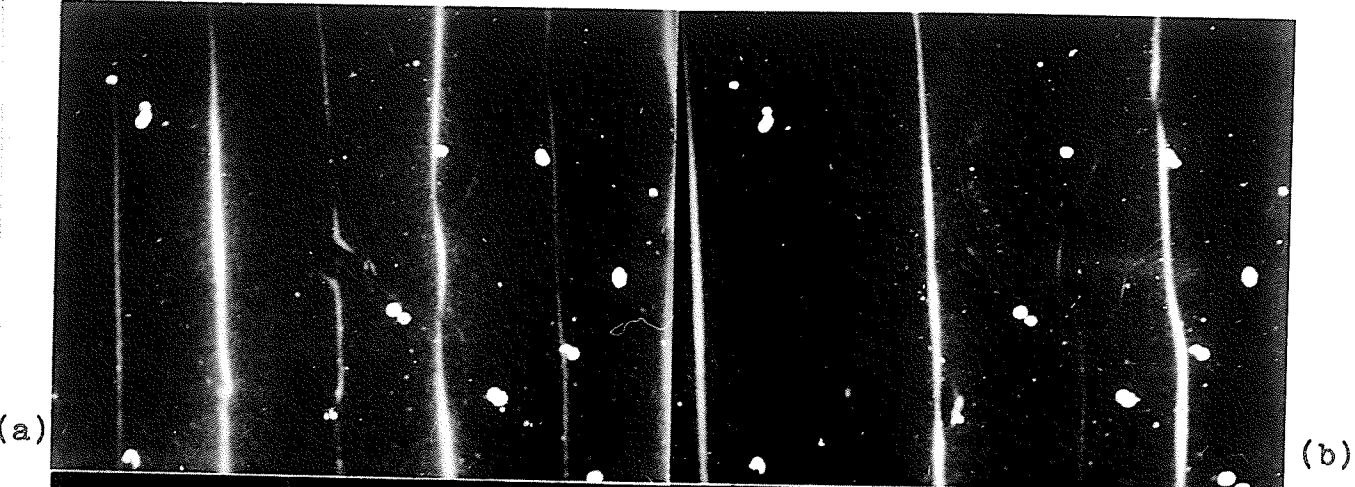
This effect is illustrated in Fig. 13 (f) and also in Fig. 14(a) and (b).

In $(1\bar{1}0)$ sections, the normal walls behave as those in the $(11\bar{2})$ section for fields perpendicular to the crystal surface, coalescing in fields of between 20 and 30 Oe. For fields parallel to the surface however, they would move only slightly, $\sim 10-20\mu$, with increasing field and they would either disperse or gradually convert into the CN-walls with no N-walls by 20 Oe. The CN-walls would show only very slight movements, which did not indicate movements toward or away from each other, with increasing field. Generally, the movements appear as sideways shifts of the whole domain structure. Also, the distance between the walls could not be determined to easily since alternate walls had disappeared by 10 Oe. The remaining walls however, were still present at 100 Oe. The movements however, did not really suggest that these walls were coalescing with field. In a field perpendicular to the surface the CN-walls would show small movements of $10-20\mu$ toward and away from each other respectively before dispersing in fields of a few oersteds.

An unusual behaviour of these walls in a field parallel to them and the crystal surface occurs when the field is reversed. At approximately 4-5 Oe in the reverse

Figure 14.

The unusual behaviour of CN-domains in fields and some unusual domain structures. A field is applied parallel to basal plane and $(1\bar{1}0)$ thin section crystal surface. A field of 5 and 10 Oe is applied in (a) and (b) respectively and is reversed to -10 Oe in (c). Reversal of the field caused dispersal of domains and reappearance in new positions. When N- and CN-domains appear in adjacent regions, then removal by a field results in the type of pattern in (d) reforming in N-domain region. The enhancement of CN-domains adjacent to N-domains after stress and cycling through T_M is illustrated in (e). Photograph (f) shows production of CN-domains on (110) bulk surface after application of stress. They are superimposed on very straight N-domain walls.



field all the CN-domain walls disperse suddenly and reform at slightly different positions with the opposite set of walls now being the fainter set of walls due to colloid polarization. This effect would occur for any field as long as there is a component in the basal plane parallel to the crystal surface. This effect is illustrated in the sequence of photographs of Fig. 14(a), (b) and (c).

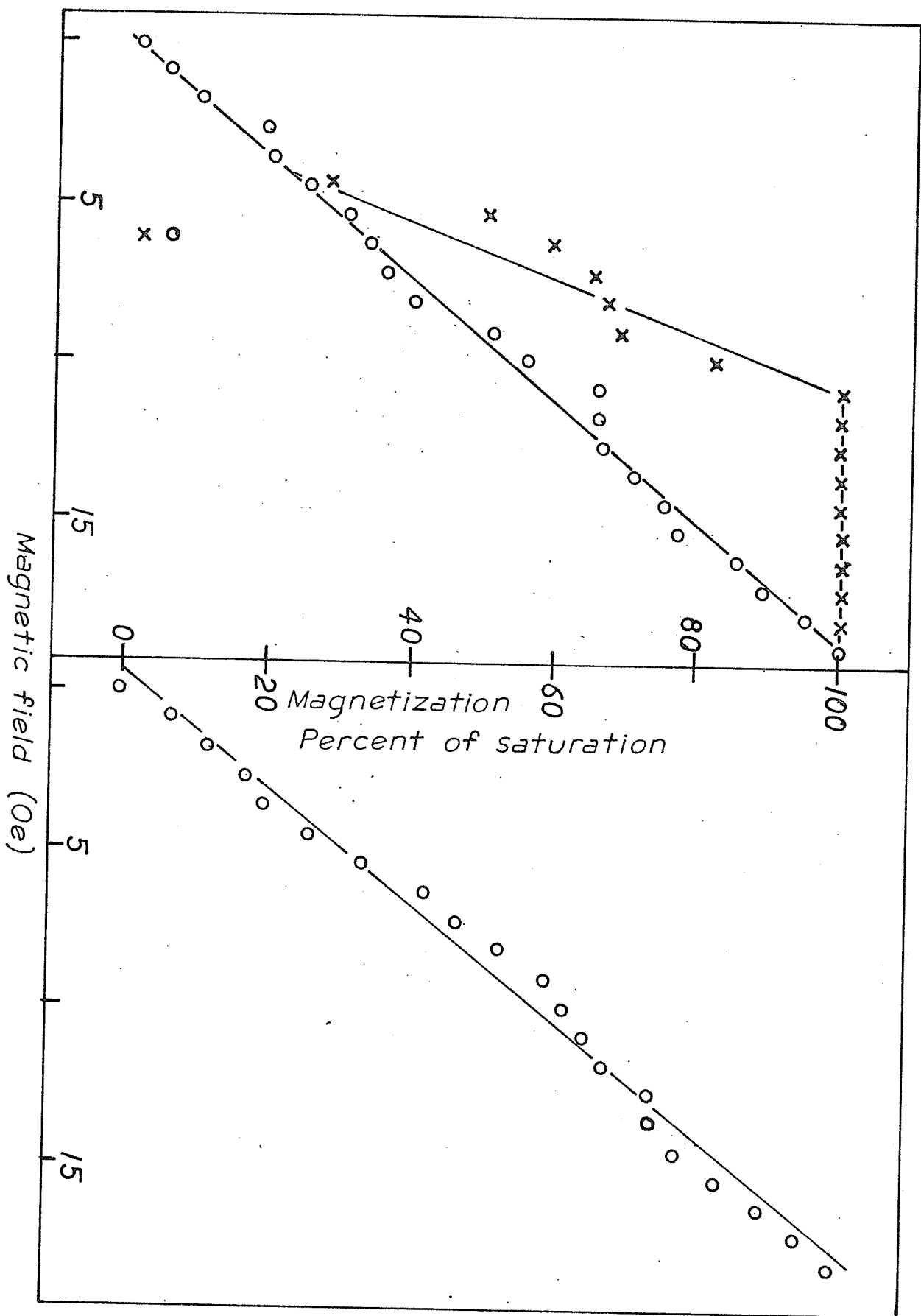
In regions of $(1\bar{1}0)$ thin sections having N-domains and CN-domains adjacent, application of a sufficient magnetic field parallel to crystal surface results in the types of structure illustrated in Fig. 13(d) on removal of the field. These walls behave exactly like normal walls.

C-domains showed no change in size in fields regardless of field direction, gradually or suddenly disappearing with increasing fields. Only one phase would remain in higher fields. Any movement of the walls appeared as equal sideways displacements of all walls and occasionally there was a switching from one direction to the other.

Fig. 15 illustrates a graph of magnetization versus field for $(1\bar{1}0)$ and $(1\bar{1}\bar{2})$ thin sections interpreted from measurements of the widths of ten stripe domains in each

Figure 15.

Graphs of magnetization according to domain widths
versus magnetic field perpendicular to crystal surface
for $(1\bar{1}0)$ and $(11\bar{2})$ thin sections.



specimen as a function of field perpendicular to crystal surface. The magnetization \underline{m} is given by

$$\underline{m} = \underline{m}_S (\sum w_I - \sum w_D) / (\sum w_I + \sum w_D)$$

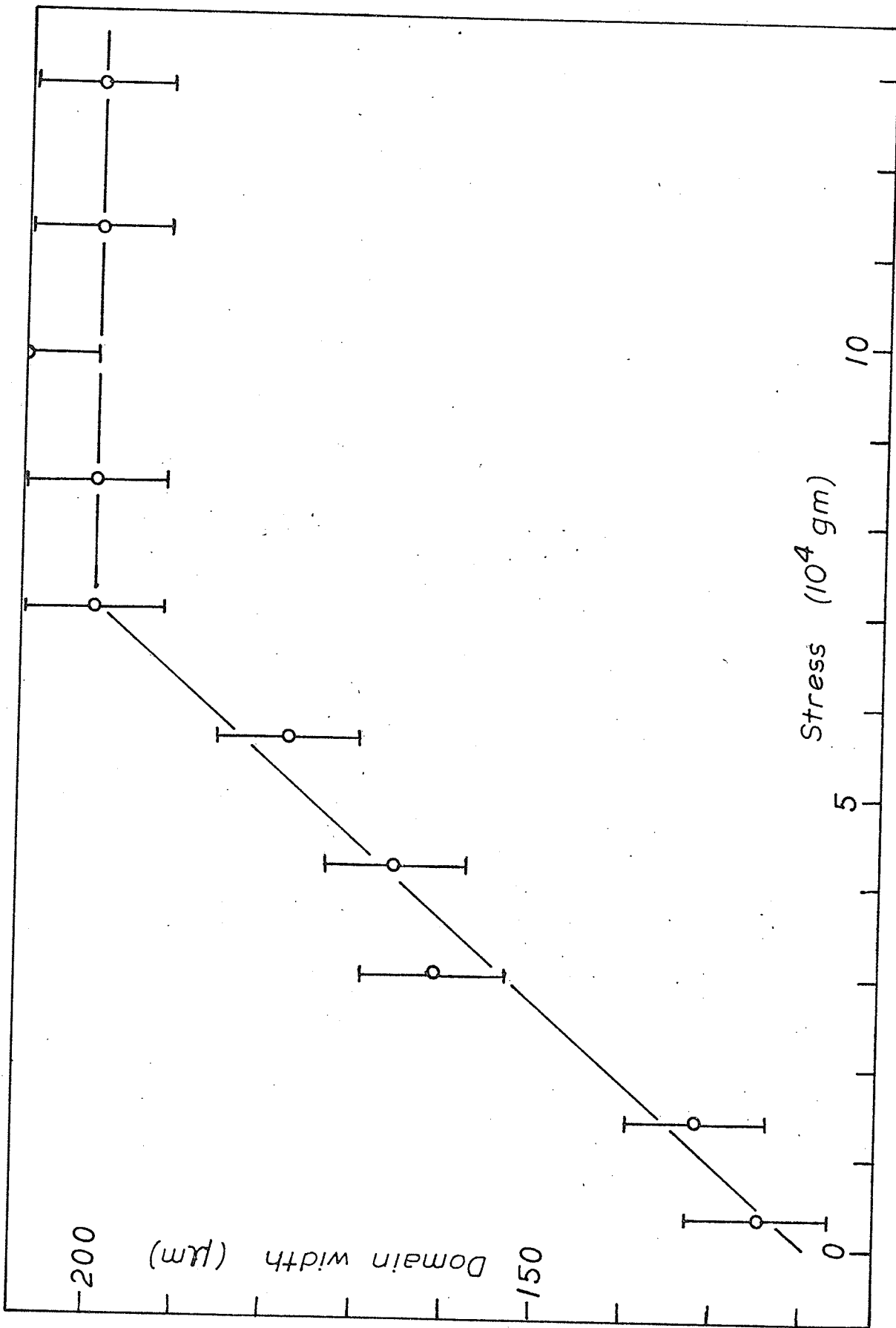
where \underline{m}_S is the saturation magnetization and w_I and w_S are the widths of the increasing and decreasing domains respectively.

c) With Applied Stresses and Magnetic Fields.

Most results from applied stress resulted in unclear, unmeaningful results. However, a few results did appear significant. For bulk specimens in most cases a uniform linear compression stress parallel to crystal surface would enlarge the domain structure anywhere up to 50%. As the stress increased the walls would move for a while until no further movement occurred for any further stress. Under the application of magnetic field parallel to crystal surface, with crystal under maximum stress, the domain walls did not move or at most only very slightly in a few places. They remained there up to 100 Oe. However, they did move, and finally coalesce, in nearly all cases, with a perpendicular field. Thin sections behaved in exactly the same manner. Figure 16 illustrates, the change in domain width of stripe patterns as a function of applied uniform compression stress.

Figure 16.

Graph of N-domain width for $(1\bar{1}0)$ thin section as a function of applied stress.



The application of shear stresses did not lead to any meaningful results possibly because it is impossible to apply just a shear stress. The mechanical means used also applied some kind of compressive stress to the crystal as well. In thin sections, various results occurred such as irregular domain patterns. Some regions in the centre of the crystal slice were without domains, while the edge areas had N-domain structure. Sometimes a uniform stripe normal domain structure or no domain structure at all would occur. However, whatever domain pattern occurred under shear stress, it behaved in magnetic fields in a similar manner to domain structures produced by a uniform compression stress.

For thin sections, no matter what kind of stress was applied, any domain structures other than normal type were quickly removed by stresses less than $\sim 3000 \text{ gms/cm}^2$. In all instances, except one, where stress was applied to bulk crystals the behaviour of the domains appeared similar to the case of thin sections. The exception was a pure bulk crystal where the stress was applied parallel to the (110) surface and perpendicular to the sides which were close to being (110) planes. Initially the crystal exhibited N-domains with a few regions of C-domains. Application of compression stress increased the number of

C-domains, and made the normal domains all very straight and perfectly parallel to intersection of the (111) plane with crystal surface as illustrated in Fig. 14(f). On increasing the stress beyond 50 kgms/cm^2 , however, all the C-domains were removed, but they returned on lowering the stress and remained under no stress.

In thin-section crystals which without stress exhibited some other domain structure than just N-domains. Application and removal of stresses followed by cycling through T_M sometimes enhanced the non-normal type domain structure as illustrated in Fig. 14(e).

2. Colloidal Structures at The Morin Transition.

The behaviour of the colloidal domain pattern as crystals cooled or warmed through the Morin transition are illustrated in Figs. 17-19. In Fig. 17, the effect is shown for a (110) face of a pure crystal as it is cooled. At regions A and B in Fig. 17(a) the two colloidal lines indicate small domain movements because of their very broad or double-wall appearance. This effect is caused by colloid coagulating at old domain boundaries. Therefore, care must be taken in distinguishing the active domain boundary. While viewing in the

Figure 17.

Domain pattern for a (110) surface of pure hematite on cooling through the Morin transition. The white band in upper left hand corner is crystal edge formed by two (110) surfaces. The temperature of the crystal in each photograph is (a) -10.0°C , (b) -10.2°C , (c) -10.4°C , (d) -10.5°C , (e) -10.6°C , and (f) -10.8°C .

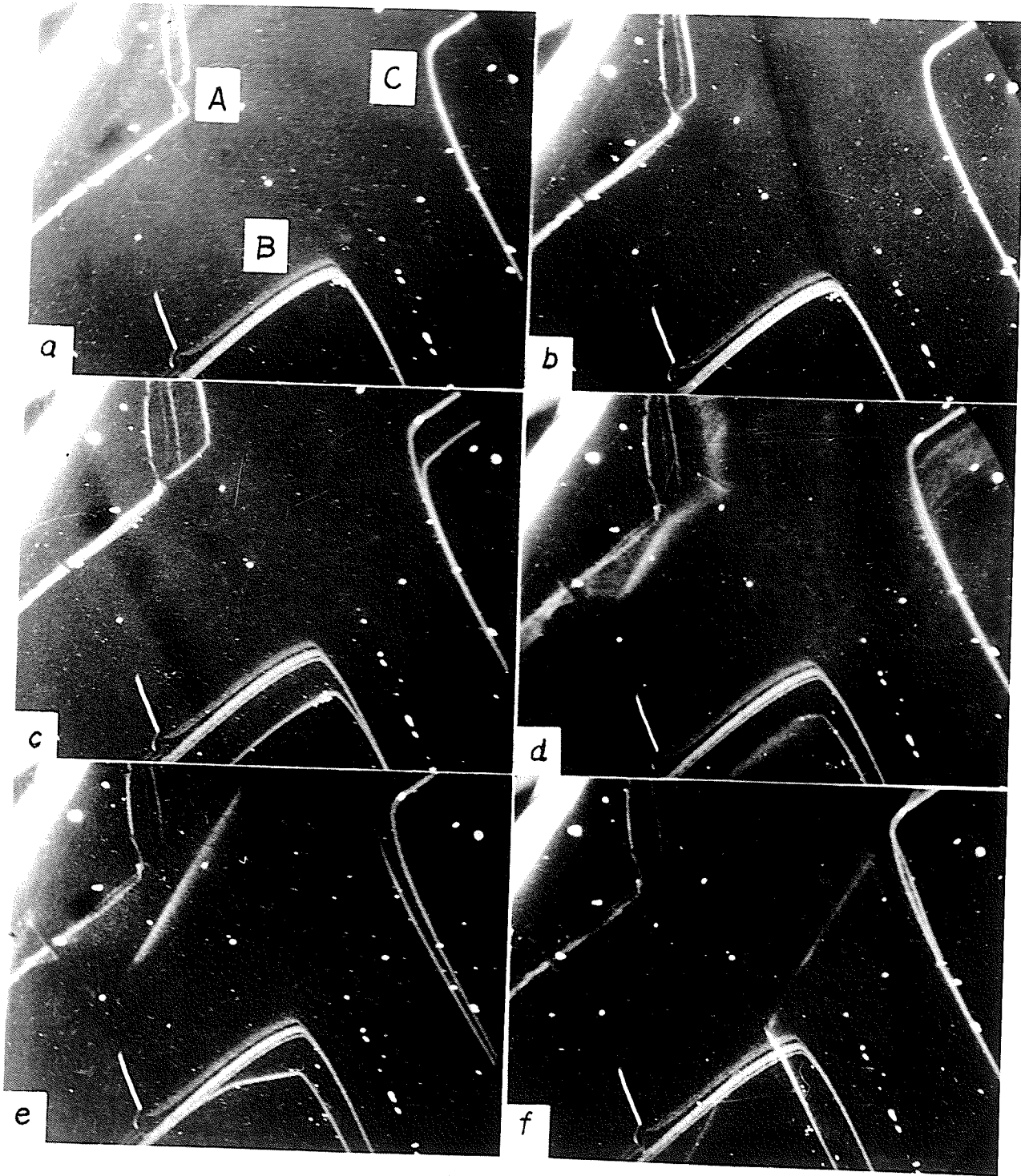


Figure 18.

- (a) Same surface as in Fig. 17, but showing domain pattern after cycling through T_M many times.
- (b) Domain pattern at Morin transition in pure $(11\bar{2})$ thin section.
- (c) Affect on transition of high intensity incident microscope light for thin section of (b).
- (d) (e) and (f). The Morin transition in a 2 mole % Ga doped thin section at -18°C , -19°C and -26°C respectively.

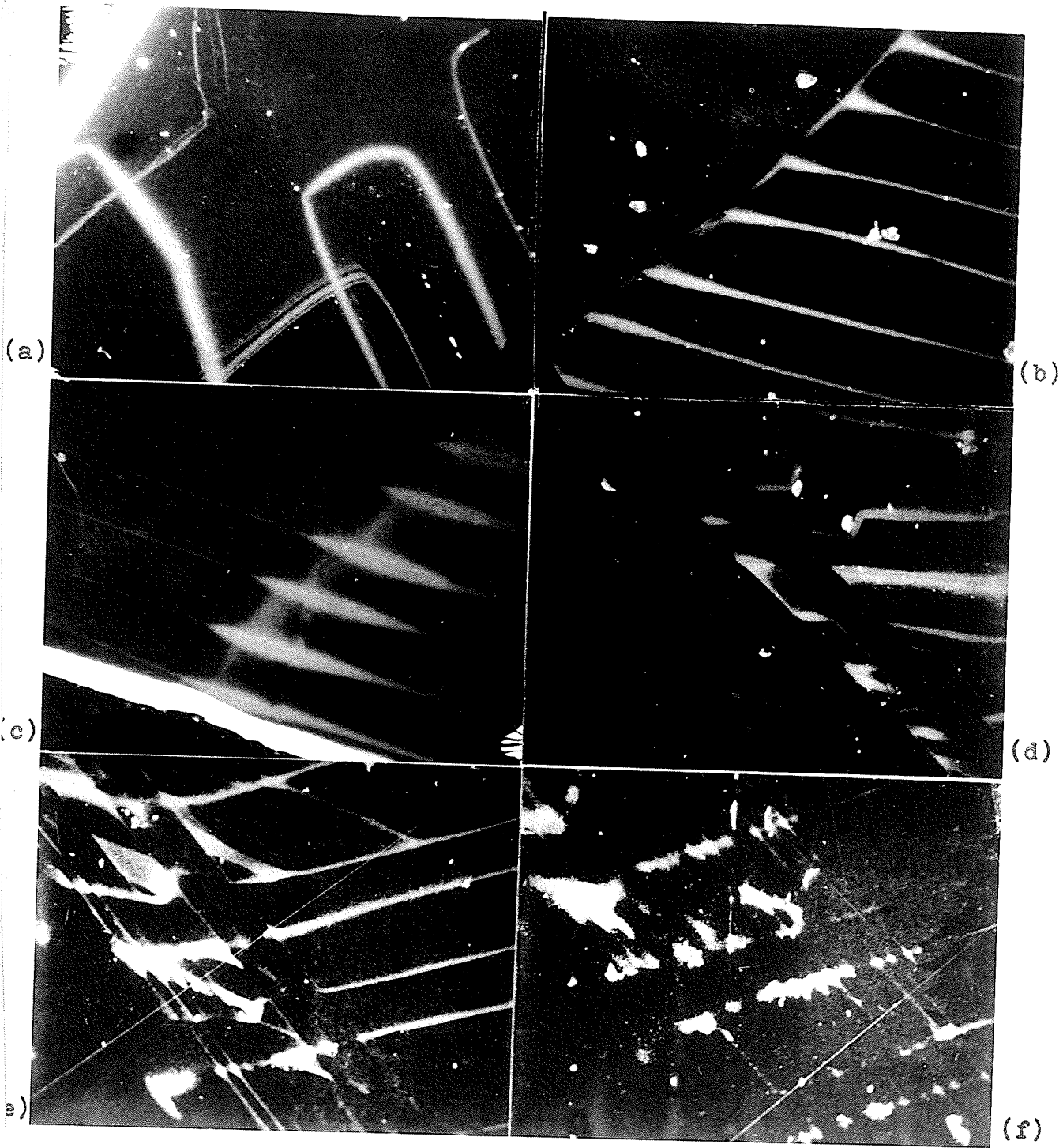
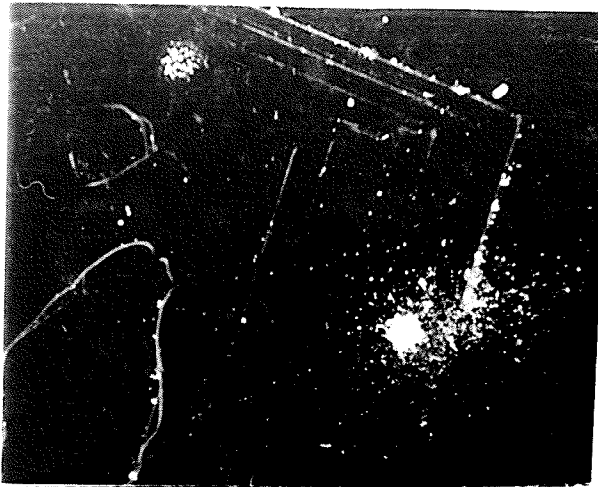


Figure 19.

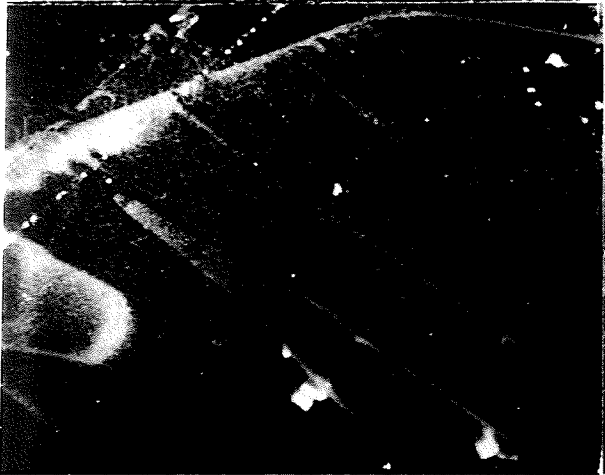
- (a) The Morin transition for (110) surface of a 0.05 mole % Ti doped bulk crystal at -15°C .
- (b) to (f) The Morin transition for a (110) thin section of a 0.1 mole % Ti doped crystal about -25°C .



(a)



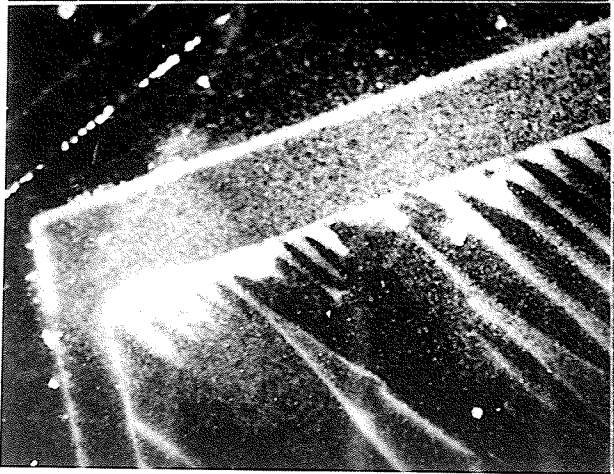
(b)



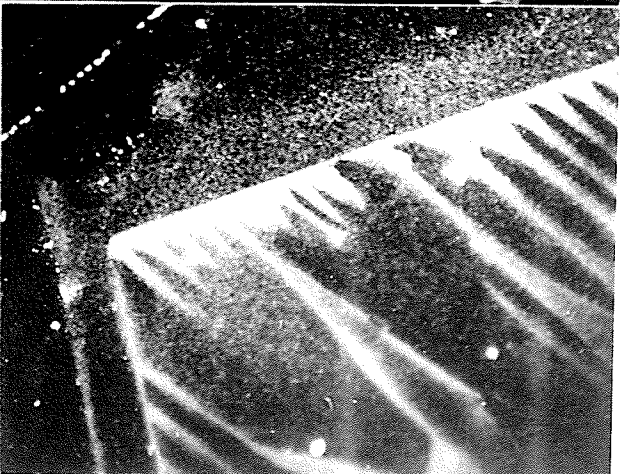
(c)



(d)



(e)



(f)

microscope the difference is obvious because of Brownian motion of the particles, but unfortunately this is not observable in photographs. Therefore, the change in pattern between succeeding photographs must be used to distinguish the difference. This coagulation problem occurred in this case because of old colloid, but in most cases coagulation was not a problem.

Figure 17(b) indicates further domain wall movement in region A. In Fig. 17(c) regions A, B and C have all experienced domain-wall movement. An important and interesting phenomena is the formation of a light diffuse line of colloid in region A in Fig. 17(e) which was in the process of forming in Fig. 17(d). This line which effectively runs across the whole crystal surface, is parallel to the intersection of another (110) plane with this surface. In Fig. 17(f) the wall has moved further inwards to regions B and C and the domain walls end on this diffuse wall as if it were the boundary of the crystal. There is no evidence of domain walls between the line and the edge of the crystal. The edge is indicated by the bright band in upper left-hand corners of the photographs. Any walls that appear are coagulated colloid. Eventually all the domain walls are removed in the path of the light diffuse wall as the temperature decreases. This

line and domain walls move in both an apparent continuous and discontinuous fashion. The term 'discontinuous' is to mean that the colloid in the wall relaxes and disperses and reforms at a new site. On the other hand, 'continuous' is to mean movements of the wall which are small or slow enough to allow the colloid to retain its shape.

This transformation process reverses its path in an exactly similar manner on warming back through the Morin transition. In fact in all cases studied, this was found to be the case. However, all photographs were taken for the cooling process only. The reason for this is a resolution problem because of the time required for sufficient colloid to deposit out at new domain boundaries. This is not a problem on cooling since colloid has been allowed to deposit out at the boundaries. In changes in the domain structure, there is always then a high density of colloid at adjacent boundaries to immediately supply the new boundary with enough colloid to become visible on photographs. In the warming process, of course, no domains are present initially and also there is always change going on. This results in much lower particle densities at the boundaries so that they are not resolvable on photographs, but can, with care, be seen while viewing on the microscope.

The behaviour observed at the Morin transition for this pure crystal was essentially typical of nearly all crystal surfaces studied. The exceptions to this behaviour were a few pure and a 0.05 mole % Ti doped crystals. In these cases on the (110) surface studied the transition occurred suddenly with all the domain walls on the surface suddenly dispersing. However, on non (110) faces these two crystals behaved in the normal manner.

This separation into two phases, with and without domain walls, are apparently the weakly ferromagnetic (WF) and antiferromagnetic (AF) states of hematite respectively. In most cases it was not done by just one light diffuse colloid boundary. Instead, as many as two or three intersecting light diffuse lines, all parallel to the intersection of (110) planes with the surface, formed the boundary between the two phases. This is clearly illustrated in Figs. 20, 21 and 22 where the boundaries between the two phases for different temperatures are drawn on an outline of the crystal surfaces. The dopant density for these surfaces was determined by electron microprobe analysis along the scan paths indicated. These boundaries were found to be the same before and after annealing the crystals.

Figure 20.

The WF-AF phase boundaries obtained from domain observations on a 0.5 mole % Rh doped bulk crystal at various temperatures. They are drawn on the outline of the crystal surface and the scan paths of the electron microscope analysis are also shown.

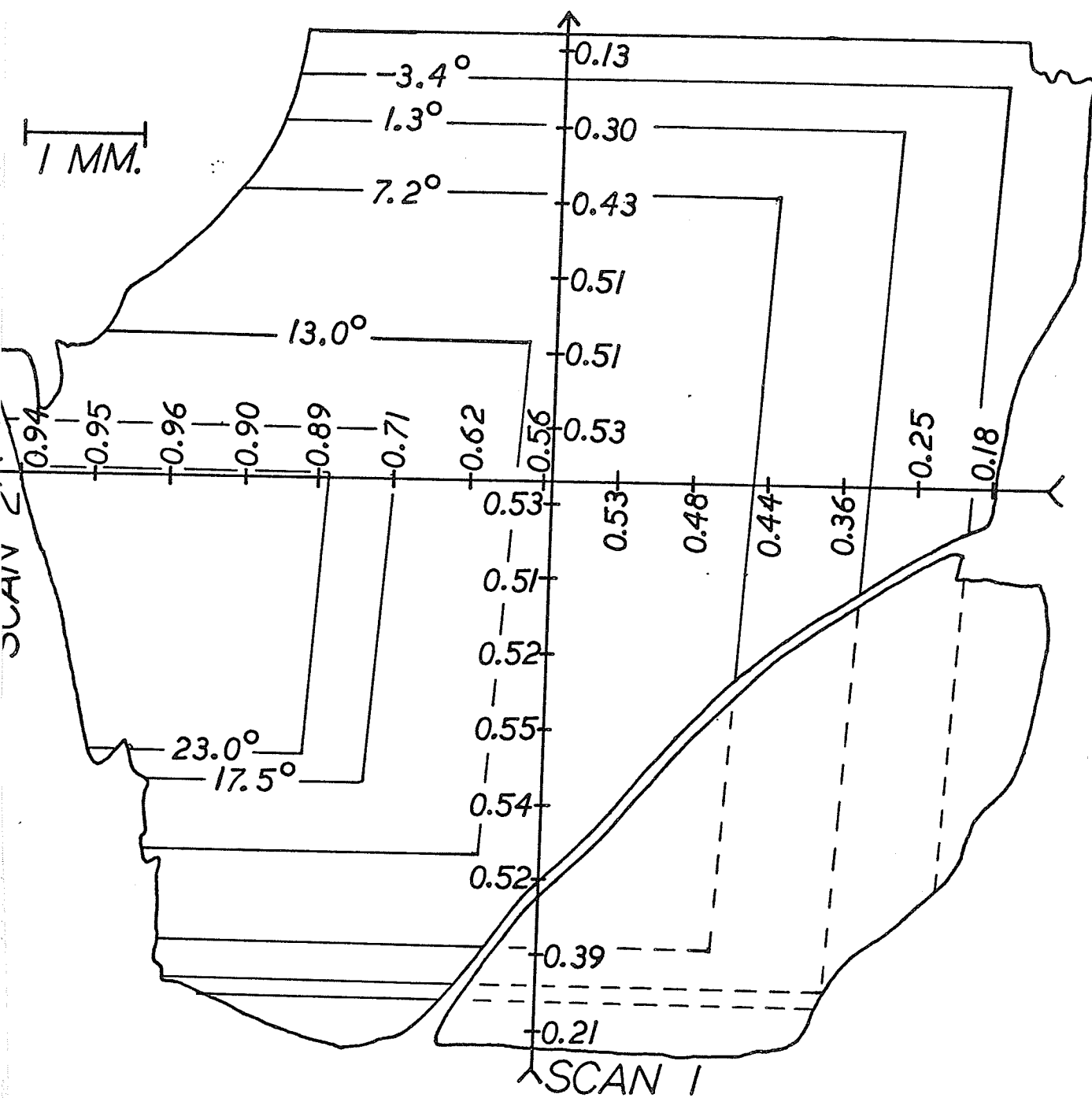


Figure 21.

The WF-AF phase boundaries on a 1.0 mole % Rh doped crystal.

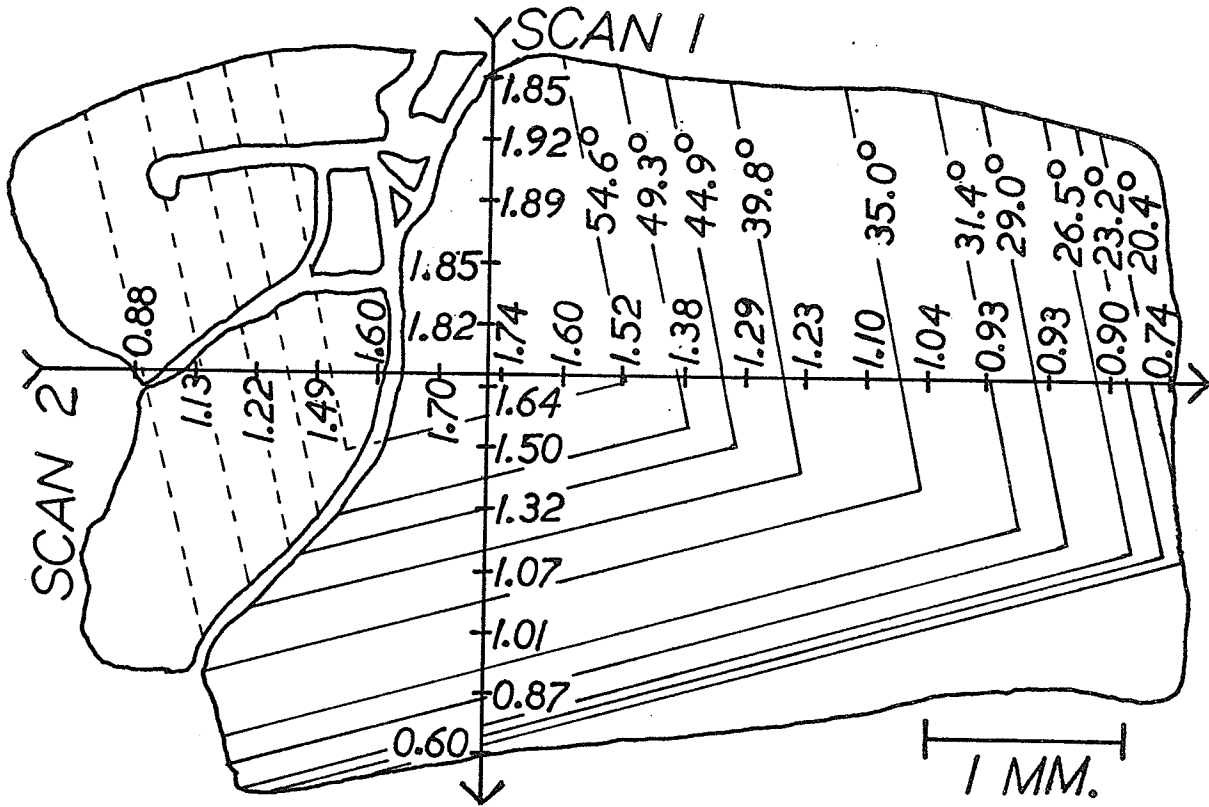
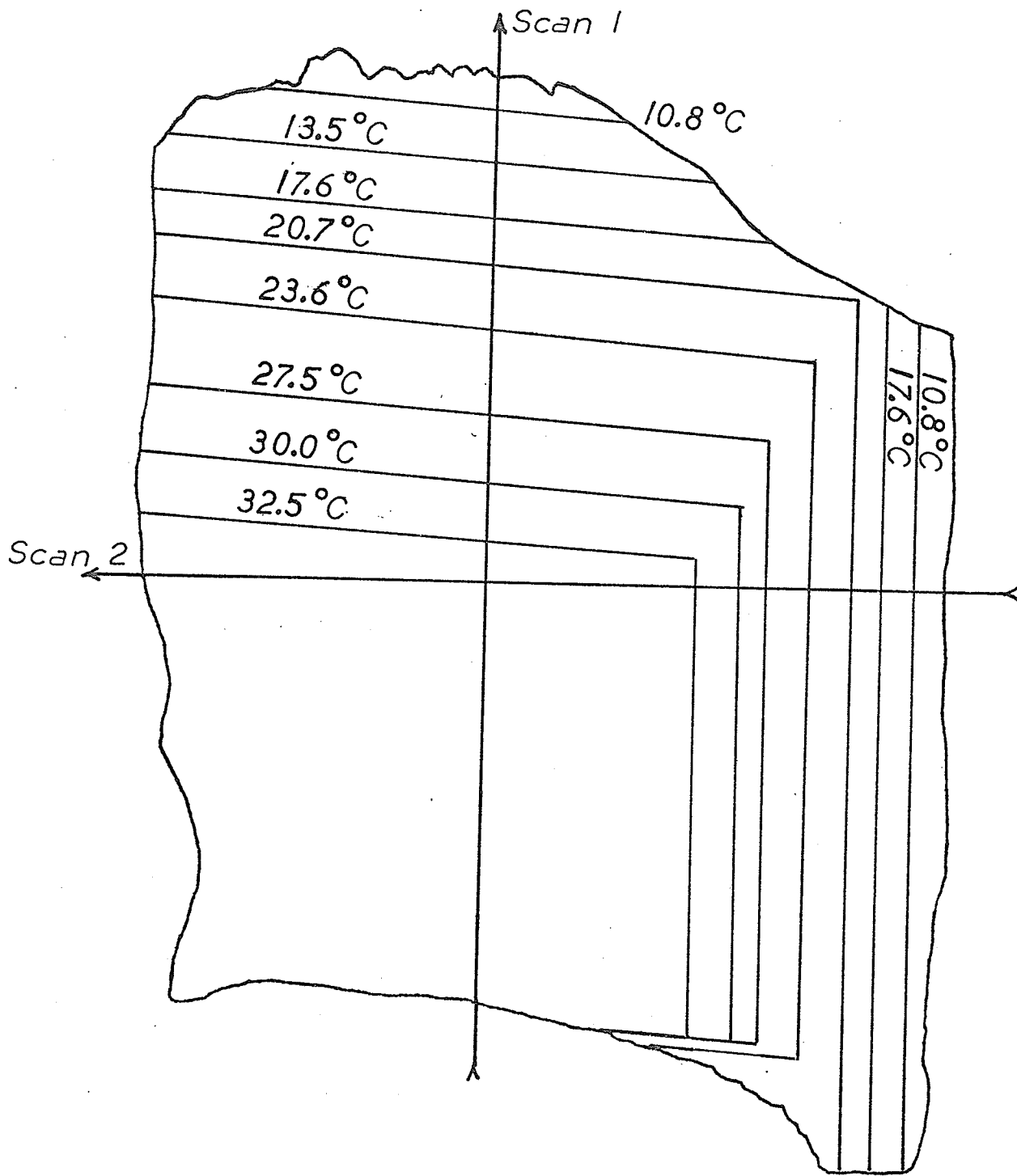


Figure 22.

The WF-AF phase boundaries on a 0.1 mole % Ti doped crystal.



1 mm

The transformation process appeared much more graphically in the case of thin sections as illustrated in Fig. 18(b). In this case the antiferromagnetic regions and weak ferromagnetic regions are very clear. The domain walls do not move as the boundary between the two phases changes position. The temperature sensitivity of this transformation process is illustrated in Fig. 18(c). In these studies at the Morin transition the light intensity of the microscope was reduced by filtering with a green filter and a bottle of water. If however, the light was not filtered it could reverse the transformation by the process of turning the light on and off. In Fig. 18(c), the photograph was obtained immediately after turning the illumination on. The AF-WF boundary was originally at the boundary of the heavily deposited domain walls. The light has made the AF region revert to the WF state which is evidenced by the formation of much lighter domain walls. The formation of these walls occurs a fraction of a second after turning on the light. This sensitivity was not as great in bulk crystals.

In Ti doped specimens the WF-AF boundary is not always a single boundary, but can be a set of several parallel light colloidal walls. This is illustrated in

Fig. 19(f) for a (110) surface of a 0.05 mole % Ti doped bulk crystal. In this case there are two sets of boundary walls parallel to intersection of (110) planes with crystal surface. These walls have a separation of about 50μ .

Another interesting feature in the transformation process is illustrated in Fig. 18(d). In this case a 2 mole % Ga doped thin section is undergoing the transition. A growth layer goes through the transition at a slightly higher temperature than the two adjacent growth layers. This can be seen by the AF region followed by a $\sim 50\mu$ strip of WF region, $\sim 50\mu$ strip of AF region and finally a WF region. An interesting point to note is the lack of change of the domain structure in the WF strip compared to its structure when the crystal was entirely in WF state.

It was not always true that there was no significant change in the domain structure in the transition process. The notable exception to this is most clearly illustrated in a 0.05 mole % Ti doped thin section, in Fig. 19(e). In this case characteristic domain walls form at the AF-WF boundary and gradually disappear as they extend further into the WF region.

After cycling crystals through the Morin transition up to 40 times no memory phenomena for the domain structure in pure crystals was observed. The domain structure reappeared with basically the same type of structure but never in an identical pattern. The effect of cycling is illustrated in Fig. 18(a). However, in doped crystals where the domain structure was poor then the domain structure reappeared in almost identical form.

B. Crystal Physical Properties.

1. X-ray Diffraction and X-ray Fluorescence.

The average distortion from the powder diffraction pictures for the heaviest doped crystals of each type are listed in Table IV. Also given are the accepted ionic radii of the elements. The (232) and (318) lines showed no abnormal broadening to indicate non-stoichiometry or non-uniform doping in the crystals.

The amount of dopant present in the Rh doped crystals obtained from intensity measurements from diffractometer traces of the Rh and Fe present, are 0.37 mole % and 0.75 mole % Rh³⁺ for nominally doped 0.5 mole % and 1.0 mole % Rh³⁺ respectively.

The dopant present on the surface of the 0.5 mole %

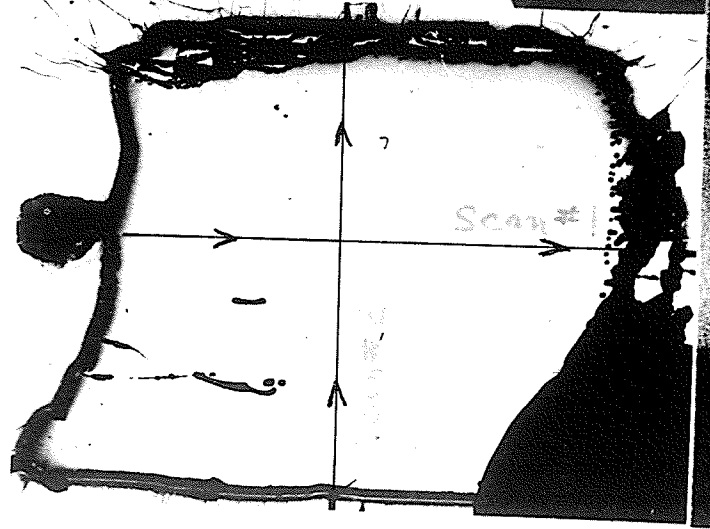
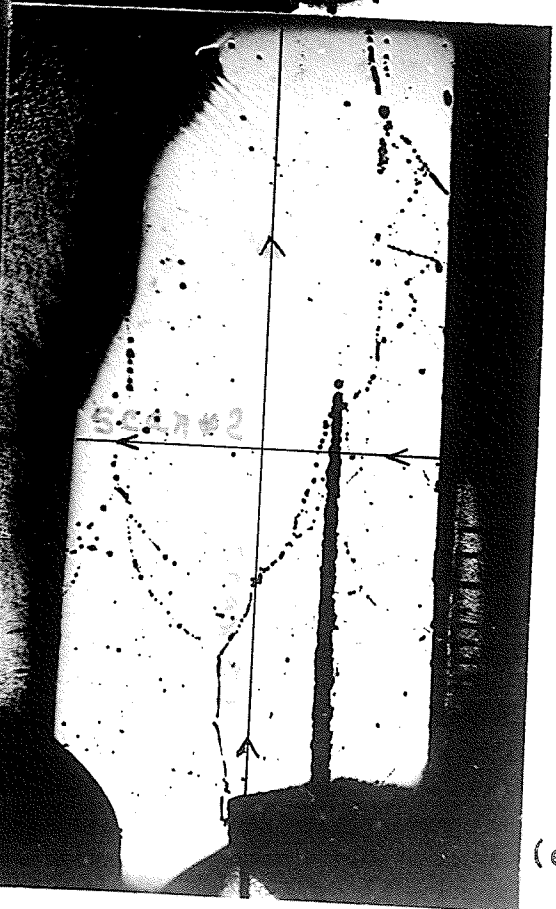
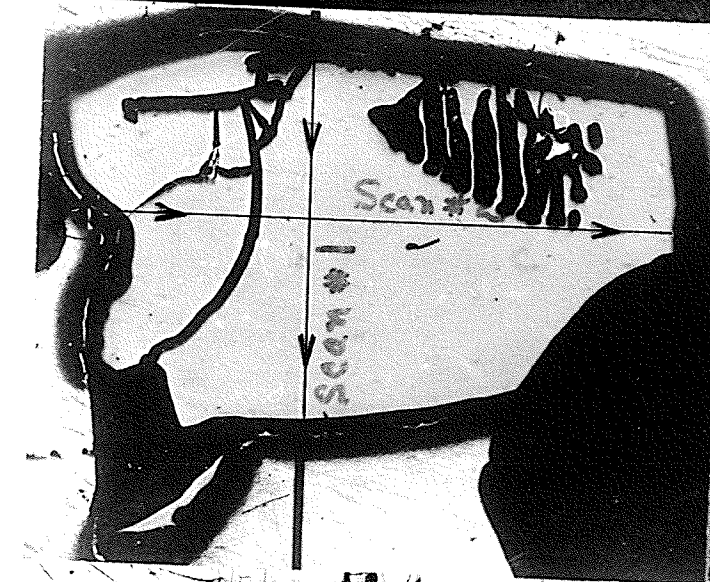
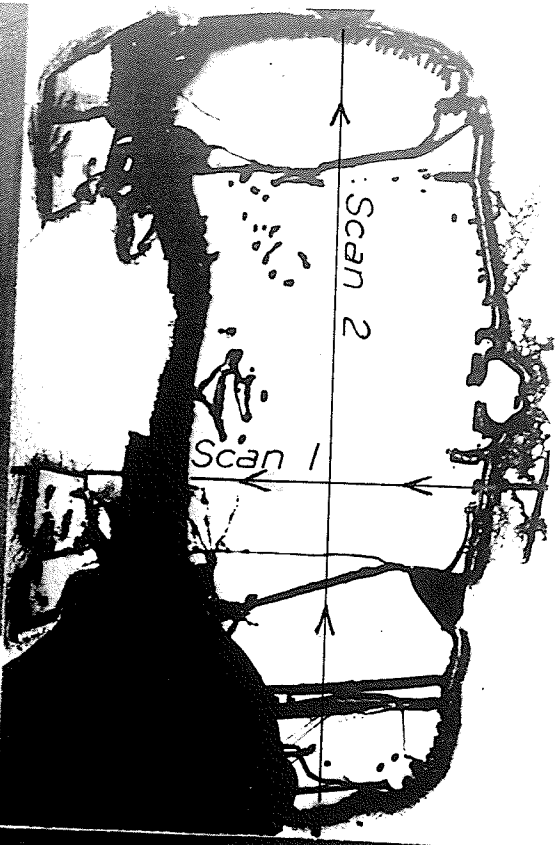
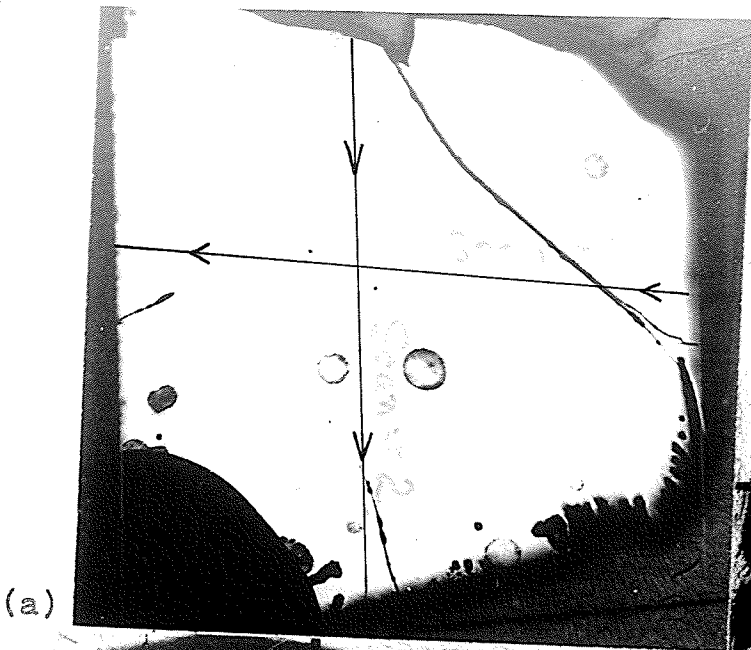
Table IV. Average Distortion of Hematite Lattice from
Fe K α_1 (232) and (318) Reflections.

Nominal Doping	Measured Mole % Doping	2θ (degrees)	d A $^\circ$	% Distortion in d	Ionic Radii A $^\circ$
Pure Fe $^{3+}$	----	156.41(5)	0.98886	----	0.64
2 mole % Ga $^{3+}$	1.38*	156.99	0.9878(3)	-0.10%	0.62
2.5 mole % Al $^{3+}$	1.5 *	156.96	0.9878(9)	-0.10%	0.51
1.0 mole % Rh $^{3+}$	0.75	156.33(5)	0.9890(0)	+0.014%	0.68
0.1 mole % Ti $^{4+}$	0.085*	156.42(5)	0.9888(5)	negligible	0.68

* Besser, Morrish and Searle

Figure 23.

Photographs of crystal surfaces for which the dopant density was measured by the electron microprobe technique. The scan paths are also shown. The crystals analysed were (a) 0.5 mole % Rh, (b) 1.0 mole % Rh, (c) 0.1 mole % Ti, (d) 0.5 mole % Ga and (e) 1.0 mole % Al.



(d)

(e)

Rh doped sample, analysed by the electron microprobe, was measured in single crystal form, and comparing with the ground up standards gave a doping value of 0.5 mole % \pm 10%.

2. Electron Microprobe Analysis.

Photographs of the crystal surfaces studied are illustrated in Fig. 23. The scan paths studied are also indicated. In Fig. 24-27 are graphed the dopant density along the scan paths. Also, plotted on the graphs of Fig. 24-26 are the corresponding Morin transition temperatures along the scan paths obtained from Figs. 20-22. The dopant density was calculated from counts of dopant fluorescent radiation and compared to that of a pure standard⁸⁰. Background counts were obtained by bracketing the fluorescence peak. Thus, the error bars on dopant density are obtained just from the standard statistical error \sqrt{N} for N counts. The Ga and Al doped specimens gave constant density levels across all the scan paths. No value was obtainable for the Gallium doping because no standard was available. The aluminum doping did not give a meaningful value because of the extremely low intensity compared to the background level and also possibly because of absorption in the hematite crystal.

Figure 24.

Graphs of T_M and doping along scan paths obtained from electron microprobe analysis for 0.5 mole % Rh doped crystal.

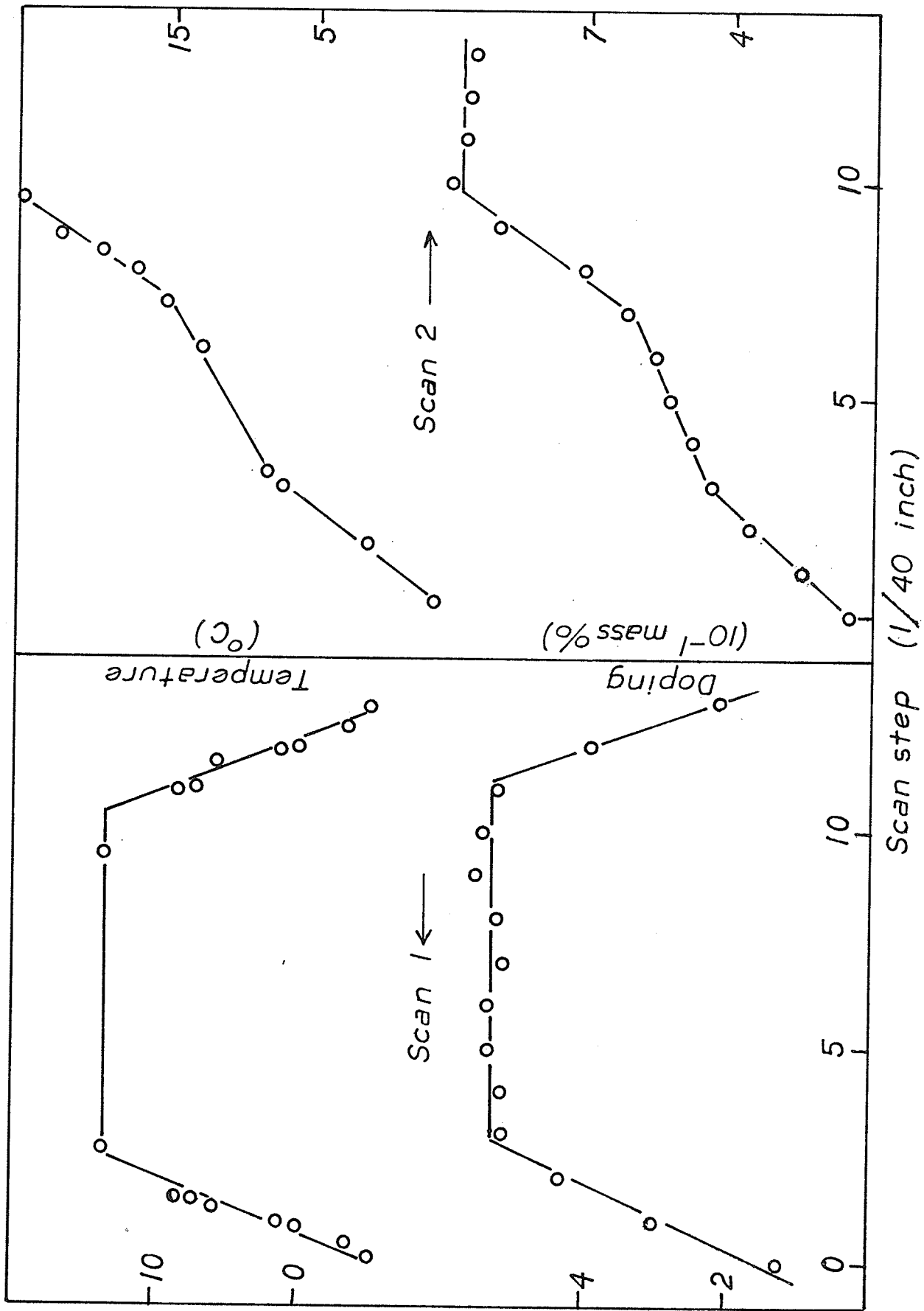


Figure 25..

Graphs of T_M and doping along scan paths for 1.0 mole % Rh doped crystal.

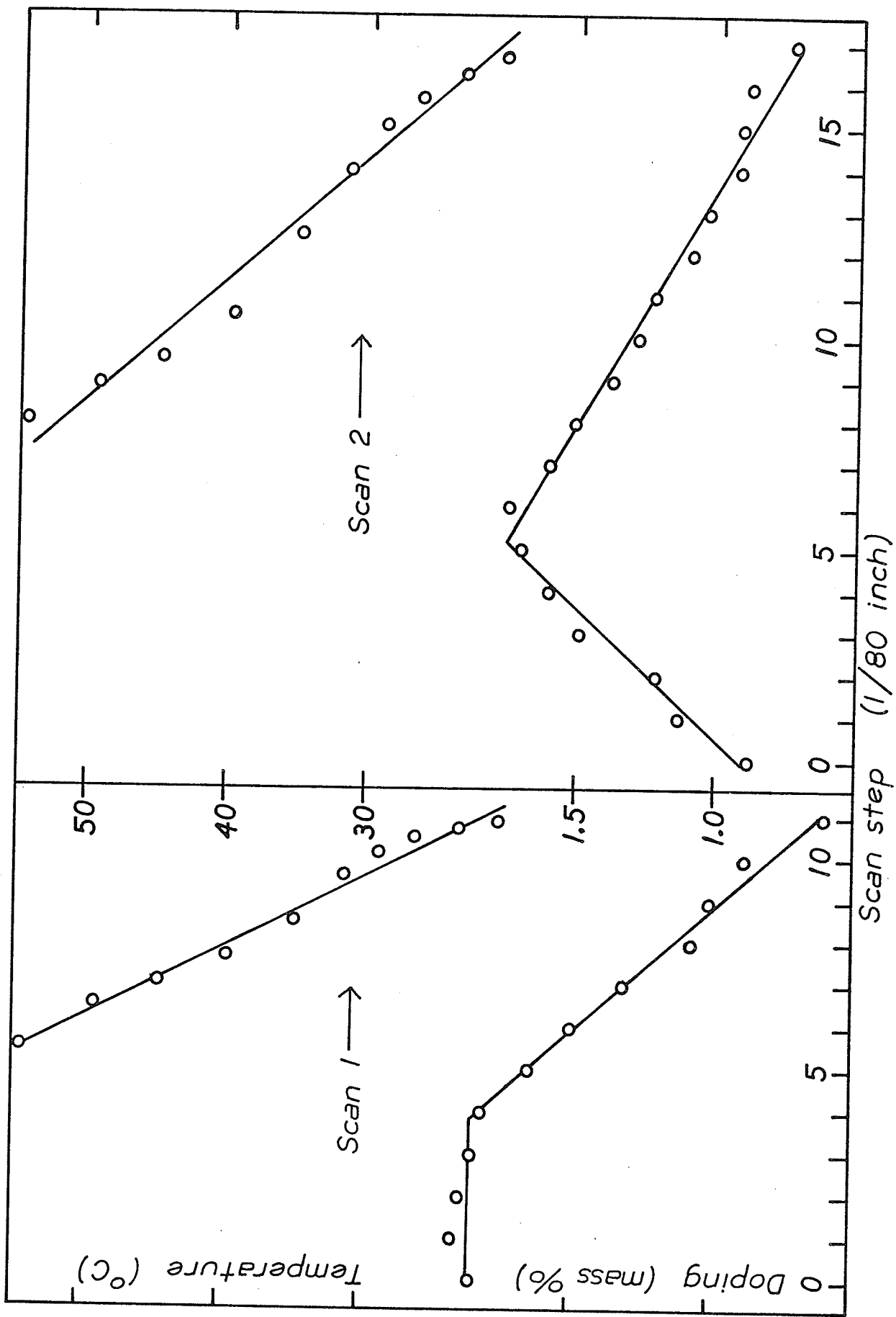


Figure 26.

Graphs of T_M and doping along scan paths for 0.1 mole % Ti doped crystal.

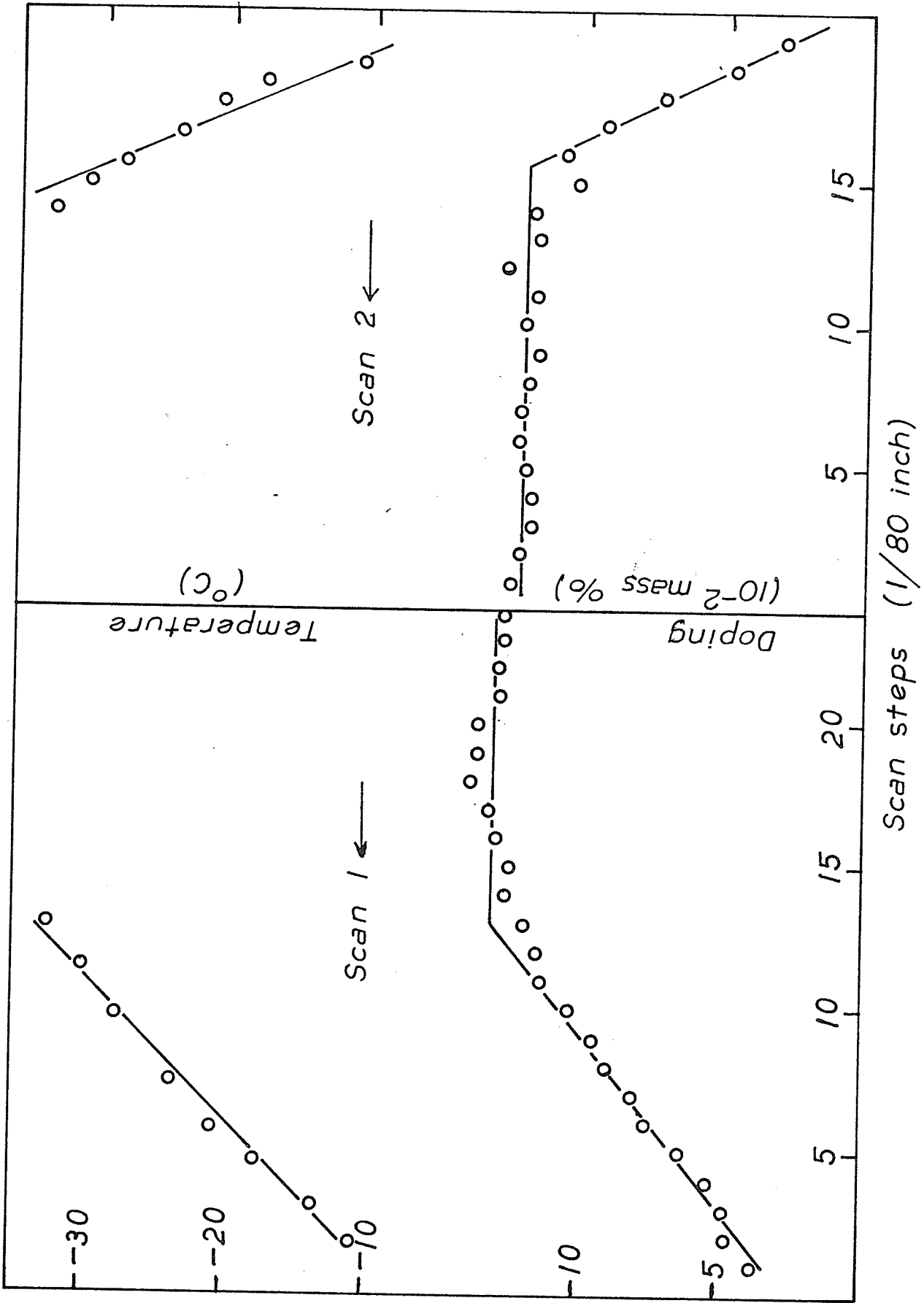
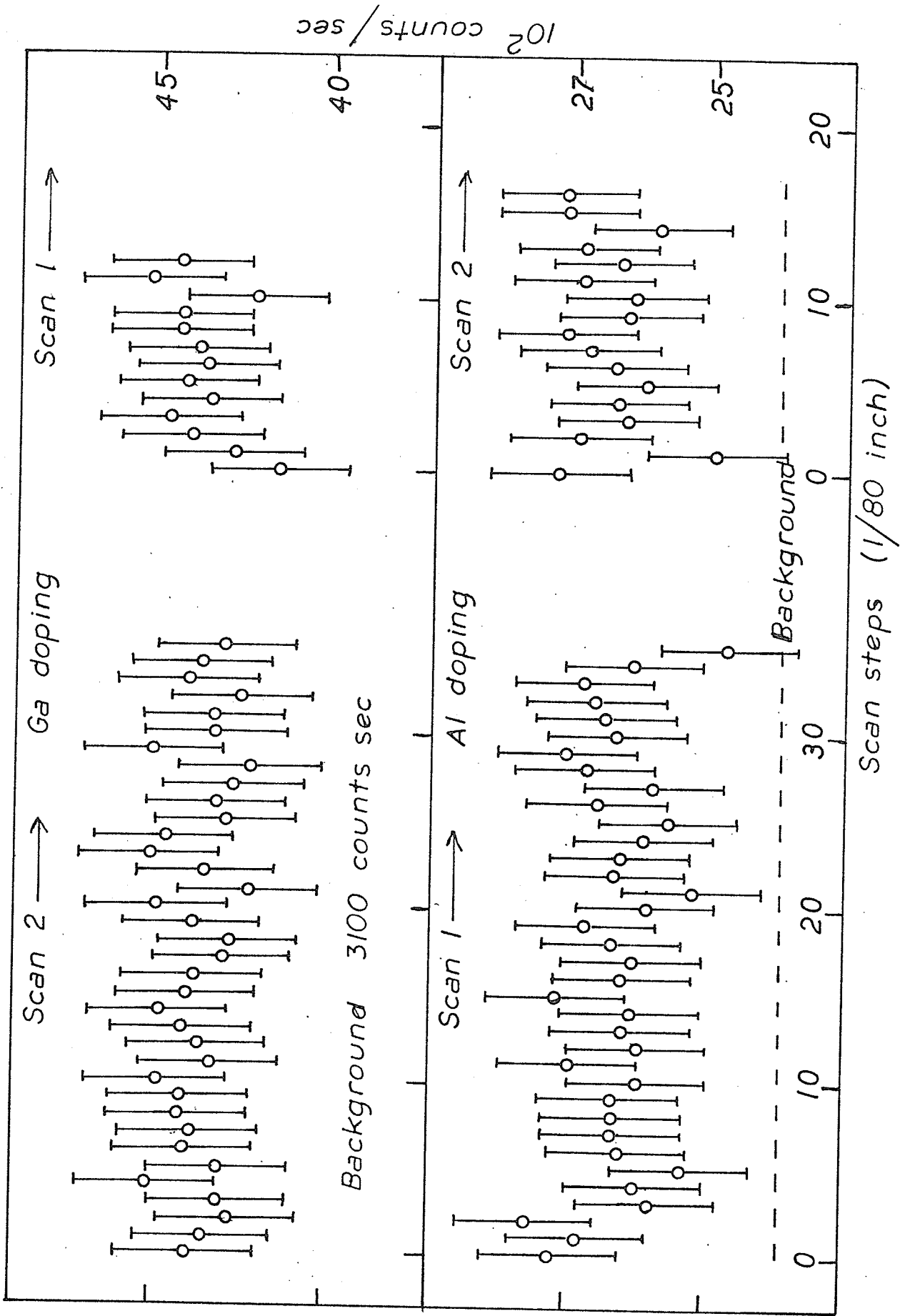


Figure 27.

Graphs of doping along the scan paths of 0.5 mole % Ga and 1.0 mole % Al doped crystals.



3. X-ray Topographic and Optical Observations.

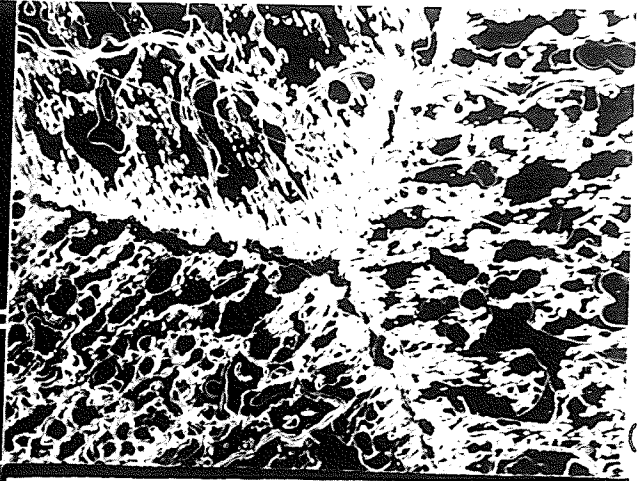
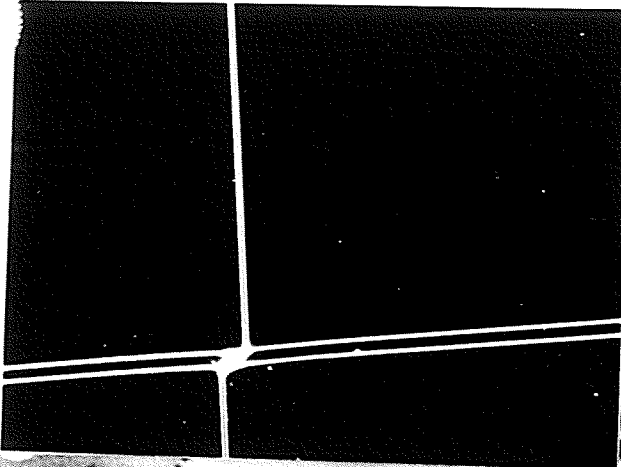
The x-ray topographs of various bulk and thin section polished and high temperature annealed crystal surfaces showed no defects other than those observable with the microscope. The microscope had somewhat better resolution and therefore, all results are those obtained optically. It was hoped that the x-ray topographic studies would show dislocations especially in regions of the crystal where changes in type of domain structure occurred. However, no such defects were observed.

Some of the geometry of the crystals on removal from the flux was described previously. In general, most crystals did not show an ideal box-like structure because of growth conditions in the flux. If the crystal was isolated and grew at the bottom of the crucible then it would be a close approximation to this ideal structure. The face adjacent to the crucible would be the irregular face containing the nucleating point and the termination of successive growth layers. This face would have no specific orientation. An example of this face is illustrated in Fig. 28(d). The nucleating point appears to be in the centre of the face surrounded by triangles of growth layers. As can be seen this crystal does not appear box-like because of the

Figure 28.

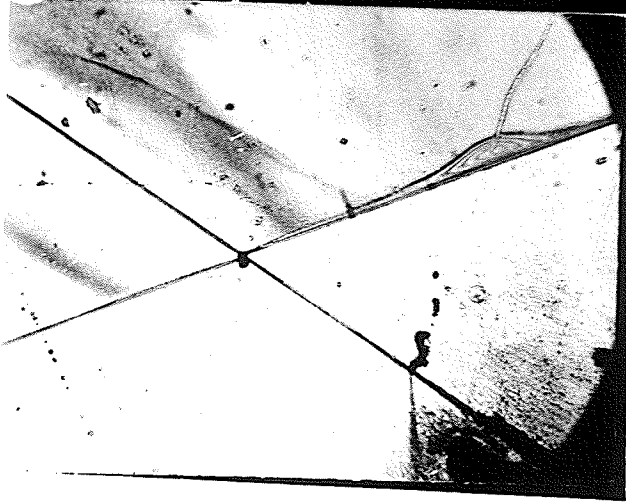
Photographs of crystals and crystal surfaces.

- (a) $(1\bar{1}0)$ polished surface, after annealing, showing twins in dark field contrast.
- (b) Flux etching of a (110) virgin crystal surface.
- (c) Twins on an annealed polished surface in bright field contrast.
- (d) Crystal showing nucleating point surrounded by termination of growth platelets.
- (e) Crystal showing two (110) faces and region where these faces' growth terminated.
- (f) Terraced structure of crystal grown at surface of flux on the side of the crucible.



a)

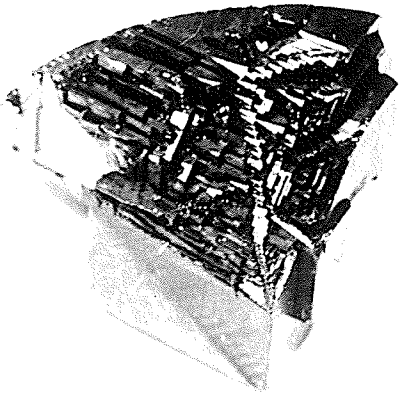
(b)



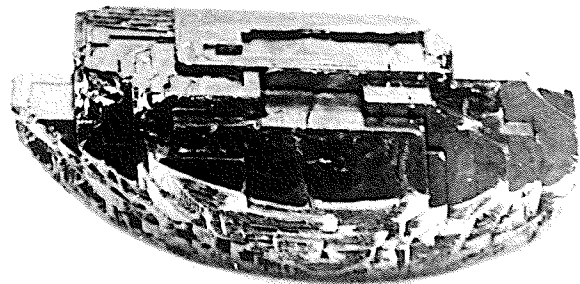
c)



(d)



e)



(f)

presence of other crystal growth interference. Figure 28(e) illustrates some (110) faces of a crystal and a region of termination of growth layers because of interference of a neighbouring crystal. Figure 28(f) shows a crystal grown on the side of the crucible. This crystal shows terraced (110) planes instead of single smooth (110) plane. This type of structure is very typical of doped crystal growth. Figure 28(a), (b) and (c) illustrate microscopic features of crystal surfaces. The appearance of virgin (110) faces is shown in Fig. 28(b). It has a mottled appearance because of flux etching. This etching reveals some type of directional property which divides the surface into three regions. It could perhaps be related to direction of growth of the platelet. Another feature is the presence of a very faint straight line across the surface parallel to intersection of (110) planes with the surface. This is similar to the lines observed on polished surfaces after high temperature annealing. These are typically illustrated in Fig. 28(a) and (c) in dark and bright field contrast respectively. The dark field observation shows that these lines appear in pairs. The distance between them sometimes varies with them finally meeting and disappearing. Bright field showed that these lines

changed contrast on tilting the surface to angles of $\sim 5-10^\circ$. This indicates that these lines are low angle twins. This also explains why they appear in pairs. The angle appears to be about right for a (110) twin since the angle between (110) planes is $\sim 94^\circ$ leading to a $\sim 8^\circ$ tilt between twinned (110) planes.

C. Bulk Magnetization Measurements.

1. Magnetometer Measurements.

Figures 29 and 30 illustrate hysteresis loops for two large bulk specimens before and after annealing. A much smaller well annealed specimen exhibited a hysteresis loop illustrated in Fig. 31. Hysteresis loops showed no difference as a function of orientation in the large bulk samples. In the one large bulk sample, the wasp-waistedness was removed on annealing but for the other it was only partially removed. The better large sample also showed closure at lower fields and a higher moment at closure. The smaller specimen showed no wasp-waist and also showed even higher moment and lower field at closure than the large samples. Figure 32 shows the magnetization versus magnetic field up to nearly saturation. The interesting point is the lack of saturation until about 2-4 kOe which

Figure 29.

Hysteresis loops of pure bulk crystal before and after annealing at 1200°C . This specimen grew at surface of flux.

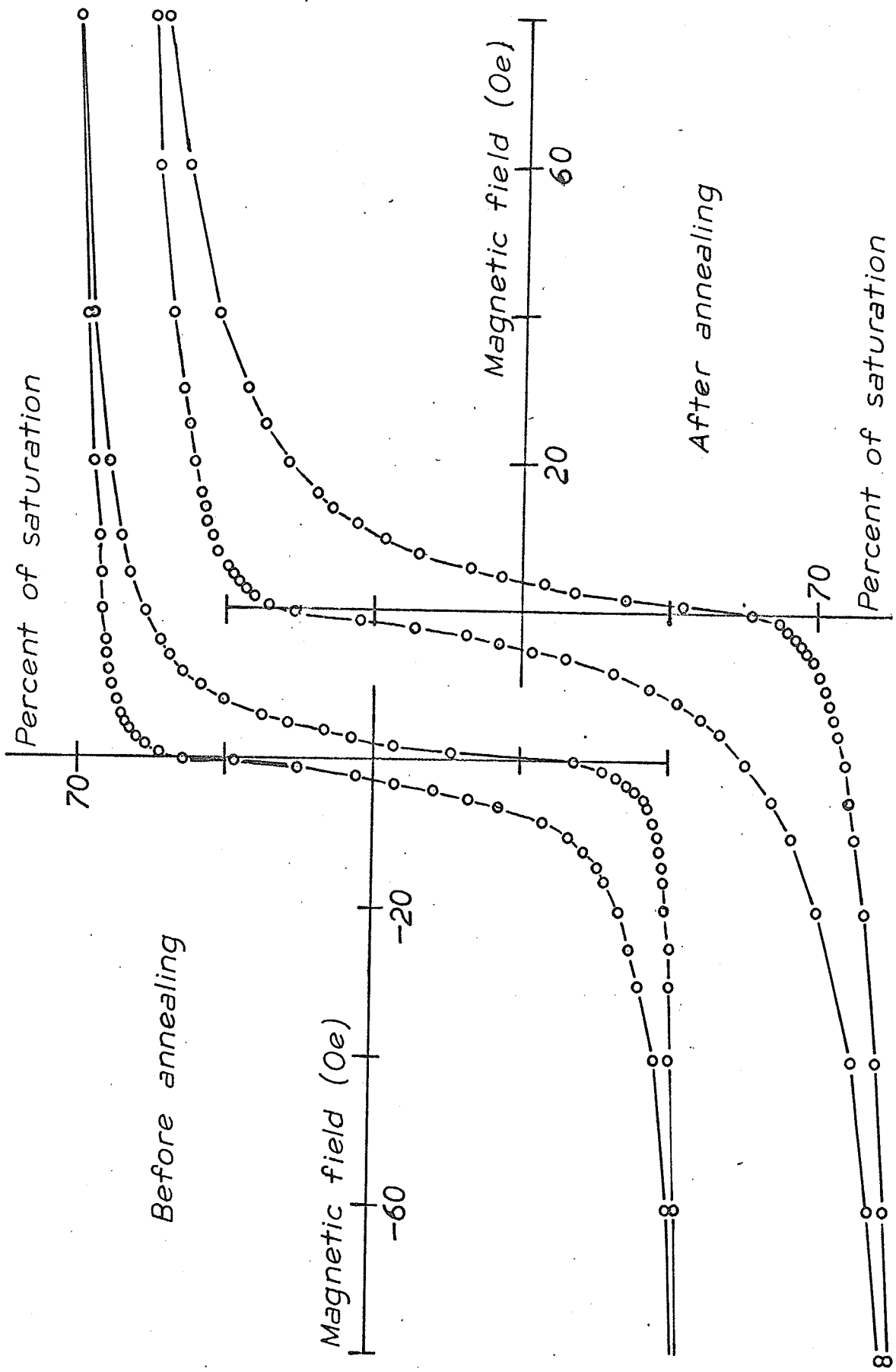


Figure 30.

Hysteresis loops of pure bulk crystal before and after annealing at 1200°C . This crystal grew near the bottom of the crucible.

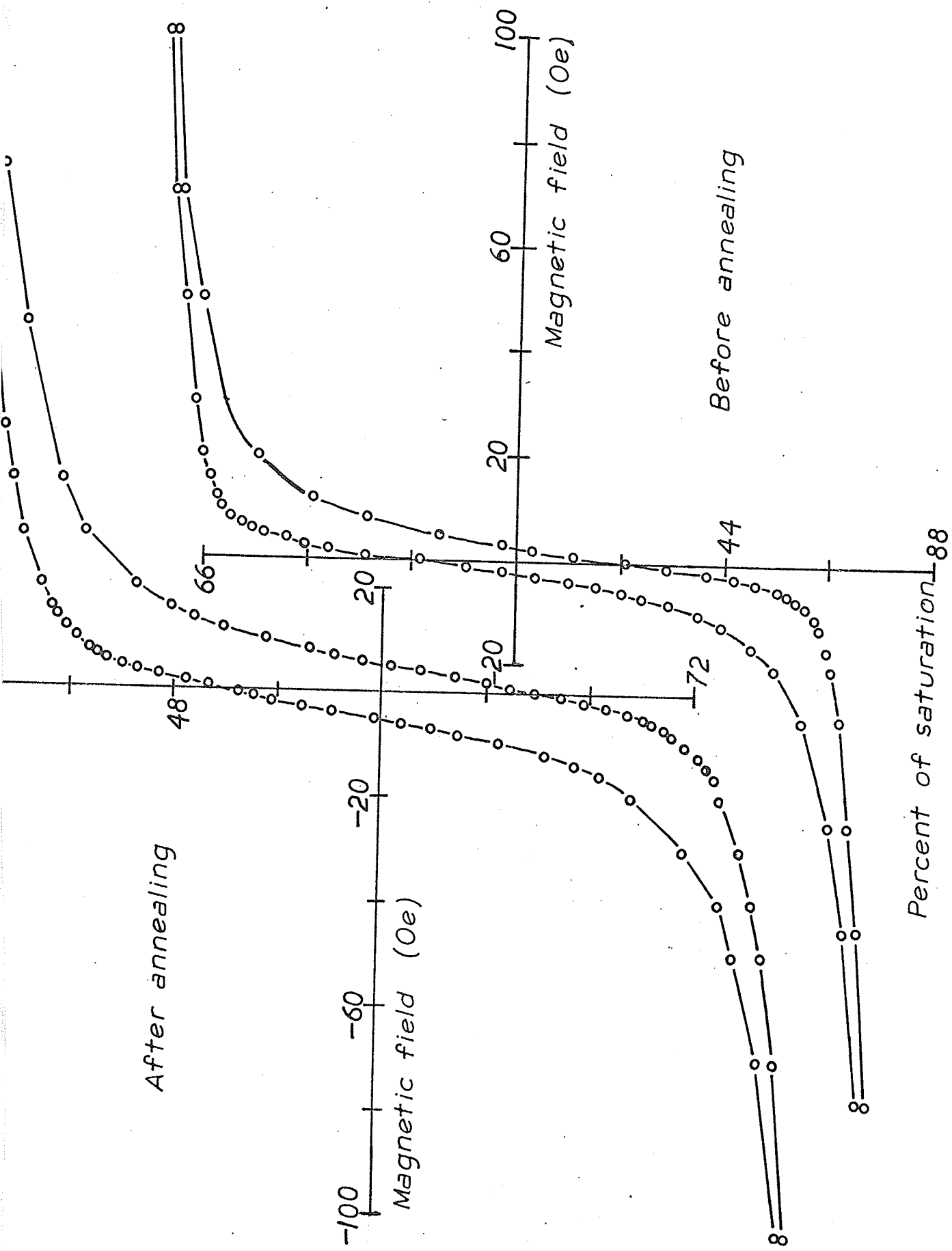


Figure 31.

Hysteresis loop for a small bulk crystal
(0.1" x 0.1" x 0.1").

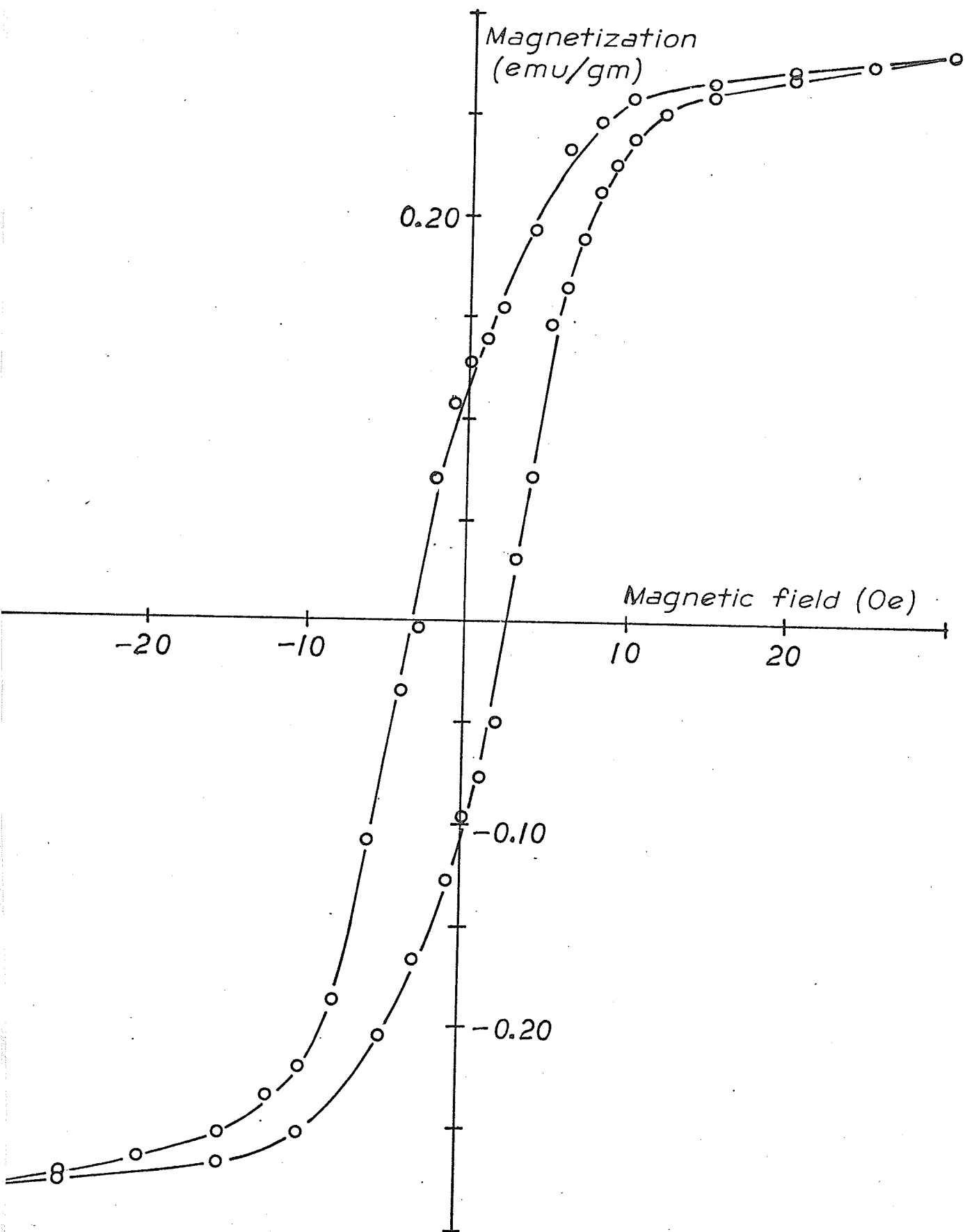
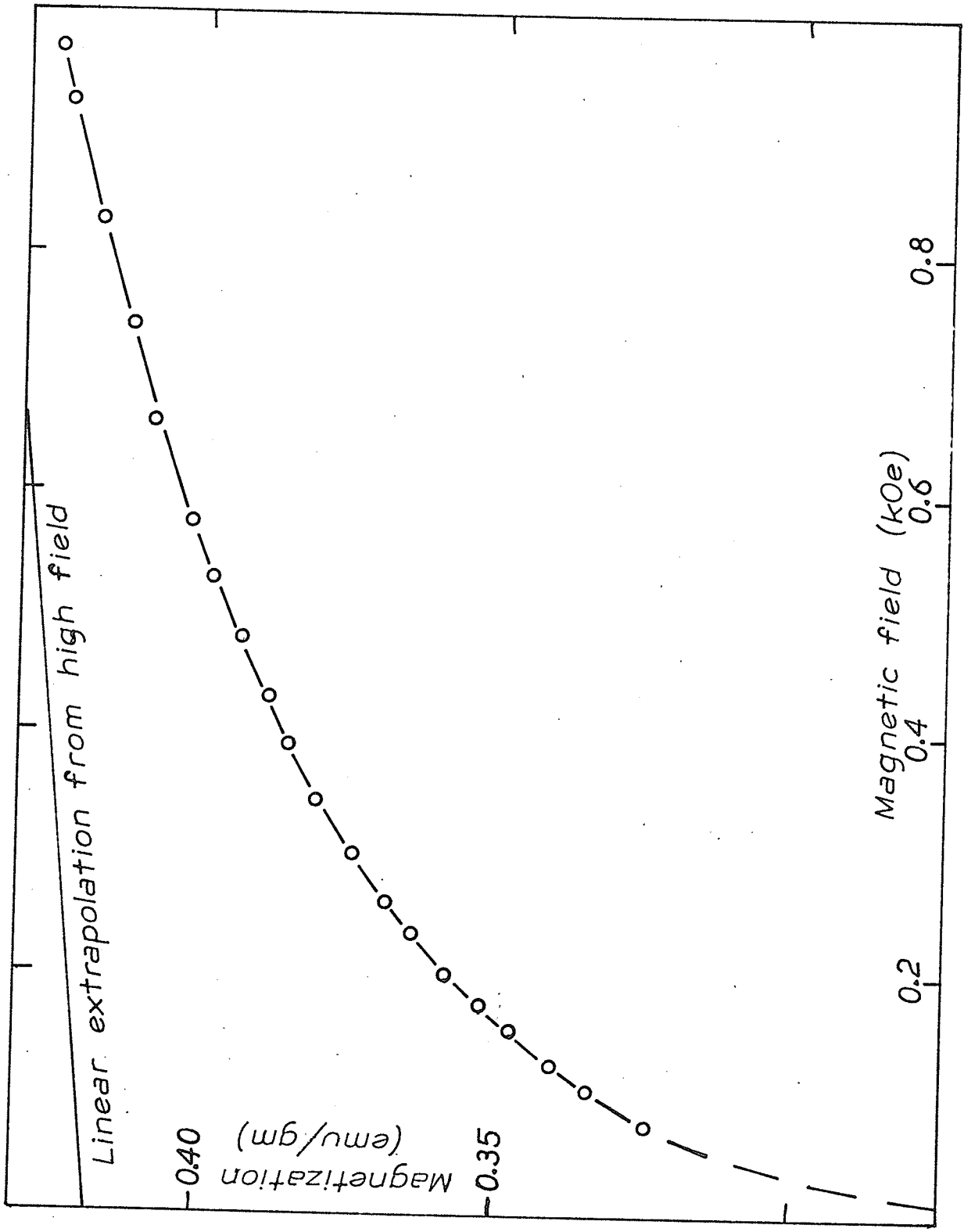


Figure 32.

Magnetization as a function of field in the basal plane and up to saturation, for the same sample as in Fig. 31.



is much larger than the fields of 30-100 Oe required for hysteresis loop closure. Smaller bulk samples also showed a variation in magnetization as a function of direction in the basal plane at fields higher than those necessary for hysteresis loop closure.

Measurement of magnetization versus temperature for the nominally 0.5 and 1.0 mole % Rh doped hematite are illustrated in Fig. 33 and 34 respectively. The magnetization was measured at two field values of 100 Oe and 15 kOe. At 100 Oe, where the field is sufficiently low as not to shift T_M , the samples show a gradual change in magnetization over -5° to 15°C and 15° to 45°C for the 0.5 and 1.0 mole % Rh respectively. The 15 kOe field shifts T_M downward by $\sim 7^\circ\text{C}$ for the nominally 0.5 mole % Rh doped samples.

2. Mössbauer Spectra Observations.

The peak intensities for several 6 peak spectra were obtained by a least squares computer fit to Lorentzian shaped peaks without constraints⁶². The resulting intensities and their errors for the different spectra are given in Table V. The theoretical intensities of the peaks are⁶² $9/4(1+\cos^2\theta)$: $3\sin^2\theta$: $3/4(1+\cos^2\theta)$ for the 1,6:2,5:3,4 peaks respectively. The angle θ is the angle

Figure 33.

Magnetization as a function temperature through the Morin transition at 100 Oe and 15 kOe for a cylindrical 0.5 mole % Rh doped crystal.

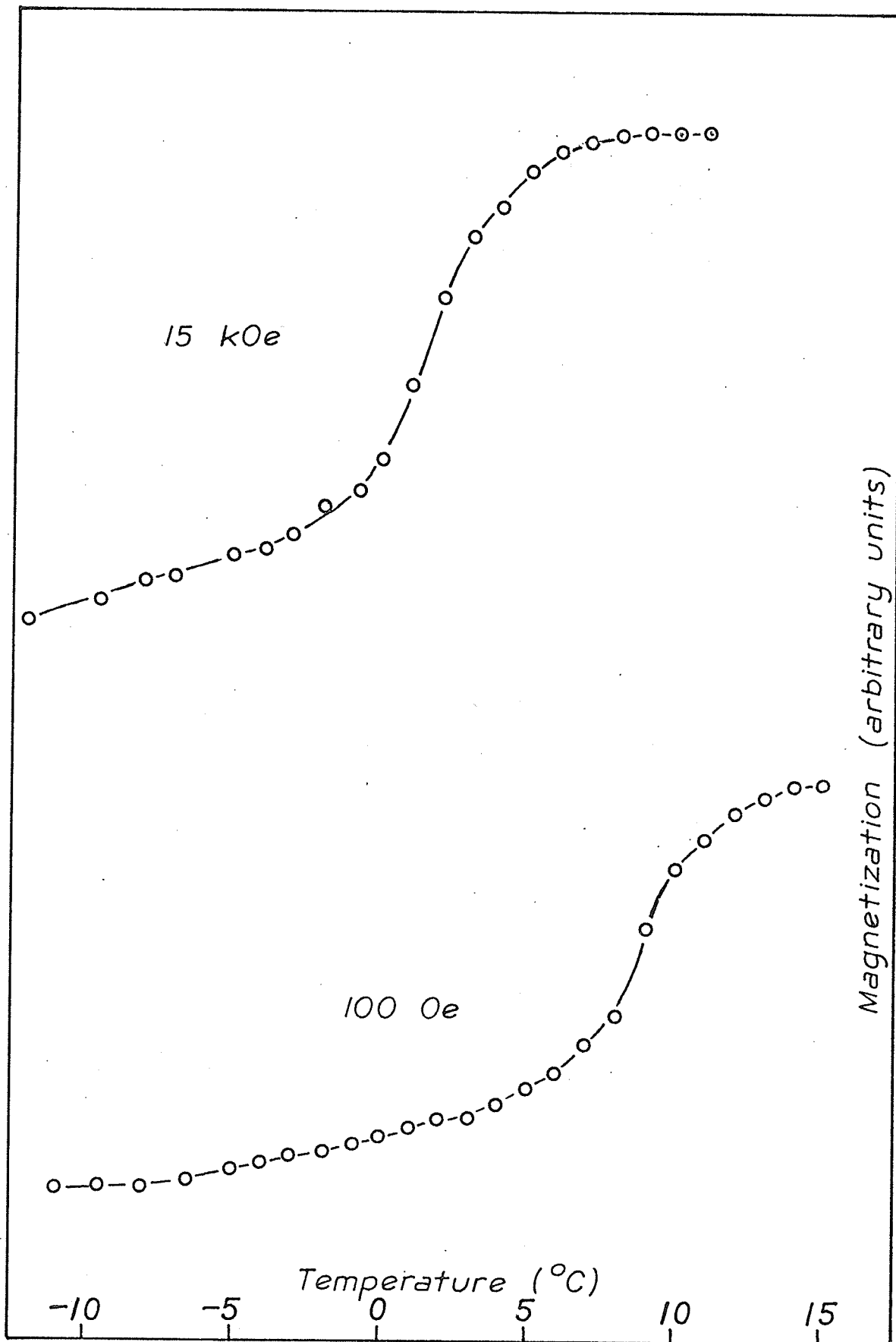


Figure 34.

Magnetization as a function of temperature through
the Morin transition at 100 Oe for a cylindrical
1.0 mole % Rh doped crystal.

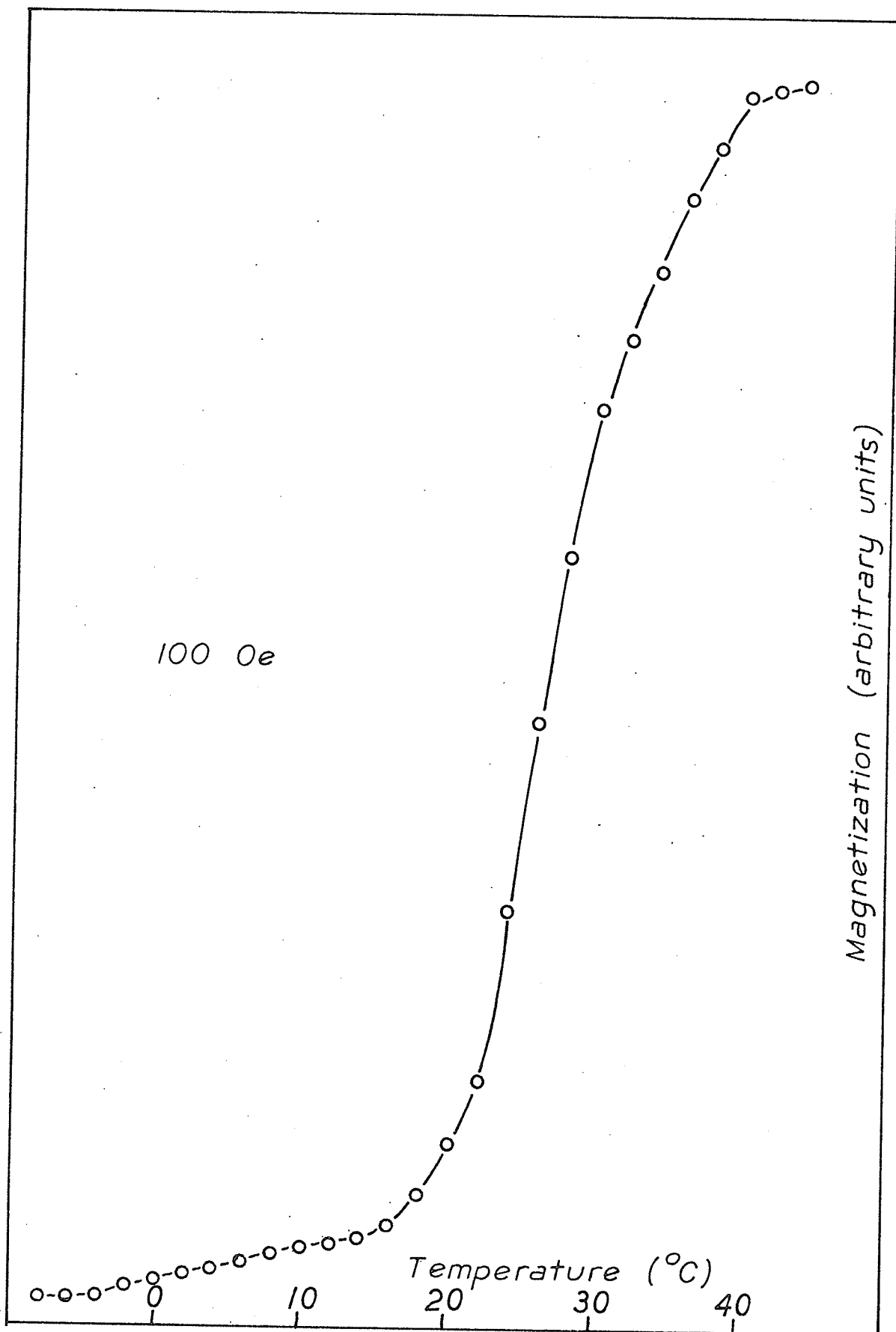


Table V. Mossbauer Spectra Parameters for (110) Thin Section.(a) First 1 mm² region.

Peak Position (PP)	Peak Height (PH) or % Absorption	Peak Width at Half Height (PW $\frac{1}{2}$ H), number of channels	Peak Intensity (PI) = (PH) x (PW $\frac{1}{2}$ H)
1	5.67 \pm 4%	10.2 \pm 6%	57.8
2	2.50 \pm 11%	9.12 \pm 17%	22.8
3	4.28 \pm 7.5%	6.30 \pm 11%	27.0
4	3.41 \pm 9%	7.61 \pm 13%	26.0
5	2.33 \pm 10%	11.3 \pm 15%	26.3
6	5.04 \pm 5%	11.5 \pm 7%	58.0

(b) Second 1 mm² region.

(PP)	PH	PW $\frac{1}{2}$ H	PI
1	8.69 \pm 4%	9.85 \pm 6%	85.4
2	8.19 \pm 4.5%	9.89 \pm 7%	81.0
3	5.23 \pm 8%	8.96 \pm 12%	46.8
4	5.44 \pm 7%	8.38 \pm 11.5%	45.6
5	7.82 \pm 4.5%	10.1 \pm 7%	79.0
6	7.53 \pm 4.5%	10.7 \pm 6.5%	80.6

Table V. continued

(c) Third 1 mm² region.

(PP)	PH	PW $\frac{1}{2}$ H	PI
1	4.49 \pm 5%	12.4 \pm 7%	55.7
2	2.73 \pm 9%	9.10 \pm 18%	24.8
3	3.01 \pm 9%	9.35 \pm 13%	28.1
4	3.63 \pm 9%	6.54 \pm 15%	23.8
5	2.59 \pm 10%	9.07 \pm 19%	23.5
6	4.89 \pm 5%	9.55 \pm 8%	46.6

(d) Whole thin section.

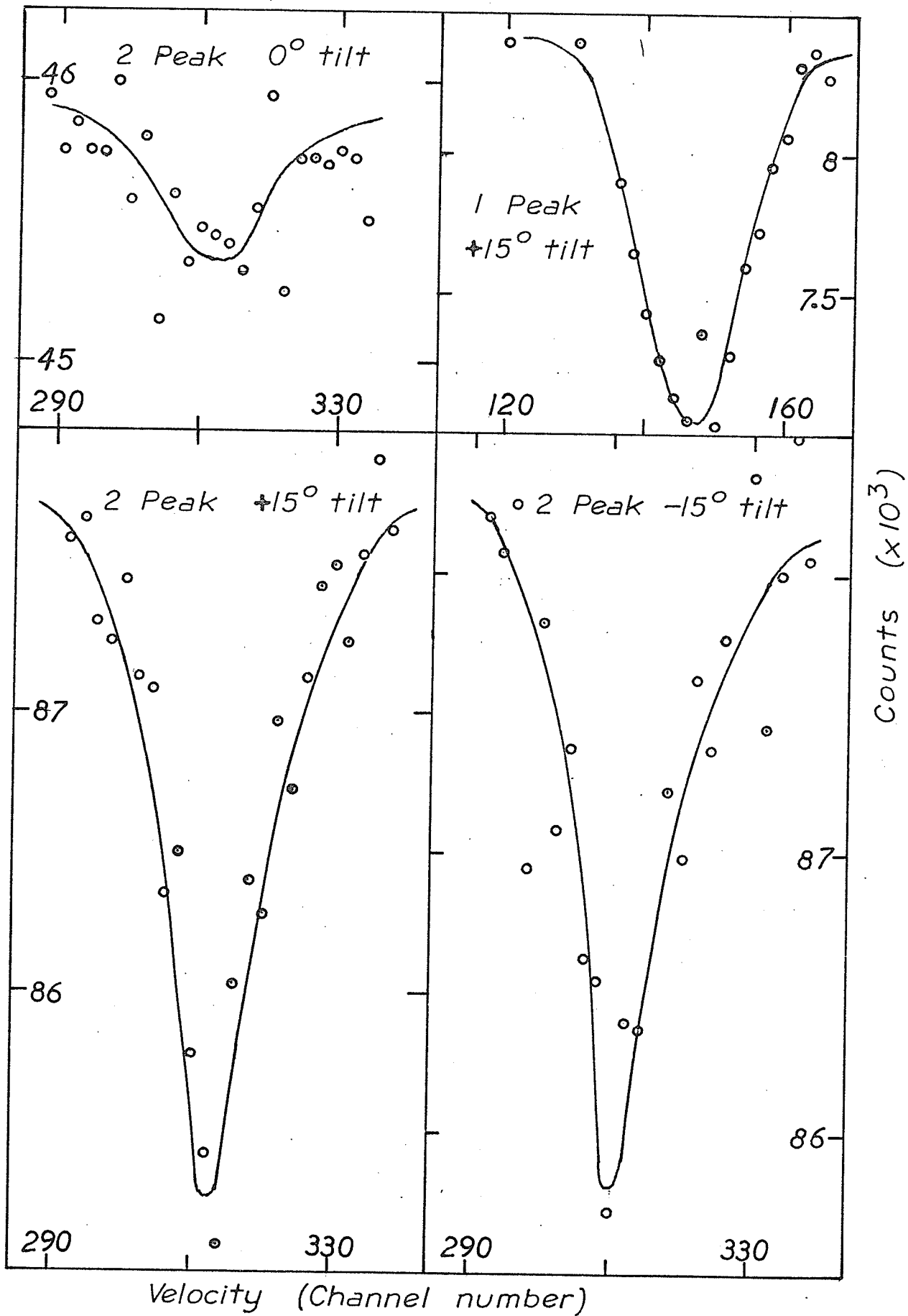
(PP)	PH	PW $\frac{1}{2}$ H	PI
1	13.5 \pm 1.1%	12.6 \pm 1.6%	170
2	7.70 \pm 2.2%	10.6 \pm 3%	81.5
3	10.4 \pm 1.1%	7.99 \pm 4%	83.0
4	10.2 \pm 1.1%	8.61 \pm 3%	87.0
5	7.62 \pm 2.3%	10.3 \pm 3%	78.5
6	13.1 \pm 11%	12.5 \pm 1.7%	164

between the direction of propagation of the gamma rays and the antiferromagnetic axis. Assuming in the case of domains that the angle the moment makes with the crystal surface is either $\pm\phi$ or $\phi, \phi+180^\circ$ then $\theta = \pm 90^\circ + \phi$. Therefore, the average value of ϕ can be obtained from the Mössbauer spectra data and is given in Table V.

The results of the experiment to determining the antiferromagnetic axis angle relative to the basal plane are illustrated in Fig. 35. Plotted are the 2 peak for 0° and $\pm 15^\circ$ tilts and the 1 peak for 15° tilt. Calculation of the angle θ from the theoretical intensities gives $\theta = 15$ and $\pm 24^\circ$ for tilts of 0° and $\pm 15^\circ$ respectively.

Figure 35.

Mossbauer spectra for $\pm 15^\circ$ and 0° orientation of a $(1\bar{1}0)$ thin section. The 1 peak is shown only for 15° orientation and the 2 peak for all orientations.



V. Discussion of Results.

A. The Domain Structure of Hematite.

1. The Orientation of the Domains' Magnetizations.

For the N-domains a structure consistent with the observations is a 180° wall structure of slab-like domains and/or cylindrical domains of irregular cross-section⁷⁴. This structure ideally is then indicative of a stripe domain structure. Thus, the stripe domain structure equation for domain wall energies can be applied to obtain estimates of wall energies. For the bulk crystals these will be very rough but should be somewhat better in the case of the thin sections. The data of Table III give values of $f_w \sim 10^{-2}$ ergs/cm² for bulk crystals and $3-15 \times 10^{-2}$ ergs/cm² with the best values being $\sim 3 \times 10^{-2}$ ergs/cm² for thin sections. The calculations from thin sections assumed that the moment is perpendicular to the surface. However, this is not necessarily true. If instead the magnetizations make an angle ϕ with surface then the domain energy is actually reduced by $\sin^2 \phi$. Therefore, the values calculated are upper bounds on the domain wall energy.

What is the angle ϕ ? Magnetostatic energy would prefer ϕ to be zero for thin sections. Therefore, some kind of anisotropy is responsible. Magnetocrystalline

in-plane anisotropy is extremely small but possibly sufficient to produce a non-zero ϕ . However, sections cut parallel to the hard and easy directions indicate that this is not the real cause. Therefore, the only other cause is magnetoelastic anisotropies. These would arise only if strains were present in the crystals. That this is the case is clear from the Mössbauer data in Table V. The large change in the relative intensities of the peaks for different parts of the thin section indicates there is a large change in the angle θ over the crystal. That these variations occur is also indicated by the apparent changes in domain structure over many thin-sections. Since, typically, the magneto-static energies of the stripe domain structures are $\sim 0.1 \text{ ergs/cm}^3$ and the magnetoelastic coupling constants are $\sim 10^{-5} \text{ to } 10^{-6} \text{ ergs/cm}^3$ then extremely small average strains $\sim 2 \cdot 10^{-9}$ would be sufficient.

Therefore, a reasonable model is a variation of θ over the whole domain structure in order to accommodate a variation of strain in the crystal. However, the density of flux indicates that although this variation of angles occurs, the domain angles $\pm\phi$ are not too small and are closer to $\pm 90^\circ$ than 0° . If ϕ becomes too small the 180°

domain structure does not appear to be the most stable structure and this structure disappears or converts to a CN-domain structure.

The CN-domains appear to be non 180° walls with the domains having the moment at $\pm\phi$ with respect to crystal surface. The evidence for this is the switching of the domain walls at ~ 4 Oe on reversing the direction of the magnetic field parallel to the crystal surface but with the field still indicating the presence of only two domain phases. Also, the faintness of the colloid walls indicates that ϕ is considerably less than 90° except where they terminate at N-domains. The angle ϕ still appears to vary from place to place in the crystal since they generally disappear and reappear in various regions of the surface. The fact that the angle between adjacent domains is 2ϕ also would then account for the appearance of very wide N-domains superimposed on the CN-domains observed in one case. The wall energy of the CN-domains is then $f_w \sim 10^{-1} \sin^2 \phi$ ergs/cm². Unfortunately, it does not appear possible that this type of domain structure is stabilized by in-plane magnetocrystalline anisotropy since it is observed only in $(1\bar{1}0)$ thin sections which contain the easy direction for magnetization. The one

specimen which they almost completely covered was a particularly well annealed highly perfect specimen. Therefore, it must be stabilized by only very small strains. However, in the case where they coexisted with a mainly N-domain structure they occur because of changing states of strain in the crystal.

The C-domains do not appear to behave as real domains at all, however, they do indicate some kind of regular significant spatial variation in the magnetization. The most important feature, as with CN-domains is their unusual direction from which they do not deviate. Another important feature is the colloid density tendency to change in intensity, finally, disappearing in many regions. This indicates a spatial variation of the moment in the domain itself. The narrow width would indicate, on the basis of the stripe domain formula a wall energy possibly considerably less than 10^{-2} ergs/cm.

The unusual behaviour of the domain structures in a magnetic field and their unusual character in some cases indicates that there are some strongly anisotropic effects occurring. The magnetocrystalline anisotropy does not appear to fit in with this behaviour. The basal plane anisotropy is very weak and if it did have any

effect there should be characteristic signs of three-fold behaviour. The out-of-basal plane anisotropy is so large that it can be effectively regarded as infinite for domain behaviour. Thus, all that remains is magnetoelastic coupling.

Clearly, the regularity of the three domain types indicate that if the magnetoelastic interaction is the important interaction for all domains then this interaction must have some fundamental nature rather than just a random interaction with strain causing crystal defects. A reasonable assumption for a domain structure is that there be no magnetoelastic interaction between adjacent domains. Clearly this condition is satisfied if the domains are in exactly the same strain state. From the discussion in the introduction it is clear that 180° domains satisfy this condition. The out-of-basal plane shear components rotate 360° when the moment rotates 180° and all the other components depend only on the direction not the sign of the moment. Therefore, such walls could be in arbitrary directions and would appear to explain the N-domains.

However, this may be too restrictive a condition. A more general condition for no interaction is for the

magnetostriction parallel to the domain walls to be constant going from one domain to another. The conditions under which this can occur can be determined from equation (15) which for the weakly canted state can be reduced to the form

$$\lambda_{\sigma} = (\alpha_x^2 - \alpha_y^2)N \cos 2\phi + 2\alpha_x\alpha_y N \sin 2\phi \\ + 2\alpha_x\alpha_z L \sin 2\phi + 2\alpha_y\alpha_z L \cos 2\phi$$

where ϕ is the angle the spin axis makes with the x axis or the moment makes with the y axis. Then if two adjacent domains have moments along ϕ_1 , and ϕ_2 then it is required that $\lambda_{\sigma}(\phi_1) = \lambda_{\sigma}(\phi_2)$ parallel to the domain wall. The most reasonable structure to consider is $\phi_2 = -\phi_1$ or $180-\phi_1$ since nearly all of the surfaces studied were parallel to either the x or y axis. Also, the resulting expression would then be complex and lead to no meaningful solution for any other case. If $\phi_1 = \phi$ for convenience then for the two cases suggested, setting

$$\lambda_{\sigma}(\phi) - \lambda_{\sigma}(180-\phi) = 0$$

gives

$$N\alpha_x\alpha_y + L\alpha_x\alpha_z = 0$$

This expression results in two solutions for a plane.

They are $\alpha_x = 0$ or $\frac{\alpha_y}{\alpha_z} = -\frac{L}{N}$. It is fortuitous that these cases lead to a plane across which the parallel components of λ_v are constant, since this is exactly the requirement for domain walls. Therefore, domain phases making angles $\pm\phi$ with respect to the x or y axis require the domain walls to be parallel to either the y-z plane or the plane parallel to the x axis at angle ψ to the y axis. The second plane is given by

$$\frac{\alpha_y}{\alpha_z} = \tan \psi = -\frac{L}{N} = -\frac{8.5}{3.4} \pm 20\%$$

using the measurements of Levitin et al^{30,63}, which gives a value $\psi = -22^\circ \pm 4^\circ$. The basal plane has threefold symmetry, therefore, the coordinate system may be rotated $\pm 120^\circ$ about the z axis and similar results hold for these coordinate systems. It would appear that these walls are a possible explanation for the C- and CN-domains observed.

The CN-domains were measured to have an angle $\psi \sim -26^\circ \pm 2^\circ$ with the y axis in the $(1\bar{1}0)$ surface which is in reasonable agreement with the value calculated for ψ . These walls might be present on a $(11\bar{2})$ surface, however, they would be difficult to distinguish from 180° domains since the $(11\bar{2})$ surface contains the x-z plane. Walls

parallel to the y-z plane should be visible in the $(11\bar{2})$ plane but not $(1\bar{1}0)$ planes. This could then explain the walls perpendicular to basal plane observed in the $(11\bar{2})$ thin section of Fig. 13(c) which gradually disappear. The domain moments' angles $\pm\phi$ are slowly varying to zero as the walls move further away from the defect region.

The explanation for the C-domains appears to be the projection of the planes $\frac{\alpha_y}{\alpha_z} = \frac{-L}{N}$ from two of the three possible coordinate systems onto the (110) planes. These planes make an angle of $\sim \pm 22^\circ$ with the x axis of the third coordinate system in the (110) plane. The third coordinate system's x axis lies in the (110) plane itself so that the plane $\frac{\alpha_y}{\alpha_z} = \frac{-L}{N}$ would result in domain walls indistinguishable from N-domain walls. The $\pm 22^\circ$ is in reasonable agreement with the measured $\pm 23.5^\circ$ for pure specimens the discrepancy for the Ti doped case could possibly be caused by a small change in the magnitude of some of the magnetoelastic interactions. In the case of Ti, the valence is +4 which produces a strong coupling with the magnetic sub-lattices.

The difficulty with this explanation is that the two domain phases would have unsymmetric magnetic charge

densities at the crystal surface. Therefore, such a domain structure could not be stabilized magnetostatically. However, there is evidence to suggest that it could be stabilized magnetoelastically by a changing shear stress through the crystal as occurs at the AF-WF boundary. These type of walls, in the case of some doped crystals, form in the WF phase at the boundary as illustrated in Fig. 19(c), (d), (e) or (f). In the AF phase there is no magnetostriction and therefore, the average magnetostriction parallel to the (110) AF-WF boundaries would try to be as small as possible. This could occur if the moment in the WF phase rotated $\pm 45^\circ$ in the basal plane at the boundary. This would result in the apparent C-domain wall at the boundary which would gradually disappear further away from the boundary.

For the case where these domains appear without an AF-WF boundary the stabilizing influence could be the growth structure of the crystal. That shear stress occurs in the crystal is evidenced by the appearance of (110) twins on annealing. This suggests that each growth layer could be associated with a shear stress producing a variation of shear stresses in going from one (110) growth layer to the next. This could then result in a

plus and minus variation of the moment or spin-axis angle relative to the (110) growth layer across the layers.

2. The Structure of the Domain Walls.

a) The N-Domain Wall.

Since hematite has its ferromagnetic component produced by a very small canting between two anti-ferromagnetic sub-lattices, two distinct types of 180° wall models are possible. The two classes of walls are an antiferromagnetic-ferromagnetic (AF-F) and a purely ferromagnetic (F) wall as suggested by Nathans et al.⁶⁴ These two models for walls parallel to the basal plane are illustrated in Figs. 36 and 37 respectively.

Since magnetoelastic interaction energies resulted in walls with energies 10^{-1} ergs/cm², we proposed⁶⁵ that the 180° walls were F walls in order to account for the observed much lower domain wall energies. The unusual nature of this wall requires that the canting vector change sign across the wall. This proposal led to a certain amount of controversy about its validity.^{66,67,68} However, since the work of Levitin et al.³⁰ it has been possible to make a more careful analysis of the magneto-

Figure 36.

Model for an antiferromagnetic-ferromagnetic domain
wall parallel to the (111) plane.

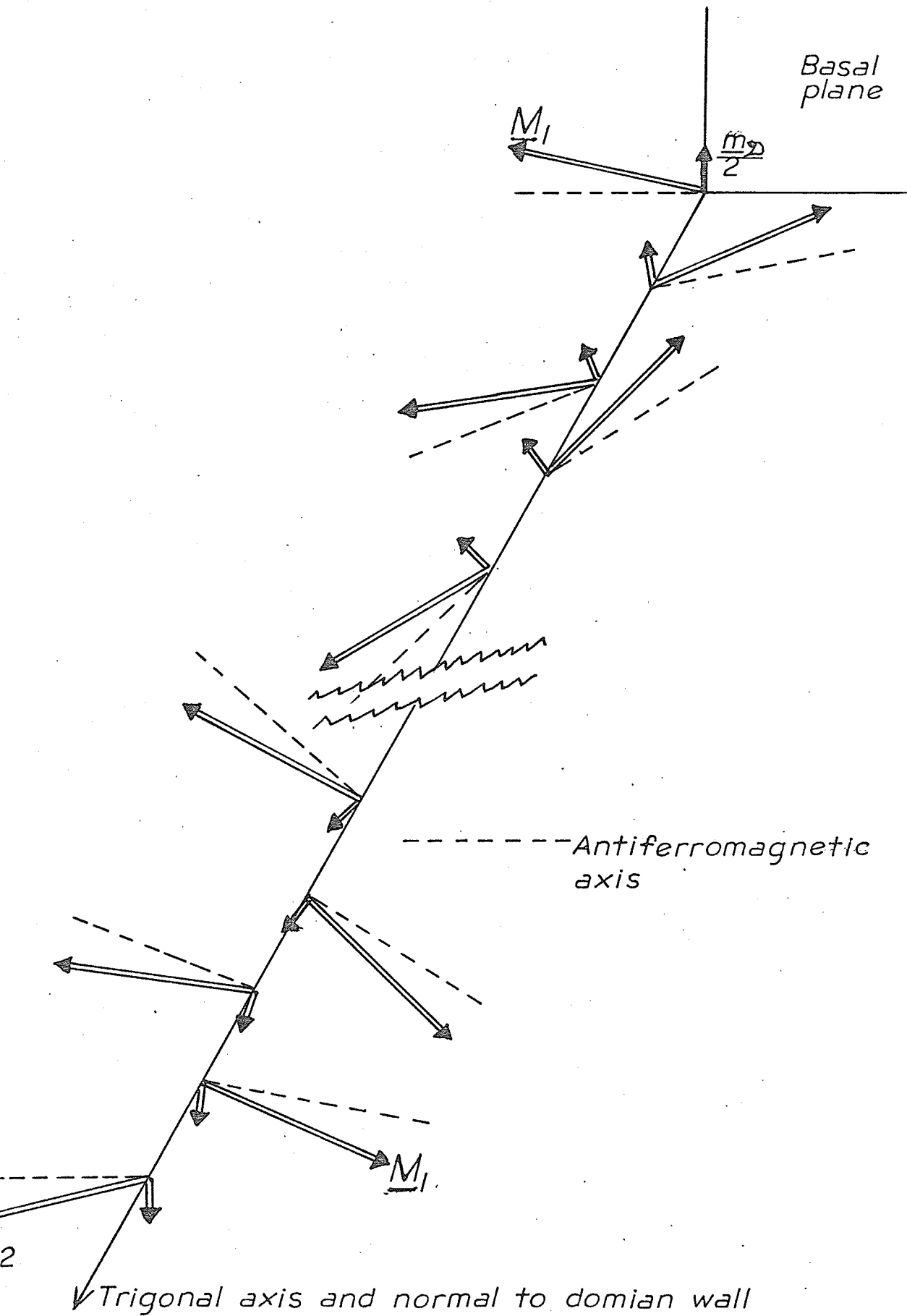
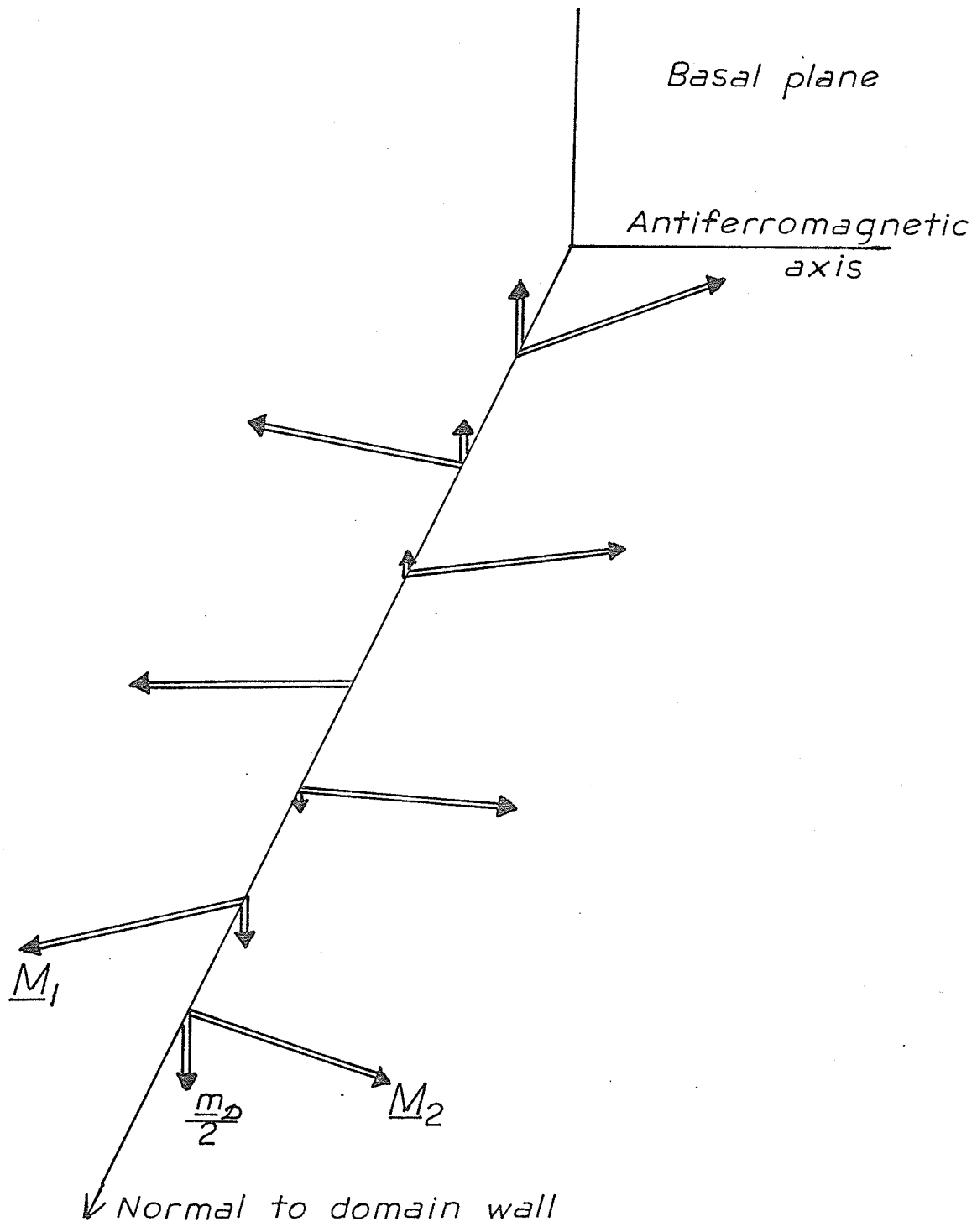


Figure 37.

Model for a ferromagnetic domain wall parallel to
the (111) plane.



elastic coupling which now allows the N-domain walls to be explained in terms of an AF-F 180° wall. Also, it would appear that the F wall would result in a magnetoelastic interaction between the domains unless they had forms similar to the C- and CN-domains. Thus, the advantage of a much lower wall energy would be nullified by this interaction.

For the moment a 180° AF-F domain wall parallel to the basal plane only will be considered. Then assuming that the moment in the domain wall sees the strain of the domains equations (13) and (14) can be reduced to give

$$\begin{aligned}
 F &= E_e + E_{me} = 2 \left[(B_{11} - B_{12})N + B_{14}L \right] \cos^2 \phi \\
 &\quad + \text{constant} \\
 &= -K \cos^2 \phi + \text{constant}, \quad K > 0 \\
 &= K \sin^2 \phi + \text{constant}
 \end{aligned}$$

where ϕ is the angle of the moment in the domain wall relative to that of one of the domain phases. K is the effective anisotropy constant because of magnetoelastic coupling and can be applied to the domain wall energy formula given by equations (26) and (27). Then from the data of Voigt³¹ and Levitin et al³⁰, K has a value of $514 \text{ ergs/cm}^3 \pm 20\%$. The exchange constant $A = \frac{1}{2} \lambda M^2 a^2$ has a value of $\sim 2 \times 10^{-6} \text{ ergs/cm}$ for domain walls parallel to

the basal plane. Therefore, a 180° domain wall parallel to the basal plane has an energy of $\sim 1.3 \times 10^{-1}$ ergs/cm² $\pm 20\%$. This is considerably higher than the energy calculated from the data of Table III. However, from Fig. 16 the saturation domain width because of the applied stress gives a wall energy of 10^{-1} ergs/cm². These two values are in reasonable agreement.

A possible explanation for the difference of domain wall energy with and without applied stress is the significance of the shear component B_{14} . In an ideally plane 180° wall parallel to the basal plane the shear component does not contribute any magnetoelastic energy to the domain wall. The shear component can follow the rotation of the moment in the wall without any strain energy since the distortions at different points in the wall will not interact. Therefore, under no external stress the effective anisotropy constant K_1 is just

$$K_1 = 2(B_{11} - B_{12})N = 54.5 \text{ ergs/cm}^3.$$

This results in a domain wall energy of 4×10^{-2} ergs/cm². This value is now in reasonable agreement with those obtained from the data of Table III. Under the applied stress it is necessary for the crystal to have exactly the same strain state and therefore, the shear component

will now contribute.

Walls not parallel to the basal plane will be of significantly higher energy since the sublattice moments are effectively constrained to the basal plane. This then requires that either $\text{div } \underline{m} \neq 0$ or the canting would have to disappear in the wall. The situation could possibly be a combination of these two factors but in any event will lead to a wall approximately an order of magnitude larger in energy. Therefore, unless local strains in the crystal necessitate it the walls will always be as close as possible to parallelism with the basal plane. This is then in agreement with observations.

b) The C- and CN-Domain Walls.

These two walls appear to be the same, however, for the C-domain structure magnetostatic considerations do not appear to play any role. These walls are parallel to planes given by $\frac{\alpha_y}{\alpha_z} = -\frac{L}{N}$. This plane makes approximately -26° angle with the basal plane. These walls then will have $\text{div } \underline{m} \neq 0$. A small change in canting angle in the wall could allow $\text{div } \underline{m} = 0$ in the wall. This unfortunately would require too large an increase in the wall energy. However, since the wall

only makes an angle of 26° with the basal plane, for walls where $\phi \sim 30^\circ - 45^\circ$ the magnetostatic energy of the wall will be negligible compared to the wall energy according to Kaczers results for 60° walls shown in Table I. The demagnetizing field of the wall is treated as an effective uniaxial anisotropy constant. Therefore, the magnetostatic energy of these walls will be ignored compared to the magnetoelastic anisotropy energy. For a wall of angle 2ϕ equation (26) gives the wall energy as

$$\begin{aligned} f_w(2\phi) &= 4\sqrt{AK} (1 - \cos\phi) \\ &= 0.13 (1 - \cos\phi) \end{aligned}$$

In this case the correct value of the anisotropy constant K is that including the shear component since the wall is not parallel to the basal plane.

The CN-domain spacing for the 300μ thick specimen gives, according to equation (32), a wall energy of

$$f_w(2\phi) = 0.1 \sin^2\phi.$$

Since these values for f_w are only approximate, to get a value for ϕ from the two values is not worthwhile.

However, since $\sin^2\phi$ and $1 - \cos\phi$ have almost the same magnitude for all ϕ , then these values have reasonably good agreement.

If the C-domain structure were stabilized magneto-

statically then their equilibrium spacing would indicate wall energies $\sim 10^{-2}$ to 10^{-4} ergs/cm² which are significantly lower than any theoretical estimate of wall energies. This is another indication that these walls must be stabilized by a mechanism such as magnetoelastic coupling to the growth structure. CN-domains are not observed in bulk specimens. This is probably because the demagnetizing effect of the domain walls becomes non-negligible. Also, possibly the strain effects are too complex in bulk crystals and only in a thin section can a relatively strain free crystal be obtained.

There is also the possibility of a domain wall parallel to y-z planes. There is only one circumstance where this was observed and is illustrated in Fig. 13(c). These walls would involve a much larger magnetostatic energy than CN-domain walls. Also, in this case, they indicate a changing ϕ along their length making energy calculations difficult. They are clearly stabilized on crystal defects and therefore, any energy calculations would probably be misleading. In general then these walls would not be expected to occur as a result of magnetostatic effects.

B. The Morin Transition.

The results clearly indicate the phase change occurs via the growth structure of the crystal. The boundary between the AF and WF phases always appears to be (110) growth planes. The process always either starts or ends at the last growth layer or the apparent crystal growth nucleating point. The results for Rh and Ti doped crystals clearly show that the wide transition temperature range is a result of non-uniform doping, with a single transition temperature for a specific doping. The non-uniform doping according to electron microprobe analysis, changes with the growth layers. The data of Figs. 25-26 gives a shift

T_m of the transition per mole % impurity as

$$\sim 40^\circ\text{C}/\text{weight \% Rh} = \sim 50^\circ\text{C}/\text{mole \% Rh}_2^{3+}$$

$$\text{and } \sim -270^\circ\text{C}/\text{weight \% Ti} = \sim -80^\circ/\text{mole \% Ti}^{4+}$$

There may be an error in these values of a multiplicative constant because of the method of electron microprobe analysis for dopant density. However, in the case of the 0.5 mole % Rh sample, fluorescence analysis of the same surface gave reasonable agreement with the electron microprobe value. This value was calculated assuming the doping was constant along boundaries parallel to the AF-WF phase boundaries and evaluating an average doping for the surface using the doping values along the scan

paths.

The pure Ga and Al doped specimens showed a transition range of 1° - 2° C except in the case of the heavily Ga doped specimen illustrated in Fig. 18. This is in agreement with other measurements²⁰ and is probably also a result of non-uniform doping in the last few growth layers. The electron microprobe Ga analysis did not show any non-uniformity. However, this was a specimen of low doping which had a narrow transition.

The pure crystals still had a transition over a finite temperature range which followed the growth structure also. This could possibly be due to changing internal stress during growth. However, a more likely reason is again impurities. If this is the case, impurity levels of ~ 0.01 - 0.02 mole % of Ti and Rh or similar elements such as Sn would be all that is necessary to produce this result. The purity of the chemicals was reagent grade so that this amount of impurity is a distinct possibility. Analysis for such concentrations was beyond the scope of the present work.

A possible model for the way in which the dopants with a $3+$ valence state effect the Morin transition can be based on the lattice distortion effect of the dopants

producing an effective pressure. The Morin transition has been shown to have a pressure dependence^{72, 73, 75} of about $+2.6^{\circ}\text{C}/\text{kbar}$ initially and decreasing to $+1.3^{\circ}\text{C}/\text{kbar}$ at pressures greater than ~ 6 kbar. Also, the dependence of T_M on microcrystal size^{76, 77} has been analysed in terms of a lattice expansion and related to an effective pressure model. That this model is qualitatively correct, in the present case, can be seen by comparing ΔT_M with the difference between ionic radii of the dopants and iron. Dopants with larger ionic radii than iron force the oxygen ions to reduce the space available to the iron ions. This is then equivalent to contractions of the lattice by an external positive pressure which should increase T_M in agreement with the observations. Conversely smaller ionic radii dopants allow more room for the iron ions resulting in an effective negative pressure which lowers T_M . A quantitative analysis is difficult because of an added complication of a real lattice distortion. Also, it is difficult to determine exactly how the impurities distort the lattice.

The effect of Rh ions on the transition temperature was considerably greater than that observed by others^{78, 79} on Rh doped polycrystalline hematite. However, poly-

crystalline materials result in particle size effects as well as possibly non-stoichiometry problems.

The effect of the transition on the domain structure never appeared in most cases to be more than that of a changing WF phase boundary. The only exception to this was the appearance in an occasional thin section of C-domains at the phase boundary probably because of a magnetoelastic effect requiring the magnetostriction in the WF phase to go to zero at the boundary. Obviously, local strains interact with the domain structure and should therefore, produce some effect when the WF-AF boundary crosses them. These effects, appeared however, to be small indicating that either they were almost completely annealed out or that they had a special form such as shear stresses related to the growth structure. The results of Blackman et al⁷⁻¹¹ indicate a crystal with a number of large stress centres. Also, the transition temperature indicates the presence of impurities.

The diffuse colloid boundaries formed at the boundary of the AF-WF phases was produced by the fringing field gradient. The phase boundaries that showed several diffuse lines were probably caused by growth layers under the surface going through the transition at a different

transition temperature from the surface above. These growth layers would magnetoelastically effect the surface layer producing a domain boundary-like effect on the surface still in the WF state.

No temperature hysteresis effect was detected in the transition to within the accuracy of the experiments of about 1°C .

C. Bulk Magnetization Measurements.

1. Magnetometer Measurements.

The hysteresis loop indicate that in unannealed crystals there was a large number of domain wall pinning effects as indicated by the wasp-waistedness of the hysteresis loop. However, after annealing, this disappeared and the loops became much broader indicating a greater contribution from purely magnetostatic effects. The percentage of saturation at loop closure also increased significantly but was still much less than the saturation moment of $\sim 0.4\text{emu/gm}$. This indicates that there are still local stress effects producing a variation of the preferred magnetization direction in the crystal. This is still consistent with a slab-like 180° domain structure because for 180° domains it is possible for the

magnetization to vary without affecting the domain walls. However, for cylindrical domains variation of magnetization direction would produce walls of $\text{div } \underline{m} \neq 0$. Therefore, cylindrical domains may have to change direction of their axis and in a bulk crystal the apparent cylindrical domains structure could actually be a little more complex than indicated by the domain patterns.

For smaller bulk specimens the loops appeared wider and closure occurred at lower fields and higher magnetizations indicating that thin sections could possibly be of very high perfection with little strain effects. However, measurement of these effects is impossible by magnetometer techniques. It would be possible to do it by Mössbauer techniques but the low accuracy of the results and the time consuming aspect make it unrealistic.

The measurements of the magnetization of Rh doped samples at the Morin transition indicate a temperature range for T_M within those of the domain measurements. This is as should be expected since the magnetometer samples were cylinders cut out of a single crystal. The Morin transition temperature showed a shift because of an applied field of $\sim 0.5^\circ\text{C}/\text{kOe}$ which is in agreement with temperature shifts measured by others⁶⁹.

2. Mössbauer Measurements.

Mössbauer measurements indicate that even in large thin sections (2 cms x 1.5 cm) variations in magnetization direction occur. Thus, strain effects are still important. However, domain observations indicate that in some specimens a high degree of perfection with very little strain can occur.

The experiment to detect whether the spin axis was canted out of the basal plane gave indication that this was the case in agreement with Searle⁷⁰. The value of $\sim 10^\circ$ tilt appears significantly larger than that attributable to errors such as geometry. There might be a fundamental error in the technique. It still appears, however, that a more careful experiment performed over a longer time is worthwhile. The original purpose of the experiment was to show that the canting vector \underline{D} could change sign in hematite. This was possible if there is a tilt of the spin axis out of the basal plane since the two states corresponding to $\pm \underline{D}$ would have opposite tilts⁷¹. Therefore, if only one state existed then the experiment should show an asymmetry in the 2,5 peaks for the $+15^\circ$ compared to the -15° orientation. The experiment showed no asymmetry. This could be explained also by a splitting

up to the spins into four sub-lattices⁷⁰ as well as the existence of the ± 2 states. Therefore, a definite conclusion other than the apparent existence of a tilt is impossible.

D. Crystal Physical Characteristics.

The crystals grow with (110) plane from some nucleating point. Subsequent growth appears to start from the corners of two (110) surfaces in layers of $\sim 50 \mu$. The impurities or dopants have the maximum density at the nucleating point. This would suggest in some cases that the dopants, like Rh and Ti are preferentially absorbed into the lattice and increase the likelihood of nucleation of new growth layers. It is also interesting to note that the non-uniform doping occurs for ions of larger ionic radii than iron ions. Thus, it appears that the larger ions are energetically preferred in the growth of hematite. The ions of smaller ionic radii show no large variation of doping other than that occurring in small regions which showed an anomolous increase in dopant density. These probably occur at inclusions or crystal defects. There is also the possibility of formation of different phases such as GaFeO_3 and also possibly incomplete solution of the dopant.

However, apart from these sudden non-uniformities, the otherwise uniform doping level would indicate that this doping occurs by the trapping of the dopant ions as the crystal grows.

In crucibles containing high Rh doping there was a great deal of nucleation producing many small highly terraced crystals. The terracing effect is a dominant feature of more highly doped crystals and is probably caused by too rapid a nucleation of new growth layers. Also, in the more heavily doped crystals there appear lots of voids between growth layers. This indicates that a new growth nucleated and grew faster than one underneath resulting in the void.

The crystals show no twinning after crystal growth. Subsequently annealing did produce what appears to be (110) twins along the growth layers as illustrated in Fig. 28(a). This would indicate that there exists shear strains between growth layers which is relieved on annealing by the creation of these lines of (110) twins.

VI. Conclusion.

A. The Domain Structure.

It appears that spontaneous magnetostriction and its coupling to local strains due to crystal defects play a dominant role in the domain properties of hematite. Ideally, the preferred domain structure is a stripe or slab structure with 180° domain walls. In bulk crystals the magnetoelastic effects in well annealed good quality crystals appear to allow the 180° domains to remain and only cause variations of the direction of the magnetization still retaining 180° walls. In thin sections on the other hand magnetostatic effects are not sufficient to always stabilize a 180° domain structure resulting in the appearance of CN-domains with 2ϕ domain walls where ϕ varies and in many cases goes to zero. The interesting feature of non- 180° walls is their orientation of $\sim 26^\circ$ to the basal plane. Magnetoelastic coupling to the growth structure in bulk (110) surfaces appears to result in variation of magnetization direction resulting in the appearance of walls in the same planes as CN-domain walls.

B. The Morin Transition.

The Morin transition occurs by the crystal forming

an AF and WF phase separated by a boundary which follows the growth structure of the crystal and, with changing temperature, the boundary moves from one growth layer to the next. This effect is clearly related to shift of T_M caused by impurity ions which varies with growth layer as the crystal grows.

C. The Physical Characteristics of Hematite Crystals.

Hematite grows from the flux with a (110) habit of successive (110) platelets. This growth structure and the manner in which impurity ions are taken into the lattice has significant consequences for the Morin transition and the domain structure.

D. Suggestions for Further Experiments.

It would be interesting to compare the domain and Morin transition properties of synthetic hematite with crystals of a different growth habit, such as (111), with the present results. This would then give a direct confirmation of many of the present explanations put forward.

Further analysis of the effect of dopant density on T_M could be carried out to produce a good model for this effect. X-ray diffraction analysis with Co

characteristic x-rays would allow the lattice distortion to be more adequately analysed. By also looking at a few other suitable dopants, a satisfactory model might be obtained.

Further Mössbauer experiments, with more carefully thought out geometry, might allow a conclusive determination of the orientation of the spin axis. This might then allow the controversy over ± 2 to be settled.

Finally, further domain experiments on similar weakly canted single crystals would be interesting in order to show up any properties which are of importance to domain formation in systems with only very weak moments.

References

1. F.J. Morin, Phys. Rev. 78, 819 (1950).
2. C.G. Shull, W.A. Strauser, and E.O. Wollan,
Phys. Rev. 83, 333 (1951).
3. I.E. Dzialoshinskii, Zh. Eksp. Teor. Fiz. 33,
1454 (1957) Sov. Phys. JETP 6, 1120 (1958) .
4. T. Moriya, Phys. Rev. 120, 91 (1960).
5. M. Blackman, G. Haigh, and N.D. Lisgarten, Nature
(London) 179, 1288 (1957).
6. H.J. Williams, R.C. Sherwood, and J.P. Remeika,
J. Appl. Phys. 29, 1772 (1958).
7. M. Blackman and B. Gustard, Nature (London) 193,
360 (1962).
8. M. Blackman and G. Gustard, in 'Proceedings of the
International Conference on Magnetism, Nottingham,
1964' (Institute of Physics and the Physical
Society, London, 1964), p. 600.
9. B. Gustard, Proc. Roy. Soc. (London) A297, 269 (1967).
10. T.E. Gallon, Proc. Roy. Soc. (London) A303, 511 (1968).
11. T.E. Gallon, Proc. Roy. Soc. (London) A303, 525 (1968).
12. N.A. Curry, G.B. Johnston, P.J. Besser, and A.H. Morrish,
Phil. Mag. 12, 221 (1965).
13. P.J. Besser, Ph.D. Thesis, University of Minnesota
(1965).

14. A.H. Morrish, 'The Physical Principles of Magnetism',
(John Wiley & Sons, Inc., New York, 1965).
15. L. Pauling and S.B. Hendricks, J. Amer. Chem. Soc.
47, 781 (1925).
16. R.L. Blake, R.E. Hessevick, T. Zoltai, and L.W. Finger,
Amer. Min. 51, 123 (1966).
17. P.W. Anderson, Phys. Rev. 115, 2 (1959).
18. M.A. Gilleo, Phys. Rev. 109, 777 (1958).
19. C.W. Searle and S.T. Wang, J. Appl. Phys. 39, 1025
(1968).
20. P.J. Besser, A.H. Morrish, and C.W. Searle, Phys.
Rev. 153, 632 (1967).
21. C. Guillaud, J. Phys. Radium 12, 489 (1951).
22. G.W. Dean, Master's Thesis, University of Manitoba
(1970).
23. P.J. Flanders and J.P. Remeika, Phil. Mag. 11, 1271
(1965); P.J. Flanders and W.J. Schuele, in
'Proceedings of the International Conference on
Magnetism, Nottingham, 1964' (Institute of Physics
and the Physical Society, London, 1964) p. 594;
I. Sunagawa and P.J. Flanders, Phil. Mag. 11,
747 (1965).
24. F. van der Woude, Phys. Stat. Sol. 17, 417 (1966).
25. J.O. Artman, J.C. Murphy, and S. Foner, Phys. Rev.
138A, 912 (1965).

26. M. Tachiki and T. Nagamiya, J. Phys. Soc. Japan 13, 452 (1958).
27. S. Iida and A. Tasaki, in 'Proceedings of the International Conference on Magnetism, Nottingham, 1964' (Institute of Physics and the Physical Society, London, 1964) p. 583; K. Mizushima and S. Iida, J. Phys. Soc. Japan 21, 1521 (1966).
28. J.C. Anderson, R.R. Birss, and R.A.M. Scott, in 'Proceedings of the International Conference on Magnetism, Nottingham, 1964' (Institute of Physics and the Physical Society, London, 1964) p. 597.
29. V.P. Andratskii and A.S. Borovik-Romanov, Zh. Eksp. Teor. Fiz. 51, 1030 (1966) Sov. Phys. JETP 24, 687 (1967) .
30. R.Z. Levitin, A.S. Pachomov, and V.A. Shchurov, Phys. Lett. 27A, 603 (1968).
31. W. Voigt, Ann. Phys., Lpz., 22, 129 (1907).
32. H.M.A. Urquhart and J.E. Goldman, Phys. Rev. 101, 1443 (1956).
33. W.F. Brown, 'Magnetostatic Principles in Ferromagnetism' (North-Holland Publ. Co., Amsterdam, 1962).
34. F. Bitter, Phys. Rev. 38, 1903 (1931).
35. F. Bloch, Z. Phys. 74, 295 (1932).
36. L. Neel, C.R. Acad. Sci. (Paris) 241, 533 (1955).

37. C. Kittel, Phys. Rev., 70, 965 (1946); C. Kittel, Rev. Mod. Phys. 21, 541 (1949).
38. J. Kaczer and R. Gemperle, Czech. J. Phys. B11, 510 (1961).
39. Manufactured by 'Micromech Mfg. Corp., 695 Rahway Ave., Union, N.J., U.S.A.'
40. N.F.M. Henry, H. Lipson and W.A. Wooster, 'The Interpretation of X-ray Diffraction Photographs' (MacMillan & Co. Ltd., London, 1961).
41. Manufactured by 'Buehler Ltd., 2120 Greenwood Street., Evanston, Illinois, U.S.A.'
42. D.J. Craik and R.S. Tebble, 'Selected Topics in Solid State Physics, Vol. IV: Ferromagnetism and Ferromagnetic Domains', (John Wiley & Sons, Inc., New York).
43. J. Kaczer, Czech. J. Phys. B12, 354 (1962).
44. M.M. Farztdinov, Izv. Akad. Nauk SSSR (Ser. Fiz.) 28, 590 (1964).
45. J. Kaczer, J. Phys. Rad. 20, 120 (1959).
46. J. Kaczer, Czech. J. Phys. 7, 557 (1957).
47. J.F. Dillon Jr., 'Magnetism III' Edited by G.T. Rado and H.Suhl, (Academic Press Inc., 1963) p. 415.
48. R.C. Sherwood, J.P. Remeika, and H.J. Williams, J. Appl. Phys. 30, 217 (1959).

49. 'The AB Metal Digest' Vol. 12: (Buehler Ltd., 2120 Greenwood St., Evanston, Illinois, U.S.A.).
50. S. Chikazumi 'Physics of Magnetism' (John Wiley & Sons, Inc., New York, 1964).
51. Manufactured by 'Ernst Leitz GMBH, Wetzlar, Germany'.
52. Manufactured by 'Frigistors Ltd., 5770 Andover Ave., Montreal 9, Canada'.
53. C.S. Barrett, Trans. AIMME 161, 15 (1945).
54. A.P.L. Turner, T. Vreeland, and D.P. Pope, Acta. Cryst. A24, 452 (1968).
55. Manufactured by 'N.V. Philip's, Eindhoven,' Holland.
56. W. Parrish, 'Advances in X-ray Diffractometry and X-ray Spectrography (Centrex Publ. Co., 1962).
57. V.E. Cosslett and W.C. Nixon, 'X-ray Microscopy' (Cambridge University Press 1960).
58. Manufactured by 'Princeton Applied Research Corp., Princeton, N.J., U.S.A.'.
59. Manufactured by 'Magnion Inc., 144 Middlesex Turnpike, Burlington, Massachusetts, U.S.A.'.
60. Manufactured by 'Elron Industries Ltd., P.O. Box 5390, Haifa, Israel.
61. Manufactured by 'Nuclear-Chicago Corp., 4501 West North Ave., Melrose Park, Illinois, U.S.A.'.
62. G.K. Wertheim 'The Mossbauer Effect' (Academic Press Inc., New York, 1964).

63. R.Z. Levitin, A.S. Pachomov, and V.A. Shchurov, Zh. Eksp. Teor. Fiz. 56, 1242 (1969) Sov. Phys. JETP 29, 669 (1969) .
64. R. Nathans, S.J. Pickart, H.A. Alperin, and P.J. Brown, Phys. Rev. 136A, 1641 (1964).
65. J.A. Eaton, A.H. Morrish, and C.W. Searle, Phys. Lett. 26A, 520 (1968).
66. K. Siratori and A. Tasaki, Phys. Lett. 27A, 667 (1968).
67. C.W. Searle, Phys. Rev. Lett. 21, 741 (1968).
68. G. Gorodetsky, L.M. Levinson, and Y. Tenenbaum, Phys. Rev. 180, 627 (1969).
69. G. Cinader, P.J. Flanders and S. Shtrikman, Phys. Rev. 162, 419 (1967).
70. C.W. Searle and G.W. Dean, (to be published in Phys. Rev.).
71. V.I. Ozhogin, S.S. Yakimov, R.A. Voskanyan, and V. Ya. Gamlickii, Report Institute of Atomic Energy, Moscow (IAE1674) (1968).
72. H. Umbeyashi, B.C. Frager and G. Shirane, Phys. Rev. Lett., 22, 407 (1966).
73. T.G. Worlton, R.B. Bennion, and R.M. Brugger, Phys. Lett. 24A, 653 (1967).
74. J.A. Eaton and A.H. Morrish, J. Appl. Phys., 40, 3180 (1969).

75. C.W. Searle, Phys. Lett., 25A, 265 (1967).
76. D. Schroerer and R.C. Nininger Jr., Phys. Rev. Lett.,
19, 632 (1967).
77. N. Yamamoto, J. Phys. Soc. Japan, 24, 23 (1968).
78. I. Dezsi, Gy. Erlaki, and L. Keszthelyi, Phys. Stat.
Sol., 21, K121 (1967).
79. E. Kren, P. Szabo, and G. Konczos, Phys. Lett., 19,
103 (1965).
80. D. Quataert and R. Thiesen, in 'First International
Conference on Electron and Ion Beam Science and
Technology', (John Wiley & Sons Inc., New York,
1965) p. 799.